University of Stuttgart
Institute of Nuclear Technology
and Energy Systems

Debris Bed Formation in Degraded Cores of Light Water Reactors

Wael Hilali

February 2019 IKE 2-160

University of Stuttgart
Institute of Nuclear Technology
and Energy Systems

Debris Bed Formation in Degraded Cores of Light Water Reactors

von der Fakultät Energie-, Verfahrens- und Biotechnik der Universität Stuttgart zur Erlangung der Würde eines Doktor-Ingenieurs (Dr.-Ing.) genehmigte Abhandlung

Vorgelegt von

Wael Hilali

geboren in Redeyef, Tunesien

Hauptberichter: Prof. Dr.-Ing. Jörg Starflinger

Mitberichter: Prof. Dr.-Ing. Thomas Schulenberg

Tag der mündlichen Prüfung: 08. Februar 2019

ISSN-0173-6892

February 2019 IKE 2-160

Contents

List of Figures

List of Tables

Nomenclature

Latin Symbols

B	$[-]$	Blake number
d_p	$[\mathrm{m}]$	Mean particle diameter
Eu	$[-]$	Euler number
f	$[-]$	General solution variable
F_{sg},F_{sl}	$[\mathrm{N}]$	Solid-fluid frictional forces
g	$[\mathrm{m} \cdot \mathrm{s}^{-2}]$	Gravitational force
h	$[\mathrm{m}]$	Bed height (spacing in Section 3.6)
He	$[\mathrm{J} \cdot \mathrm{kg}^{-1}]$	Latent heat of evaporation
l_i	$[-]$	Left eigenvectors
$\mathcal{O}$	$[-]$	Order of convergence
q	$[-]$	State vector of the conserved variables
r	$[-]$	Refinement ratio
r^i	$[-]$	Right eigenvectors
S	$[-]$	Source terms vector
s_g	$[-]$	Volume fraction of gas
s_l	$[-]$	Volume fraction of liquid
t	$[\mathrm{s}]$	Time
u	$[\mathrm{m} \cdot \mathrm{s}^{-1}]$	Local mean velocity
u_g, u_l	$[\mathrm{m} \cdot \mathrm{s}^{-1}]$	Gas and liquid superficial velocities
$v_{y_{y=\delta}}$	$[\mathrm{m} \cdot \mathrm{s}^{-1}]$	Velocity of the deposed particles
$v_{y_{y=0}}$	$[\mathrm{m} \cdot \mathrm{s}^{-1}]$	Erosion / absorption rate
W	$[\mathrm{m}]$	Half of vessel width
x, y	$[\mathrm{m}]$	Cartesian coordinates

Greek Symbols

$\beta(x,t)$	$[\mathrm{rad}]$	Local slope angle
β_m	$[\mathrm{rad}]$	Angle of movement
β_s	$[\mathrm{rad}]$	Angle of settlement

γ	$[\mathrm{s}^{-1}]$	Shear rate
δ	$[\mathrm{m}]$	Layer thickness
ε	$[-]$	Porosity
ε_h	$[\mathrm{m}]$	Discretization error
η	$[\mathrm{m}]$	Passability
κ	$[\mathrm{m}^2]$	Permeability
λ_i	$[-]$	Eigenvalues
ρ_{air}	$[\mathrm{kg} \cdot \mathrm{m}^{-3}]$	Air density
ρ_p	$[\mathrm{kg} \cdot \mathrm{m}^{-3}]$	Particle density
ρ_s	$[\mathrm{kg} \cdot \mathrm{m}^{-3}]$	Steam density
σ_N,τ_{xx}	$[\mathrm{N} \cdot \mathrm{m}^{-2}]$	Normal stress
τ_{ij}	$[\mathrm{N} \cdot \mathrm{m}^{-2}]$	Stress tensor
τ,τ_{xy}	$[\mathrm{N} \cdot \mathrm{m}^{-2}]$	Shear stress
ϕ	$[\mathrm{rad}]$	Internal angle of repose
Γ_{evap}	$[\mathrm{m} \cdot \mathrm{s}^{-1}]$	Mass transfer rate
Δt	$[\mathrm{s}]$	Time step
Δx	$[\mathrm{m}]$	Mesh size
$\Delta\omega$	$[\mathrm{m}]$	Melt jet diameter (opening)
Ω	$[-]$	Set of admissible states

Super- & Subscripts

$\tilde{}$	Averaged values
i	State in the cell (i)
f	Formal
L	Belonging to the left cell
n	State at time step (n)
p	Particle
R	Belonging to the right cell

Acronyms

AIAA	American Institute of Aeronautics and Astronautics
APRI	Accident Phenomena of Risk Importance
ASME	American Society of Mechanical Engineers
BeForE	Bed Formation Experiment
BWR	Boiling Water Reactor
CCD	Charge-Coupled Device
CG	Coarse Gravel

DACS	Data Acquisition and Control System
DEFOR	Debris Bed Formation
DG	Diesel Generator
DHF	Dryout Heat Flux
EPR	European Pressurized Water Reactor / Evolutionary Power Reactor
FCI	Fuel Coolant Interactions
FG	Fine Gravel
GCI	Grid Convergence Index
GE	General Electric
GCI	Grid Convergence Index
GHG	Greenhouse Gases
GRS	Gesellschaft für Anlagen- und Reaktorsicherheit
IKE	Institut für Kernenergetik- und Energiesysteme
INES	International Nuclear Event Scale
IRSN	Institut de Radioprotection et de Sûreté Nucléaire
KTH	Kónigliche Technische Hochschule, Stockholm
LOCA	Loss of Coolant Accident
LWR	Light Water Reactor
NPP	Nuclear Power Plant
NOC	Non-Oscillatory Central difference scheme
PDS	Particulate Debris Spreading
PWR	Pressurized Water Reactor
RE	Reference Experiment (in Chapter 3: Richardson Extrapolation)
RPV	Reactor Pressure Vessel
SA	Severe Accident
SBO	Station Black-Out
SLE	Self-Leveling Experiment
TEPCO	Tokyo Electric Power Company
TMI-2	Three Mile Island Unit 2
TPI	Two-Phase Influence
TVD	Total Variation Diminishing
V&V	Verification and Validation
WENO	Weighted Essentially Non-Oscillatory

Abstract

In the aftermath of the Fukushima Dai-Ichi nuclear accident, the issue of corium coolability has received considerable attention in the severe accident research. One of the accident mitigation strategies for the ex-vessel debris cooling is the employment of deep pool water in the cavity below the Reactor Pressure Vessel (RPV). During a hypothetical Severe Accident (SA) in Light Water Reactors (LWR), degraded core materials released from the RPV after its failure will be fragmented and quenched by contact with water. The solidified particles will settle on the bottom forming a porous bed. However, this strategy succeeds only if the residual decay heat is sufficiently removed and the bed is thermally stabilized and will not re-melt again damaging the containment integrity. One of the main factors determining the ability of decay heat removal and long-term coolability of debris bed is its geometrical configuration. A flatter and broader bed can be easier cooled than a higher bed with the same mass of debris. For this purpose, the present work focuses on the development of a two-dimensional continuum model describing the formation process of the debris bed resulting from the deposition of the settling particles and their relocation along the surface of the heap.

The mathematical model is based on a hyperbolic system of partial differential equations determining the overall bed height, the distribution of the flowing particles layer depth and the depth-averaged velocity component tangential to the sliding layer. Because of the hyperbolicity of the system, a successful implementation of a solver is challenging, notably when large gradients of the physical variables appear, e.g., for a moving front in the flowing layer or possibly formed shock waves during the deposition. In this thesis, several numerical methods are applied to solve the system and compared. The implemented Roe-solver has provided promising results, which are verified with analytical solutions in the steady state. The spatial convergence is also reported and quantified with the use of the Grid Convergence Index (GCI). A sensitivity analysis is subsequently performed to study the influence of the uncertainties in the input parameters on the bed geometry.

A dedicated test facility, named BeForE, is designed and built in the framework of this study, with the aim of providing the necessary experimental data for the model validation. A series of tests were conducted using different shaped and multi-size mixtures of particles. It could be evinced, that in addition to the modeled particles sliding the smaller particles ($< 3\ mm$) are subject to the influence of a suspension and convection flows, which are affecting the final bed shape. The comparison between the numerical and the experimental results has shown a very good agreement, notably for the cases where the two last-mentioned phenomena are less present.

Moreover, the test facility could also be used to gain an insight into the influence of steam production on the particulate bed spreading. The decay-heat-induced coolant boiling and the resulting two-phase flow serve as a source of mechanical disturbance, which might lead ultimately to leveling of the debris bed (a.k.a. self-leveling). A series of experiments were then conducted by discharging solid particles in the two-dimensional viewing vessel of the facility, while air bubbles simulating the steam production are injected simultaneously from the bottom. Depending on the quantity of the settled particles on the top of each section of the vessel, air flow rate is so monitored and adjusted in time to simulate the corresponding amount of steam produced by the similar quantity of hot debris. This study shows that, in most of the cases, the two-phase flow inside the vessel alters the sedimentation process resulting in a broader and flatter bed than under quiescent conditions. However, it was observed that in the case of customarily formed concave beds in the quiescent conditions, the presence of the gas flow can change the mound shape to a convex type with a higher bed height, at least in the beginning. It was also shown that, for high gas flow rates, the convective flows induced by the bubble plumes inside the bed would contribute to the diminishment of self-leveling effect and a slower particles redistribution. Lastly, it was mathematically described how the steam production could reduce the characteristic angles of repose of a debris bed, putting forth a physical explanation of the self-leveling phenomenon. With the coupling of the developed continuum model with a model simulating the two-phase flow within the bed, a full numerical simulation of the avalanche-like particles motion during the self-leveling process could also be successfully provided. This allows a more accurate simulation of the bed formation process under the influence of steam production, which is of particular importance for the bed coolability and a decisive requirement for the nuclear accident progression and termination.

Zusammenfassung

Im Fall eines schweren Unfalls in einem Leichtwasserreaktor kann eine anhaltende Kühlwasserunterversorgung zu einer Überhitzung der Brennelemente und schlussendlich zu einer Zerstörung des Reaktorkerns führen. Unter diesen Bedingungen kann in verschiedenen Stadien des Störfalls eine Schüttung wärmefreisetzender Feststoffpartikel durch Fragmentierung des geschmolzenen Reaktorkerns entstehen. Die langfristige Kühlbarkeit solcher Schüttungen ist von großer Bedeutung, um eine Beschädigung der Barrieren (Reaktordruckbehälter, Sicherheitsbehälter) und damit die Freisetzung der Spaltprodukte an die Umwelt zu vermeiden. Eine der entscheidenden Voraussetzung für die langfristige und stetige Kühlung des gebildeten Betts ist seine geometrische Konfiguration. Eine flachere und breitere Schüttung kann leichter und schneller gekühlt werden als ein höheres Bett mit der gleichen Debrismasse.

Das Ziel der vorliegenden Arbeit ist die zweidimensionale Modellierung der Schüttbettbildung und die Implementierung und Validierung eines numerischen Kontinuumsmodells zur Simulation der Partikelablagerung und Verlagerung entlang der Bettoberfläche. Das Simulationsprogramm kann sowohl als Stand-Alone Modul eingesetzt werden oder auch in den System-code COCOMO integriert werden

Die mathematische Modellierung beruht auf einem hyperbolischen System partieller Differentialgleichungen, aus dem die lokale Schüttbetthöhe, die Schichttiefe der fließenden Partikel, sowie die tangential zur Fließschicht tiefengemittelte Geschwindigkeitskomponente bestimmt werden können. Wegen der Hyperbolizität des Systems stellte die Implementierung eines geeigneten numerischen Lösers eine Herausforderung dar, insbesondere wenn große Gradienten der physikalischen Größen auftreten, z.B. für eine sich bewegende Front in der Fließpartikelschicht. In dieser Arbeit wurden mehrere numerische Methoden angewendet und nach Stabilität und Genauigkeit verglichen. Der implementierte Roe-Solver lieferte die besten numerischen Ergebnisse, die mit analytischen Lösungen im stationären Zustand verifiziert werden konnten. Die räumliche Konvergenz wurde ebenfalls mithilfe des „grid convergence index (GCI)“ bewertet und quantifiziert. Anschließend wurde eine Sensitivitätsanalyse durchgeführt, um den Einfluss der Unsicherheiten der Eingangsparameter auf die gesamte Bettgeometrie zu ermitteln.

Im Rahmen dieser Arbeit wurde ein Versuchsstand mit dem Namen BeForE entworfen und aufgebaut, um experimentelle Daten für die Modellvalidierung bereitzustellen. Eine Reihe von Tests wurde unter Verwendung polydisperser Teilchenmischungen durchgeführt. Es konnte gezeigt werden, dass neben dem modellierten Partikelablagerungs-

regime die kleineren Partikel (mit $d_p < 3\ mm$) dem Einfluss von Suspensions- und Konvektionsströmungen im Wasser unterliegen, die sich auf die endgültige Schüttbettgeometrie auswirken. Der Vergleich zwischen den numerischen und den experimentellen Ergebnissen ergab eine sehr gute Übereinstimmung, insbesondere für die Fälle, in denen die beiden letztgenannten Phänomene weniger präsent sind.
Außerdem konnte die Testanlage auch genutzt werden, um den Einfluss der Dampfproduktion auf die Partikelausbreitung zu untersuchen. Das durch die Nachzerfallswärme induzierte Sieden des Kühlmittels und die daraus resultierende Zweiphasenströmung dienen als eine Quelle für mechanische Störungen im Partikelbett, die letztendlich zu einer Nivellierung der Schüttung führen können (auch als „Self-leveling “ bezeichnet). Eine Reihe von Experimenten wurde durchgeführt, in denen Feststoffpartikel in den transparenten Wasserbehälter von oben abgelassen wurden, und gleichzeitig Luftblasen, die die Dampfproduktion simulierten, von unten eingespritzt wurden. Die Luftströmungsrate in jedem Abschnitt des Behälters wurde als Funktion der Menge der abgesetzten Partikel so eingestellt, dass sie der Menge an Dampf entspricht, der durch die heißen wärmefreisetzender Feststoffteilchen erzeugt wird. Die vorliegenden Untersuchungen lassen erkennen, dass in den meisten Fällen die Zweiphasenströmung innerhalb des Wasserpools den Sedimentationsprozess beeinflusst, was zu einem breiteren und flacheren Bett als der unter ruhenden Bedingungen gebildeten Schüttung führt. Es wurde jedoch beobachtet, dass im Falle von üblicherweise geformten konkaven Betten ohne Wassersieden die Bettform konvex mit einer höheren Höhe aufgrund der Zweiphasenströmung geworden ist. Es wurde weiterhin gezeigt, dass bei hohen Gasflussraten die durch die Blasenfahnen im Wasserpool induzierten konvektiven Strömungen zur Verringerung des Self-leveling-Effekts und einer langsameren Partikelverlagerung beitragen würden. Schließlich wurde ein mathematisches Modell formuliert, das die Reduktion des charakteristischen Schüttbettwinkel aufgrund der Dampferzeugung abbildet und hierdurch eine physikalische Erklärung für das Self-leveling-Phänomen liefert. Die Kopplung des entwickelten Kontinuumsmodells mit einem Modell, das die Zweiphasenströmung innerhalb des Betts simuliert, ermöglicht eine genauere Simulation des Bettbildungsprozesses unter dem Einfluss der Dampferzeugung, was für die langfristige Schüttbettkühlbarkeit von entscheidender Bedeutung ist.

1

Introduction

1.1 Background and Motivation

Nuclear Power Plants (NPP) account for more than 11% of the world's electricity generation as continuous and reliable power to meet the increasing energy demand, without carbon dioxide emissions. As of December 2017, there are 448 commercial nuclear reactors operating in 30 countries, with over 391,000 MWe of total capacity. Among them, 13 countries relied on nuclear energy to supply at least one-quarter of their total electricity demand [53]. Moreover, the nuclear energy has one of the lowest impacts on the environment compared to other electricity generation methods. Coal-fired power plants have approximately 30 times greater GHG (GreenHouse Gases) emissions than nuclear on a lifecycle basis[1]. In 2011, the nuclear power plants supplied 2518 TWh of electricity worldwide, avoiding 2163 million tonnes of additional CO_2 emissions that would have been produced if coal had been used for generating the same amount of electricity [56]. In spite of these benefits, nuclear energy in its current form has limitations, both perceived and real, regarding economics, waste, proliferation, and safety. Since the 1950s, its high energy density gave rise to concerns about accidents in nuclear power plants (NPP) and their possible effects on the humans and the environment. Actually, a nuclear power plant is a thermal power station, in which heat is produced during the nuclear fission reaction. The generated heat is absorbed by the surrounding coolant (e.g., water) to produce vapor, which drives a steam turbine connected to an electrical generator to produce electricity. A vast majority of the used commercial nuclear reactors ($> 80\%$) in the world

---

[1] Lifecycle approach is defined as accounting emissions from all phases of the project (construction, operation, and decommissioning)

are Light Water Reactors (LWRs) using ordinary (light) water as the coolant. In these reactors, several cooling systems are employed to ensure a continuous and sufficient flow of coolant into the core and to remove all the generated decay heat. Despite its very low probability and the very high safety standards, simultaneous failures of all the regular and emergency cooling systems may occur, due to an event, that exceeds the range of plant design, like the tsunami and earthquake in Fukushima. In such severe accident scenarios, when all safety measures fail, the heating-up of the fuel elements due to the residual decay heat can occur, leading subsequently to a melting of the reactor core. As a consequence of the core damage, the release of the radioactive materials contained in the reactor core would create a major public hazard.

In the 60 years of history and over 17,000 cumulative reactor-years of civil operation, there have been three significant Severe Accidents (SA) - Three Mile Island TMI-2 (USA 1979), Chernobyl (Ukraine 1986), and Fukushima (Japan 2011) -. Apart from Chernobyl, the two others are the major core melt accidents in an LWR of western type.

On March 28, 1979, in Harrisburg (USA), the Three Mile Island Unit 2 (TMI-2) pressurized water reactor underwent a LOCA accident due to the coincidence of unfavorable factors and operator misjudgment that led to a partial melt of the reactor core. The post-accident investigations have shown that the core of the reactor was destroyed to a large degree, and about 17-20 tons of the molten corium (UO_2 + ZrO_2 + structure materials) had reached the lower head of the reactor pressure vessel (RPV), threatening its integrity [18]. Fortunately, the progression of the accident was mitigated by the injection of emergency cooling water, and only a tiny amount of radioactivity (999 GBq) was released to the environment [19].

The accident at Fukushima Daiichi nuclear power plant on March 11, 2011, was triggered by natural phenomena, an earthquake of magnitude 9.0 followed by tsunami waves. The Fukushima Dai-ichi (or Fukushima I) site included 6 GE boiling water reactors. When the quake hit, all the reactors of Units 1-3 (R1, R2, and R3) scrammed to fully insert all the control rods. Meanwhile, R4-R6 were not operating at that time but were affected. The main problem initially centered on R1-R3. Unit 4 became a problem on the fifth day. The earthquake partially damaged or utterly failed every equipment to receive external electric power supply for the first four reactors. Thereafter, the tsunami waves destroyed most of the sea-water cooling systems, inundated the electrical switchgear and batteries and flooded all the emergency Diesel Generators (DG) but one. The three units had Station Black-Out (SBO, Loss of all AC power) and lost the ability to maintain proper reactor cooling and water circulation functions. The power supply was lost 1 hour after the shutdown of the fission reactions. The cores would be still producing at that moment about 1.5% of their nominal thermal power resulted from the decay heat ($\sim$ 22 MW in R1 and $\sim$ 33 MW in R2,3). With the loss of their ultimate heat sink, the reactor cores overheated, much steam was produced in the RPV, and the water level dropped. The temperature of the exposed fuel rose to over 2800°C so that the nuclear fuel melted and dropped few hours after the scram into the water at the bottom of the RPV. Hydrogen was produced primarily by the interaction of the fuel's heated zirconium cladding with steam, leading to explosions inside the reactor buildings in R1, R3 and R4. In the following weeks, the TEPCO operators were focusing their efforts on restoring heat removal from the damaged reactors and coping with overheated spent fuel ponds. Official "cold shutdown condition" was announced in mid-December 2011. Due to high radioactive releases (estimated to be 940 PBq [iodine-131 equivalent] in total), the Fukushima accident was ranked Level-7 on the International Nuclear Event Scale (INES), the worst [1].

Therefore, the consideration of nuclear severe accidents is an essential component of the defense in depth approach in nuclear safety and a good understanding of the phenomena occurred in these accidents is crucial for mapping out and implementing effective accident management measures. One of the main questions in the mitigation of the consequences of a hypothetical core melt accident is how to cool and stabilize the formed debris bed, and hence protecting the structural integrity of the containment.

1.2 Debris bed formation in a light water reactor

Debris bed may be formed in different stages of a core melt accident. It generates residual heat due to the radioactive decay of the fission products, which is in the order of 6% of the thermal reactor power instantly after a regular or emergency shutdown, and decreases to about 1% of the operation power after one hour.

During a severe accident with a failure of the normal and emergency water cooling systems, the decay power yields a continued heat-up of the reactor core leading to water evaporation and water level decrease in the RPV. If the water supply is less than the evaporation rate, the fuel rods and the other core materials in the dry region heat up. With increasing temperature ($> 1200°C$), the zirconium of the rod cladding or the guide tubes reacts with the superheated steam (Zr-oxidation). This exothermic reaction accelerates the core degradation in its turn due to additional heat production. By this reaction, a significant amount of hydrogen is produced, which may arrive in the reactor containment and can lead to the deflagration or detonation of the gas mixture with the risk of premature failure of the containment [19] [28].

The re-establishment of water supply in this stage of the accident yields a thermal shock to the hot rods, due to its direct contact with cooling water. As shown in Figure 1.1(a), the rods may then crumble, and form a porous configuration with particulate debris surrounded by intact core regions. Compared to the intact fuel rods, the dense packing and small particle sizes (see post-accident investigations of TMI-2 in [83]) of the porous debris allow only limited permeability for the fluid and impede therefore the efficient cooling. The further progress of the accident in this stage depends on the temperature stabilization and the quenching of the debris bed (i.e., to be cooled down to saturation temperature by flooding with cooling water) before melting.

Without reestablished cooling, the core temperature will further increase, eventuating in the melting of the core materials. The metallic components like the rod cladding and steel from the mounting structures will start first melting. With further heat-up, the ceramic parts of oxidized ZrO_2 and UO_2 fuel will then start melting. Driven by the gravity, the molten materials will relocate to the lower core regions, where the temperature is expected to be lower than the one in the upper parts of the core due to its later dryout during the water level lessening. The relocated molten materials will therefore solidify and form a crust structure there. The stability of such crust conditions depends on the cooling from below, e.g., by heat conduction, steam flow, and also radiation to water. Several scenarios may be considered. In the first case, an insufficient cooling from below will prevent stable crust formation. Consequently, there will be no large melt accumulation and the molten materials will gradually flow to the lower plenum. Otherwise, with proper cooling of the crust, a large amount of melt will be collected in the core region, supported by a crust, as observed in TMI-2 post-accident investigation [98] [140]. Due to natural convection in the pool, a higher temperature will be reached at the top, leading to crust failure in this upper region and to a lateral melt release into the lower head. It is expected that melt outflow rate will be relatively low due to the limited size of the breaches and the limited height of the molten pool. In the view of reactor safety, this small flux is favorable, since it yields a better fragmentation of melt jet when pouring into the residual water in the lower head, and it also reduces the risk of steam explosion.

If the Reactor Pressure Vessel (RPV) is intact, it is expected that its lower head will be filled with residual water. In the case of small melt fluxes, the jet will break up by contact with water and fragment into droplets that solidify and settle down as porous particles bed (see Figure 1.1(b)). This interaction between the melt jet and water was underscored by the experimental results from the FARO-experiments (Fuel melt And Release Oven) [98] as well as by TMI-2 post-accident investigations [77] [78]. It was shown that through interaction with the residual water, melt jets with diameters of few centimeters will at least be partially fragmented into droplets with an average size of few millimeters. The diameter of the deposed solidified particles is expected to be from 1 mm to 10 mm. Depending on the reactor type and the corium composition, the formed particles beds could still include a specific power of 100-300 W/kg. To ensure long-term coolability and the in-vessel retention of the corium, this decay heat must be removed by the water evaporation, which should be refilled by water feeding to the vessel and the resulting successful quenching of the bed (conditions for the long-term coolability and quenching are discussed in detail by Rahman and Schmidt in [95] and [114] respectively). If the resulting debris is not coolable, due to non-availability of efficient cooling measures or because of its non-coolable configuration (e.g., large melt mass, large unfragmented parts, large dryout heat flux (DHF)[2]), the water will boil-off, and the corium will remelt,

---

[2] The enthalpy of the steam outflowing from the particles bed averaged over the cross-sectional surface area is the heat flux. The dryout heat flux DHF $\left[\mathrm{W/m^2}\right]$ corresponds to the maximum (critical) steam flux that can escape through the upper surface, i.e., it corresponds to the mass flux at which the water infiltration is no longer capable of replacing the evaporated steam and dryout is therefore achieved in some part of the bed interior. It is practically determined when the void fraction α in the pores reaches one. If the decay heat flux is below this DHF-limit, it can be deduced that stable coolable condition is reached for the particulate bed.

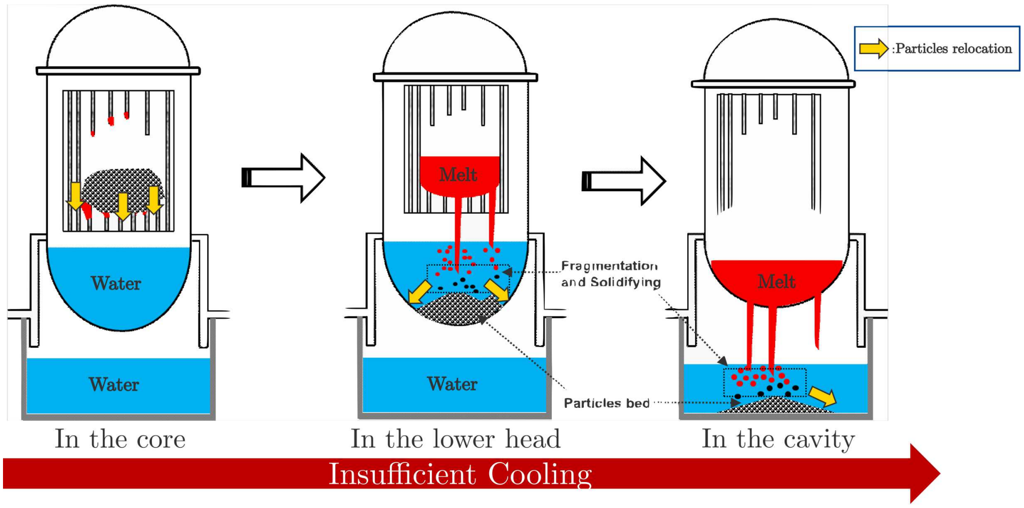

(a) (b) (c)

Figure 1.1: Different stages of meltdown and debris bed formation: (a) melting of reactor core; (b) relocation to the lower plenum of the RPV, (c) failure of the RPV and ex-vessel bed formation

forming a melt pool in the lower head. Without external cooling, the RPV walls will be attacked and weakened due to the thermal loads. It will begin creeping, and the vessel will finally fail, leading to a melt release into the cavity below the RPV.

After vessel failure, the retention of the released melt and the achievement of a safely cooled state of corium are of prime concern for the mitigation of the SA consequences. Otherwise, it will lead to basement erosion in the cavity and endanger the containment integrity. The main ex-vessel corium retention strategies are the use of core-catcher [117] or the flooding of the reactor cavity. The emphasis of the present study is laid on the formation process of debris bed by melt jet-water interaction in the reflooded cavity, and the use of the core catcher concept is beyond the scope of this study (more details about this concept can be found in [12] [39] [118] [for the EPR core catcher], and in [2] [139] [for the COMET concept]).

As a severe accident mitigation strategy adopted in several designs of light water reactors and specifically in boiling water reactors (BWR), a deep pool of water is foreseen in the cavity below the RPV. In fact, it is assumed that the corium pouring out of the broken vessel to a highly-subcooled ($\sim 80-90$ K) deep water pool ($7-11$ m) is expected to fragment, solidify, settle and form a debris bed, which is likely to be coolable by heat transfer to, and evaporation of, water (see Figure 1.1(c)). However, the molten corium jet fragmentation depends strongly on the vessel breach size and the water pool depth. Actually, the melt break-up will be reduced with thicker jets and with less deep pools, which may lead in some cases to bed configurations containing molten parts in the interior. According to findings from FARO experiments, a good fragmentation and solidification of the melt jet without large steam explosions are likely expected to take place. In the present work, a full fragmentation of the corium without steam explosions is therefore assumed to happen after the vessel failure, and a solid particles bed will be formed in the cavity.

The efficiency of heat removal from the formed beds is, however, contingent upon a number of parameters, including bed's height and its overall geometry among others. Therefore, the question of debris bed formation is addressed in the present thesis by experimental and numerical investigations of solid particles deposition and relocation.

1.3 Importance of debris bed formation for severe accident mitigation

The coolability of core debris bed is an important issue in the severe accident mitigation strategy, aiming at stabilizing the bed thermally by coolant ingress and preventing a possible re-melting. On the other hand, the long-term coolability of the particles bed depends on its physical properties and the ambient pressure. The main bed properties influencing the dryout heat flux include porosity, particle size (d_p) and morphology, and the bed geometry. The porosity ε and the characteristics of the particles affect the coolability mainly through the frictional forces between the solid particles and the fluid phases. Specifically, the effect of particle size was studied experimentally since the $1980's$ by Trenberth et al. (1980) [131] and Barelon and Werle (1981) [6], summaries of these investigations were given by Buerger and Schmidt in [20] and [114], respectively. It was found that the inter-phase frictional forces decrease with increasing particle size, leading to the improvement of porous medium capability of removing heat. Larger porosity increases the coolant ingress in the pores and favors the boiling. For smaller particles and consequently smaller pores, more resistance is acting against the coolant and steam flows. Hence, larger particles and higher porosity are favorable for the bed coolability ($d_p \nearrow, \varepsilon \nearrow \Rightarrow DHF \nearrow$). The system pressure also influences the coolability through the material properties of the steam. This effect was investigated in different studies by Miyazaki et al. (1986) [85], Reed et al. (1985) [97], and Squarer et al. (1982) [125]. For example, experimental results from the DCC2-tests (Degraded Core Coolability) [97] are illustrated in Figure 1.2. Several dryout measurements in particulate bed (with an effective particle diameters being $d_p = 1.42$ mm and a measured porosity $\varepsilon = 0.41$) were performed with varying pressure. Starting from the atmospheric pressure, the dryout heat flux (DHF) increases strongly with increasing ambient pressure. With higher pressure, the vapor density increases and the produced steam fills up accordingly less volume fraction. Larger heat removal rates can be then achieved with denser steam, because more pore volume is then available for the coolant. The decrease in the latent heat of vaporization for higher pressure counteracts the effect of the increased steam density. This effect becomes dominant for pressure above 7 MPa, leading to the decrease of the DHF for this high pressure values.

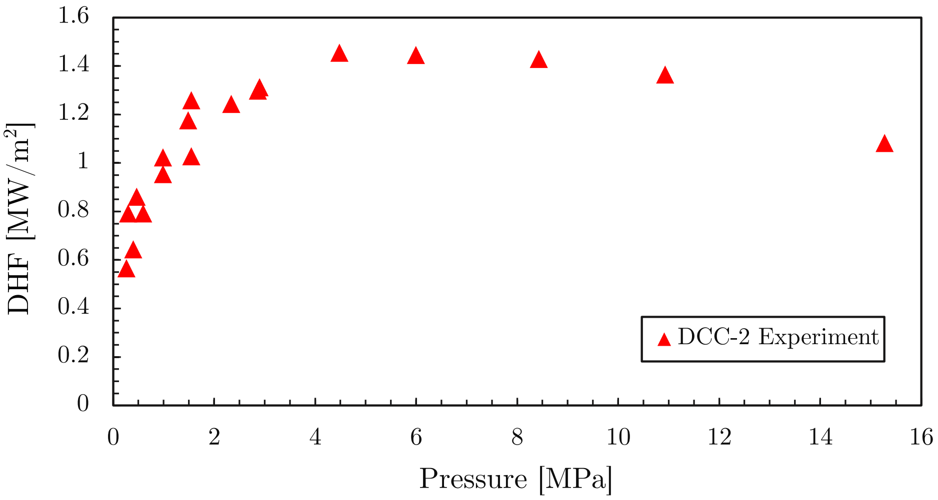

Figure 1.2: Influence of system pressure on dryout heat flux [97] ($d_p = 1.42mm, \varepsilon = 0.4$)

Regarding bed formation and its geometrical configuration, the fragmentation of molten corium when falling-through a water pool has been studied experimentally since the 1990's. The most important melt jet fragmentation tests are the CCM [124], FARO [80] [79] [77], TROI [122], COTELS [145] and KROTOS [50] tests using simulant materials as well as prototypic corium. There are indications from the FARO-experiments [77] that the behavior of the solidified particles during the formation process of debris bed, at least for fully fragmented melt jet, is similar to the behavior of granular material. When such particles are poured onto a horizontal flat surface, they form a conical pile characterized by the slope angle. These experimental observations will be the starting point of the present study for the modeling of the bed formation process (see Chapter 2). In fact, one of the crucial conditions for the long-term coolability of debris bed is its geometrical configuration and the bed height. The shape of the bed, higher or flatter, i.e., more piled or more spread, depends on its characteristic slope angle. In order to get an impression of the importance of bed geometry and its influence on the debris coolability, simulations with COCOMO (see Section 1.4) have been performed with three different conical beds varying the angle of repose, as already initiated by Rahman in [95]. It has been assumed that each time the same corium mass of 190 t has been solidified forming particles beds with a porosity of 40%. The beds have the dimensions shown in Figure 1.3.

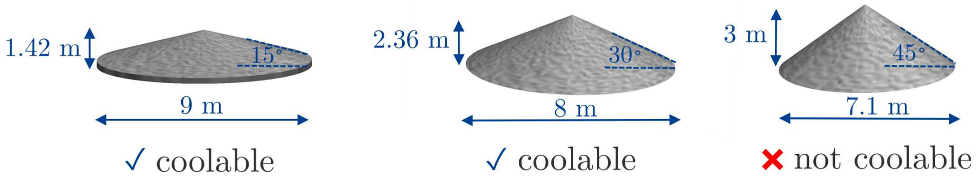

Figure 1.3: Sketch of the different geometrical configurations used for the COCOMO-simulations

Table 1.1: Results of quench-simulations with the system code COCOMO

	Slope angle	complete quenching	Quench time [s]
Ex-vessel debris bed	15°	achieved	6888
	30°	achieved	11801
	45°	not achieved	–

As illustrated in Table 1.1, results of the numerical simulations indicate that complete quenching occurs only for configurations with the angle of repose 15° (such small angle can be caused by the influence of the steam production inside the hot debris bed and the resulting bed spreading [see Chapter 5]) and also for the angle 30°. Comparing the total quenching time, faster quenching is observed in the case of the debris bed with the smaller angle of repose. A flatter and broader bed can be easier cooled than a higher bed with the same mass of the debris.

The above-demonstrated example confirms the necessity of developing a numerical model predicting the geometrical configuration of formed debris bed and taking into account the physical properties of the discharged material as well as the geometrical boundary conditions. The investigations, both computational or experimental, of the bed formation process are still scanty. And the particles deposition and relocation are still not sufficiently studied or accurately modeled in any of the dedicated computer codes for SA simulation and bed coolability. Hitherto, most of the quench and dryout experiments and simulations have been carried out assuming an already formed bed with a steady non-changeable geometrical configuration.

1.4 Computer modeling and state of the art

In order to have sufficient knowledge on the evolution and on the physical processes of core melting and degradation in the late phase of a severe accident, a number of experimental programs as ACRR [41], CORA [113], LOFT [87], and PHEBUS [30] [116] and several small-scale and separate effect experiments (e.g., DEBRIS [69]) have been conducted in the last few years. The findings from these studies have been used for the development of a number of computer modeling codes and simulation tools to recreate the phenomena occurring during the SA and evaluate the chances and the influences of accident management measures. In this context, a distinction should be made between integral codes (such as ASTEC [133], MAAP [13] or MELCOR [42]) that represent the entire power plant, but with a considerable simplification of specific physical phenomena, as well as special SA analysis codes that focus on individual phenomena, as ATHLET-CD [130] and ICARE [24]. Some of these latter are in turn coupled with integral codes.

The German-French code ASTEC [25] [133] (Accident Source Term Evaluation Code) is developed by the IRSN (Institut de Radioprotection et de Sûreté Nucléaire) and the GRS (Gesellschaft für Anlagen- und Reaktorsicherheit) jointly with different other partners. The code couples numerous modules, which can also be used independently. It can thus cover all relevant phenomena in RPV, in the primary and secondary circuits, and in the containment. Of particular interest in this context is the stand-alone code ICARE/CATHARE [24] developed at the IRSN in France, which is integrated within ASTEC, and it can cover all major phenomena from core melting to the RPV failure.

The German system code ATHLET-CD [130] (Analysis of Thermal-hydraulics of Leaks and Transient - Core Degradation) is being developed by GRS in cooperation with the IKE (Institut für Kernenergetik und Energiesysteme). It enables the simulation of regular and beyond-design-basis events in light water reactors. In ATHLET-CD the module MEWA [49] (MElt and WAter) is implemented for the description of in- and ex-vessel behavior of corium during the late phase of a SA. The code JEMI [92] (Jet Fragmentation and Premixing) is designed to simulate the fragmentation of the poured melt into water, mixing, solidifying and the settling of particles forming a debris bed. However, the major drawback in this code is that the particles deposition and the formed bed are still neither well detailed nor dynamically modeled. The bed formation process is only described with simplified geometrical formula and assumptions, without any consideration of the different physical phenomena related to the particles deposition and relocation. It is assumed that the formed bed is homogeneously cone-shaped (i.e., a constant and uniform slope angle along the whole bed surface). The numerical modeling addresses neither the changing bed geometry nor the possible interactions between the solidified particles and the two-phase flows in the water pool and within the porous bed.

Both codes MEWA and JEMI can be used as stand-alone mechanistic simulation tools or coupled together in the system code COCOMO (Corium Coolability Model), which is also being under development at IKE. MEWA is designed to describe the coolability of porous particulate bed, taking into account process of melting, melt relocation, molten pool formation and behavior as well as the two-phase flow of water and steam inside the solid bed. In MEWA, three separate continuum phases, i.e., solid particles, liquid coolant, and the gas, are considered in thermal non-equilibrium. Though, the solid particles in the MEWA-modeling are assumed to be in a fixed matrix. In the last few years, particular attention has been paid to the modification and implementation of interfacial friction and heat transfer models [95] [114] in MEWA and its extension for three-dimensional bed geometries [47].

The debris bed formation has been gaining more importance in the recent few years. Of particular note is the APRI research project (Accident Phenomena of Risk Importance) [67] initiated at the Royal Institute of Technology (KTH). In the framework of this research program, different computational approaches and experimental studies have also been carried out in the DEFOR (DEbris bed FORmation) facility to study the characteristics of debris beds formed upon fuel-coolant interactions (FCI) [32] [58] [64] [65] [66]. A thermohydraulic code, named DECOSIM, has also been developed at the KTH for the simulation of FCI and the investigation of bed coolability [67] [141]. The DECOSIM code is not merely for the simulation of the multi-phase flow inside already formed beds but it can be considered for the simulation of the convection flows in the pool, where turbulence models and discrete particle models apply [142]. However, a continuum model describing the formation process from particles relocation is still lacking. On the other hand, considerable attention within the DEFOR program has also been paid to the influence of coolant boiling on the particles spreading[3]. Experiments on particulate debris spreading (PDS) due to self-leveling have been carried out [7]. Based on these experimental observations (particularly on PDS-C tests - Particulate Debris Spreading Closures -), a scaling approach and semi-empirical closures have been developed for the prediction of the bed leveling and subsequently implemented in the DECOSIM code [8] [9]. Nevertheless, more general physical and deterministic numerical models of the self-leveling phenomenon are still required.

Viewing the importance of the geometrical configuration for the debris bed coolability and the termination of a SA, the focus of this thesis lies on the mathematical and physical description of debris bed formation and the implementation of a numerical model simulating particles sedimentation, deposition and relocation. This model can be used as a stand-alone module and also integrated subsequently in the code COCOMO, allowing a more realistic simulation of the core-melt accident. Based on numerical calculations with JEMI for a specified reactor scenario, the range of the input parameters needed by the developed model can be delineated, and with it the bed geometry can be appropriately determined. The MEWA-code can perform then its numerical simulation on this particular geometry (see Figure 1.4).

---

[3] An extended review of recent studies addressing the bed spreading due to self-leveling can be found in the dedicated Chapter 5

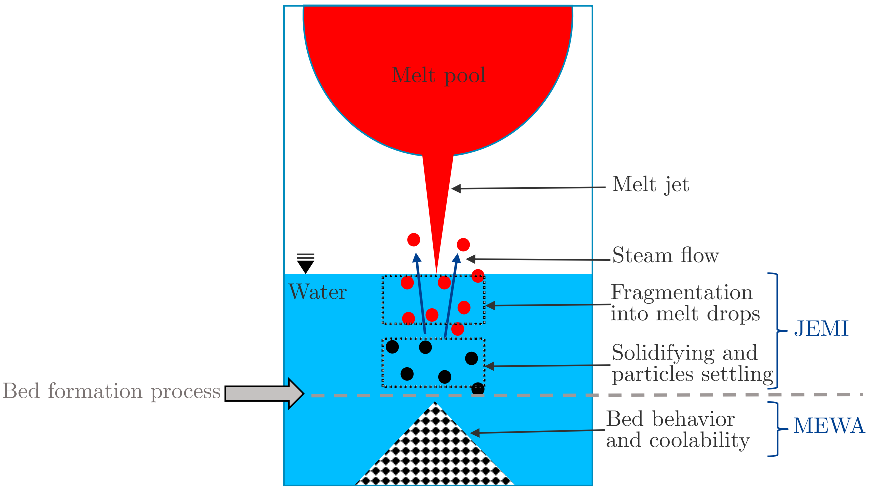

Figure 1.4: Computer modeling in COCOMO of the ex-vessel bed behavior

1.5 Aim of the present work

The paramount aim of the present work is to develop a numerical continuum model simulating the deposition and relocation of solidified particles. In the view of reactor safety, the scientific value of this thesis is the study of bed formation (mainly ex-vessel beds), which may be formed during the late phase of severe accidents with core melting in a light water reactor. The geometrical configuration of such particulate beds is considered to be of particular relevance for the bed coolability and a decisive requirement for the accident progression and termination. The coupling of the presented model with the system code COCOMO will enable a more realistic simulation of the core-melt accident. Despite its importance, very little studies and nearly no significant insights were found in the literature on the process of debris bed formation. The focus of most of the experimental and numerical studies in this stage of the SA lied on the steam explosion, on the molten fuel-coolant interactions (e.g., jet breakup, melt droplet fragmentation, premixing), or on the bed coolability and the two-phase flow inside already formed geometries, but not the formation process itself. The past most of the theoretical and experimental studies on debris coolability have taken the shape of the bed as predefined, and the particles are assumed to be fixed. Scarce experimental studies were investigating the sedimentation of solid particles and its interaction with the coolant [61] and the self-leveling process (the latter works are mainly based on correlations and empirical closures - see Chapter 5 -). But, to the best of our knowledge, no numerical continuum model has been set to investigate the formation process. The present study aims precisely to fill the above-mentioned gap in the modeling of severe accidents with a meltdown.

Due to the similarities between the solidified corium particles and the behavior of dense granular material, the implemented model and the mathematical description are based on the contemporary knowledge and former experimental and numerical studies of gran-

ular matter mechanics, which may be encountered in many other applications including processing and manufacturing industries as well as in geophysical flows (e.g., dense snow avalanches and rockfalls) [15] [38] [60] [90].
With the aim of developing an accurate and credible simulation code, it is a big concern to ensure the "correctness" of the presented model. This concern is addressed through model Verification and Validation (V&V). Therefore, a verification with analytic solutions and the validation with experimental data are envisaged in the present study. For that purpose, the test facility "BeForE" has been newly designed and built within the framework of this study. In the same context of model quality assessment, the uncertainties and the different source of errors should also be investigated and quantified, in order to study its influence on the results accuracy, mainly on the bed height, the main factor influencing the coolability. Additionally, the phenomenon of self-leveling, which can influence the bed geometry and increases the chances of its coolability, will be subsequently elucidated. This phenomenon may occur as a result of the coolant boiling and the two-phase flow inside the bed.

Outline of the work

The remainder of this thesis is structured as follows:
At first, a physical and mathematical description of a two-dimensional (2D) continuum model for the bed formation process will be introduced in Chapter 2. In this chapter, the modeling approach and assumptions will be presented, and the resulting main equations governing the particles dynamics during deposition and relocation will be then derived and explained in details.
In Chapter 3, the numerical methods used for the solution of the system equations and the numerical results will be then presented and explained. In order to verify the computer modeling, a comparison between the numerical simulations and analytical solutions will also be performed. Subsequently, the numerical uncertainties and errors will be reported and quantified, and a sensitivity analysis will be then conducted. This latter aims to study the effect of the uncertainties in the input parameters on the bed geometry.
To check the validity of the implemented model, the numerical results will be compared to experimental data in Chapter 4. A specially dedicated test-facility will be, on that account, presented in the same chapter. Then, the test procedures and measurement techniques will be delineated. Based on the results interpretation, different deposition regimes of solid particles will be identified, and a comparison to the numerical simulations will be shown.
Furthermore, Chapter 5 will outline the influence of the steam production inside the hot debris bed on the particles spreading and on the bed geometry. An experimental investigation will be performed to gain a deeper insight into the self-leveling phenomenology, and to give the present work more breadth. A theoretical investigation of this phenomenon will be performed, and the developed continuum model will be adapted to consider the influence of the coolant boiling on the bed formation process.

Before concluding the work, the major modeling assumptions underlying the developed model will be reviewed in Chapter 6. Knowing the assumptions used in this study and its range of validity will provide us with a good manner to discuss how the model could be optimally used or extended, and which future work may be outlined.
The above-introduced outline of the thesis is depicted with respect to the different stages of SA in Figure 1.5.

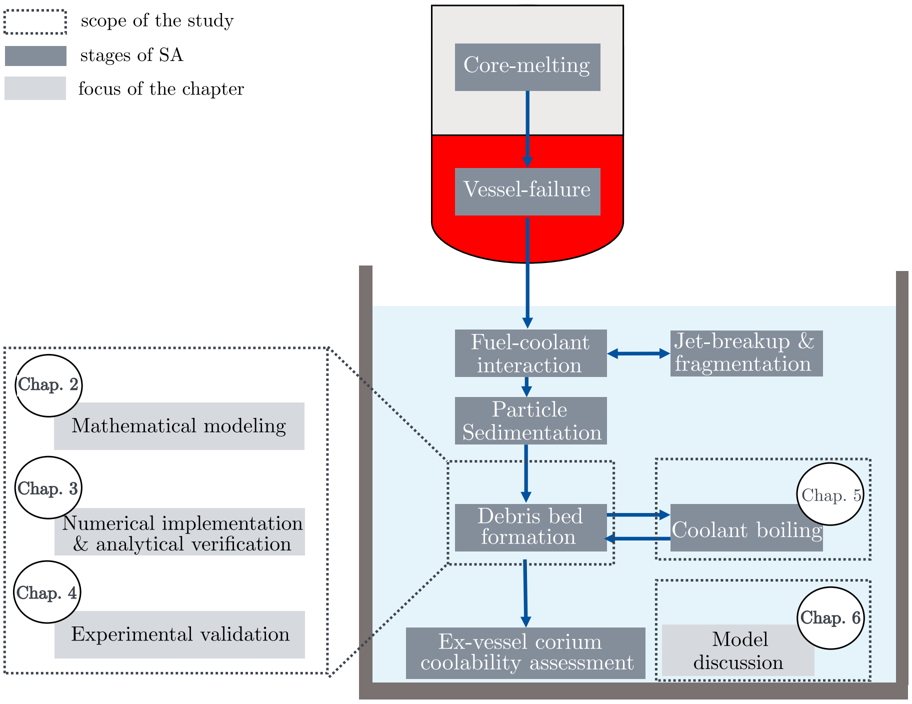

Figure 1.5: The scope of the study in the context of ex-vessel severe accident

2
Theoretical Model

In the present model, it is assumed that the fully fragmented and solidified debris particles are behaving like cohesionless granular material.

2.1 Dynamics of granular flows

Although granular materials are large conglomerations of discrete macroscopic solid particles, they also display characteristics of fluids. A resting granular system can be fluidized with an external energy input, i.e., by the release of potential energy or by agitation on the surface of the heap. During particles interaction through collision and friction, this added energy will be dissipated, and the granular material will come to rest again [54]. Thus, in contrast to drained fluids, when such particles are poured onto a horizontal flat surface, they form a conical pile characterized by the slope angle and do not spread uniformly on that surface.
Due to the complexity of the behavior of granular materials, the understanding of dynamics processes controlling the granular flow is of particular importance for its modeling. Three key processes may be identified: collision and frictional interaction between particles, cohesion, and dilatancy.

- **Inter-particle friction and cohesion:** similar to a block sliding on a rough plane when the inclination angle is greater than the friction angle, the free surface of a granular heap can be inclined at a maximum value corresponding to material's angle of repose. For a dense granular flow, the behavior is well described by the Mohr-Coulomb criterion, which states that the shear stress τ varies linearly with

σ_N, the normal stress, so that:

$$|\tau| = \sigma_N tan(\phi) \tag{2.1}$$

where ϕ is the internal angle of repose. Moreover, the stability of the heap could be increased by introducing cohesion through capillary bridges between the particles. This cohesiveness is often due to the viscosity of the interstitial fluid or to the interactions between particles (i.e., electrostatic forces). As a consequence, an extra finite shear stress c may have to be applied before yield is reached (see Figure 2.2) and the criterion in Equation (2.1) is replaced by:

$$|\tau| = c + \sigma_N tan(\phi) \tag{2.2}$$

For coarse cohesionless materials, the interstitial fluid plays only a minor role and the momentum transfer mechanism is governed largely by the particles interaction. Thus, c is negligible.

- **Inter-particle collision:** in addition to momentum transfer by inter-particle friction, collision between particles provides a mean of exerting an effective granular stress in the material. Due to its high deformation rates, the rapid shearing of granular flows causes collisions between particles, generating random motion between them. Thus, a measure of the fluctuation energy is defined with the so-called granular temperature and many studies on granular materials draw on an analogy with the Chapman-Enskog kinetic theory for dense gases [23]. However, one of the main differences between granular materials and gas molecules is that the collision between solid particles is inelastic, leading to energy dissipation. Several theoretical and experimental works [75] [89][109] [111] have been conducted to study this analogy and to allow a better understanding of the rheological behavior of flowing granular materials. For simple shear flow where uniform velocity gradient, temperature and density are assumed, the theoretical analyses predict the same behavior introduced by Bagnold in his pioneering work [4], namely:

$$\tau_{ij} = \rho_p f_{ij}(\nu) d_p^2 \left(\frac{\partial v_x}{\partial y}\right)^2 \tag{2.3}$$

where τ_{ij} is the stress tensor, ρ_p the particle density, d_p the particle (mean) diameter, $\left(\frac{\partial v_x}{\partial y}\right)$ the local mean shear rate, and $f_{ij}(\nu)$ is a tensor function of the solid fraction ν.

- **Dilatancy:** if an array of compact solid particles are subject to shear deformations, they must ride over one another leading to an expanding in volume of the bulk material (see Figure 2.1). This phenomenon was first termed *dilatancy* by Reynolds in 1885 [99]. Reynolds used the concept of dilatancy to explain the color change of the sand when walking on the seashore, namely that upon stepping over the

> wet sand, it appears to whiten or momentarily dry around his foot. The reasoning was that due to the external stress supplied by his foot, the densely packed sand experiences an increase in volume and, draining water downward to fill the extra void spaces and leaving the surface dry. As his foot is removed, the sand contracts and water rises again to the surface [93].

Detailed reviews and discussion on characteristic properties of granular flows can be found in [33][52][54][60][84][94][108].

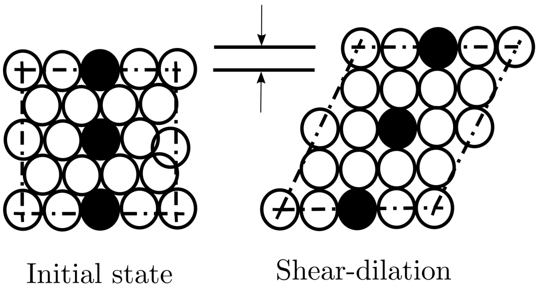

Figure 2.1: Shearing of identical spheres in closest packing

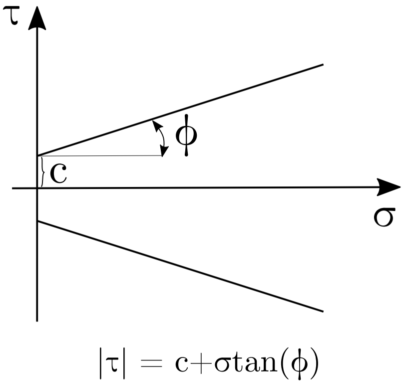

Figure 2.2: General Mohr-Coulomb yield criterion

2.2 Governing and constitutive equations

Similar to granular sand piles, when solid particles are poured onto a horizontal flat surface from a single point, they form a conical shaped pile characterized by the slope angle. The value of this angle stays between two critical values. An avalanche starts to flow when the slope exceeds the angle of movement β_m. The second characterstic angle is defined as the angle of settlement β_s (often called static angle of repose), with $tan(\beta_s)$ taken to be the effective coefficient of dynamic friction in granular flows [82]. These characteristic angles depend on the gravity, the shape and the roughness of the particles, its density, and the coefficient of friction of the material [21] [62]. By exceeding the maximum value of β_m, the pile cannot sustain the steep surface, and a flow of particles occurs within a thin surface layer on the top of a nearly quiescent bulk region [63].

In the present model, it is considered that the non-cohesive granular particles are flowing uni-directionally in a thin surface layer (as shown schematically in Figure 2.3). The mass- and momentum conservation equations in the flowing layer are as follows:

$$\frac{\partial \rho_p}{\partial t} + \frac{\partial (\rho_p v_x)}{\partial x} + \frac{\partial (\rho_p v_y)}{\partial y} = 0 \tag{2.4}$$

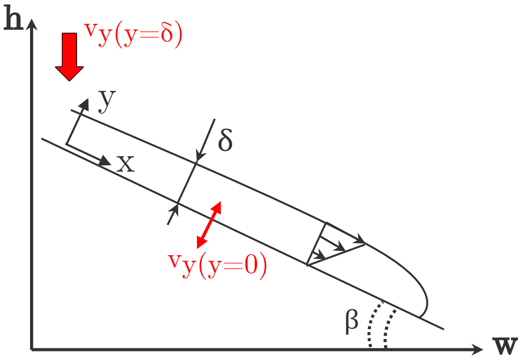

Figure 2.3: Sketch of the flowing layer

$$\frac{\partial\left(\rho_p v_x\right)}{\partial t}+\frac{\partial\left(\rho_p v_x^2\right)}{\partial x}+\frac{\partial\left(\rho_p v_x v_y\right)}{\partial y}+\frac{\partial \tau_{xx}}{\partial x}+\frac{\partial \tau_{xy}}{\partial y}=\rho_p g sin(\beta) \tag{2.5}$$

Where v_x and v_y are the particles velocity components, τ_{xx} and τ_{xy} are the normal and shear stress respectively, and $\beta(x,t)$ is the local angle made by the heap surface with the horizontal.

Plane flow configurations are of focus in this work, so depth integration $(y : 0 \rightarrow \delta)$ over the layer thickness δ reduces the model to one spatial dimension. Since the dilatation of the flowing layer is small in the present slow flows, it is assumed that the bulk density in the layer ρ_p is constant[1] and nearly equal to the bed density. The variation of the normal stress τ_{xx} in the downslope x-direction is also neglected. The integral forms of the conservation laws (2.4) and (2.5) are then:

$$\frac{\partial}{\partial t}\int_0^\delta \rho_p dy+\frac{\partial}{\partial x}\int_0^\delta \left(\rho_p v_x\right) dy+\frac{\partial}{\partial y}\int_0^\delta \left(\rho_p v_y\right) dy=0 \tag{2.6}$$

$$\begin{aligned}\frac{\partial}{\partial t}\int_0^\delta \left(\rho_p v_x\right) dy+\frac{\partial}{\partial x}\int_0^\delta \left(\rho_p v_x^2\right) dy+\frac{\partial}{\partial y}\int_0^\delta \left(\rho_p v_x v_y\right) dy\\ +\cancelto{0}{\frac{\partial}{\partial x}\int_0^\delta \tau_{xx} dy}+\frac{\partial}{\partial y}\int_0^\delta \tau_{xy} dy=\int_0^\delta \rho_p g sin(\beta) dy\end{aligned} \tag{2.7}$$

It can also be assumed that the x-velocity component can be described with the following linear form as:

$$v_x(y)=2u(x,t)\frac{y}{\delta} \tag{2.8}$$

---

[1] In the present model, the effect of dilatancy will be neglected. Actually, volume changes can occur at the instants of flow inception and during particles settling, or due to wall effects [51] [137] [136], but this change is not of great importance within the main flow region and the assumption of a constant density will not influence the model results.

With the above-mentioned assumptions, the leading order depth-integrated equations for the local layer thickness (δ) and the momentum (δu) reduce to:

$$\frac{\partial \delta}{\partial t} + \frac{\partial \left(\delta u\right)}{\partial x} = v_{y_{(y=0)}} - v_{y_{(y=\delta)}} \tag{2.9}$$

$$\frac{\partial \left(\delta u\right)}{\partial t} + \frac{4}{3}\frac{\partial \left(\delta u^2\right)}{\partial x} = \frac{1}{\rho_p}\tau_{xy_{(y=0)}} + g\delta sin(\beta) - 2uv_{y_{(y=\delta)}} \tag{2.10}$$

The first velocity term on the right side of Equation (2.9) represents the absorption and erosion rate of the particles into and from the quiescent heap, while the second term is the velocity of the falling particle from the top.

As proposed by Johnson and Jackson [57], the shear stress in the flowing layer is considered to be the linear sum of the frictional and the collisional stresses, with the frictional forces assumed to be of the Coulombic form, and Bagnold's results [4] [44] [112] are used to model the collisional stress. In the present model, the shear stress is then defined as:

$$\tau_{xy} = -1.5\rho_p \delta d_p \left(\frac{\partial v_x}{\partial y}\right)^2 - \rho_p g \delta cos(\beta) tan(\beta_s) \tag{2.11}$$

Where d_p denotes the average particle diameter and $tan(\beta_s)$ represents the effective coefficient of dynamic friction. This stress definition is also an empirical equation obtained by Orpe and Khakhar [90] from their experimental studies of surface flow in a rotating cylinder. On the other side, the shear stress imposed by the flowing layer on its surface with the static particles is balanced by friction. The shear stress can be then described according to the Mohr-Coulomb failure criterion as:

$$\tau_{xy_{y=0}} = -\rho_p g(\delta + d_p) cos(\beta) tan(\beta_m) \tag{2.12}$$

From Equations (2.11) and (2.12), a direct dependency between the mean velocity (u) and the layer thickness (δ) can be found under the assumption of having a thick layer ($\delta \ggg d_p$):

$$u = \sqrt{\frac{g cos(\beta) sin(\beta_m - \beta_s)}{1.5 d_p cos(\beta_m) cos(\beta_s)}} \cdot \frac{\delta}{2} = \gamma \frac{\delta}{2} \tag{2.13}$$

With the assumption in Equation (2.11), the conservation equations (2.9) and (2.10) can be reduced to the following system:

$$\begin{cases} \dfrac{\partial \delta}{\partial t} + \dfrac{\partial \left(\delta u\right)}{\partial x} = v_{y_{(y=0)}} - v_{y_{(y=\delta)}} \\ \dfrac{\partial \left(\delta u\right)}{\partial t} + \dfrac{4}{3}\dfrac{\partial \left(\delta u^2\right)}{\partial x} = -6d_p\dfrac{u^2}{\delta} - 2uv_{y_{(y=\delta)}} + g\delta\dfrac{sin(\beta - \beta_s)}{cos(\beta_s)} \end{cases} \tag{2.14}$$

The dynamics of the bed-layer-interface $h(x,t)$ can be geometrically deduced from Figure 2.3 as below:

$$\frac{\partial h}{\partial t} = -v_{y_{(y=0)}} cos(\beta) \quad \text{and} \quad \frac{\partial h}{\partial x} = -sin(\beta) \tag{2.15}$$

The equations (2.13), (2.14), and (2.15) define a two-dimensional continuum model for the description of the debris bed formation. The temporal evolution of the bed height as well as the avalanche thickness and the local particles mean velocities can be numerically solved with the indication of the appropriate boundary and initial conditions in regard of the real case conditions.

The equations system (2.14) is a coupled system of two non-linear conservation laws, which can be written in general vector form as:

$$\frac{\partial q}{\partial t} + \frac{\partial f(q)}{\partial x} = S \tag{2.16}$$

with the definition of q and $f(q)$ as:

$$q = \begin{pmatrix} \delta \\ \delta u \end{pmatrix} \quad \text{and} \quad f(q) = \begin{pmatrix} \delta u \\ \frac{4}{3}\delta u^2 \end{pmatrix} \tag{2.17}$$

$q : \mathbb{R}^+ \times \mathbb{R} \rightarrow \Omega$ denotes the state vector of the conserved quantities, $f(q) : \Omega \rightarrow \mathbb{R}^2$ represents the transport-flux in the x-direction, with Ω is the set if the admissible states. The vector S stands for the source terms, and it is defined as:

$$S = \begin{pmatrix} v_{y_{(y=0)}} - v_{y_{(y=\delta)}} \\ -6d_p \frac{u^2}{\delta} - 2uv_{y_{(y=\delta)}} + g\delta \frac{sin(\beta - \beta_s)}{cos(\beta_s)} \end{pmatrix} \tag{2.18}$$

Under the assumption that q is smooth, the conservation equations of the form given by Equation (2.16) can also be written as a *quasi-linear* form:

$$\frac{\partial q}{\partial t} + A(q)\frac{\partial q}{\partial x} = S \tag{2.19}$$

where $A(q) = \partial f/\partial q$ is the Jacobian of the flux vector $f(q)$. Thus, the matrix A reads:

$$A(q) = \begin{pmatrix} 0 & 1 \\ -\frac{4}{3}u^2 & \frac{8}{3}u \end{pmatrix} \tag{2.20}$$

According to the condition (2.23), the matrix $A(q)$ has eigenvalues λ_i and corresponding right eigenvectors $(r^i \mid i = 1, 2)$ given by:

$$\begin{cases} \lambda_1 = 2u \\ \lambda_1 = \frac{2}{3}u \end{cases} \quad \text{and} \quad \begin{cases} r^1 = \begin{pmatrix} 1 \\ 2u \end{pmatrix} \\ r^2 = \begin{pmatrix} 3 \\ 2u \end{pmatrix} \end{cases} \tag{2.21}$$

A quasilinear partial differential equation (PDE) system is said to be *hyperbolic* at the point (q,x,t) if the matrix $A(q,x,t)$ satisfies the hyperbolicity condition at this point.

Definition 2.1 (Hyperbolicity condition). *A linear system of the form:*

$$\frac{\partial q}{\partial t} + A\frac{\partial q}{\partial x} = 0 \tag{2.22}$$

is called hyperbolic if the $(s \times s)$ *matrix* A *is diagonalizable with real eigenvalues.*
The matrix is diagonalizable if a complete set of (non-zero) and linearly independent eigenvectors $r^1, r^2, \ldots, r^s \in \mathbb{R}^s$ *such that:*

$$Ar^i = \lambda_i r^i \quad \textit{for} \quad i = 1, 2, \ldots, s \tag{2.23}$$

Hence, the matrix $R = \left[r^1 \mid r^2 \mid \cdots \mid r^s\right]$ *is nonsingular and has an inverse* R^{-1}*. In this case, the matrix* A *can be written as:*

$$A = R\Lambda R^{-1} \quad \textit{with} \quad \Lambda = \begin{bmatrix} \lambda_1 & & \\ & \ddots & \\ & & \lambda_s \end{bmatrix} \tag{2.24}$$

With this similarity transformation, the matrix A *can be brought to diagonal form and the system (2.22) can be rewritten as:*

$$R^{-1}\frac{\partial q}{\partial t} + \cancelto{I_s}{R^{-1}R}\Lambda R^{-1}\frac{\partial q}{\partial x} = 0 \tag{2.25}$$

with the definition of $W(x,t) \equiv R^{-1}q(x,t)$*, (2.25) takes the form:*

$$\frac{\partial W}{\partial t} + \Lambda\frac{\partial W}{\partial x} = 0 \tag{2.26}$$

The matrix Λ *is diagonal. Then, the PDE system decouples into s independent advection equations for the component* w_i *of* W*:*

$$\frac{\partial w_i}{\partial t} + \lambda_i\frac{\partial w_i}{\partial x} = 0 \quad \textit{for} \quad i = 1, 2, \ldots, s \tag{2.27}$$

Since each λ_i *is real, the solution of (2.22) consists of a linear combination of s waves traveling at the characteristic speeds* $\lambda_1, \lambda_2, \ldots, \lambda_s$*. These characteristic values define the characteristic curves* $X(t) = x_0 + \lambda_i t$ *along which information propagates in the decoupled advection equations.*

In the preceding definition, the PDE system (2.22) consists of a linear problem with constant coefficients. The present model (2.19) involves a Jacobian matrix with spatially-varying coefficients ($A = A\left(q(x)\right)$); nevertheless, the introduced rules can be applied fairly directly and the system is hyperbolic in the definition domain if $A(x)$ is diagonalizable with real eigenvalues at each x in the domain.

Since the matrix A defined in Equation (2.20) is diagonalizable and its corresponding eigenvalues in Equation (2.21) are real, it can be deduced that the system (2.16) is **hyperbolic** over the set of the admissible states:

$$\Omega = \left\{ q \in \mathbb{R}^2 \mid \delta \geq 0, u \in \mathbb{R} \right\} \tag{2.28}$$

3

Numerical Solution

The mathematical model presented in Chapter 2 is based on a hyperbolic system of partial differential equations determining the distribution of the flowing layer depth and the depth-averaged velocity component tangential to the sliding bed. Because of the hyperbolicity of the system, successful implementation of a solver is challenging, notably when large gradients of the physical variables appear, e.g., for a moving front in the flowing layer or possibly formed shock waves and discontinuities during particles deposition.

In recent years there has been a great effort devoted to the development of accurate and efficient numerical methods for the solution of hyperbolic systems. One of the most popular methods is probably the Roe's solver, originally proposed for the approximation of the Euler equations [106]. The main attractive feature of the Roe's solver is its capability to capture discontinuities without any shock-fitting procedure.

In the present chapter, the numerical procedure to solve the debris bed formation model using the Roe-solver will be presented. The Roe-scheme is implemented in FORTRAN, together with a flux limiter for obtaining a second order scheme, which avoids non-physical, spurious oscillations. A numerical study is also conducted to investigate the capability and the efficiency of this solver by comparing it with other numerical methods usually applied in similar problems (for instance the snow avalanche flows [138]). This comparison includes: **(i)** the traditional first-order upstream scheme, and **(ii)** the high-resolution NOC NT-scheme. The implemented Riemann Roe's solver has provided promising results, which are verified with analytic solutions in the steady state. The spatial convergence is also reported and quantified with the use of the grid convergence index (GCI). A sensitivity analysis is then conducted, in order to study the effect of the uncertainties in the input parameters on the bed geometry.

3.1 Numerical methods

3.1.1 The ROE approximate Riemann solver

The Roe-scheme is based on solving a localized Riemann problem to calculate the flux at a given face of the domain.
Recall the system of the governing equations (2.14) in its conservative form:

$$q_t + f_x(q) = S \tag{3.1}$$

Note that the subscripts $()_t$ and $()_x$ denote partial derivatives with respect to t and x respectively. The use of a conservative form of equations is particularly important when dealing with problems admitting shocks or discontinuities in the solution as in the present model. The above equations system (3.1) is discretized on a regular grid using a forward difference scheme for time derivative and a central difference scheme for space derivative as follows:

$$\frac{q_i^{n+1} - q_i^n}{\Delta t} + \frac{f_{i+\frac{1}{2}}^n - f_{i-\frac{1}{2}}^n}{\Delta x} = S_i^n \tag{3.2}$$

By the superscripts $()^n$ are the solutions from previous time step (or from initial conditions at the first time step) denoted, and the solution at the end of the present time step is denoted by the superscript $()^{n+1}$.
The vectors $f_{i+\frac{1}{2}}^n$ and $f_{i-\frac{1}{2}}^n$ denote the convection fluxes at the cell boundaries $\left(x_{i+\frac{1}{2}}\right)$ and $\left(x_{i-\frac{1}{2}}\right)$ respectively:

$$f_{i+\frac{1}{2}}^n = f(x_{i+\frac{1}{2}}^n) \quad \text{and} \quad f_{i-\frac{1}{2}}^n = f(x_{i-\frac{1}{2}}^n) \tag{3.3}$$

The above equation (3.2) can be rewritten as:

$$q_i^{n+1} = q_i^n - \frac{\Delta t}{\Delta x}\left(f_{i+\frac{1}{2}}^n - f_{i-\frac{1}{2}}^n\right) + \Delta t S_i^n \tag{3.4}$$

The nomenclature of grid points and faces are presented schematically in Figure 3.1.

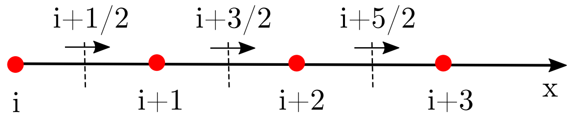

Figure 3.1: Schematic view of the grid and the related nomenclature

An accurate numerical scheme that provides stable simulations of the process occurring in the layer of flowing particles is needed. There is a broad range of finite volume schemes for the solution of hyperbolic systems based on Riemann solvers (Godunov-type schemes) [70][81]. One of the most popular techniques is the Roe-scheme [106] originally designed for the solution of hyperbolic systems without accounting for source terms. It was later modified and improved [43][11][135] to solve general channel flows with source terms (e.g., to solve shallow water equations).
A Riemann problem is present at each interface $x_{i+\frac{1}{2}} = (x_i + x_{i+1})/2$ separating adjacent states x_i and x_{i+1}. The ROE approximate Riemann solver is based on the idea of determining the approximate solution by solving a constant coefficient linear system instead of the original nonlinear system (3.1). The partial differential equations are linearized by considering the Jacobian matrix of the flux function $f(q)$ to be constant in each interval $[x_i, x_{i+1}]$. The *linear* problem reads:

$$\partial_t q + \tilde{A}\left(\tilde{q}\right) \partial_x q = 0 \tag{3.5}$$

To determine the constant coefficient Roe-matrix $\tilde{A}$, evaluated in an average state $\tilde{q}$ for every interval, Roe suggested the following conditions:

- **Condition 1 [conservation]**: $\tilde{A}\left(\tilde{q}\right) \cdot \left[q_R - q_L\right] = f\left(q_R\right) - f\left(q_L\right)$, where subscripts R and L represents the right and left cells of each cell-face $(i + \frac{1}{2})$ respectively. And $q_R = q^R_{i+1/2}$ and $q_L = q^L_{i+1/2}$ are approximations to the states to the left and right of the interface at $(i + 1/2)$.
- **Condition 2 [hyperbolicity]**: the matrix $\tilde{A}$ is diagonalizable with real eigenvalues.
- **Condition 3 [consistency]**: $\tilde{A}\left(q_L, q_R\right) \to f'(\overline{q})$ smoothly as $q_L, q_R \to \overline{q}$.

Note that choosing:

$$\begin{aligned} q_R &= q^R_{i+1/2} = q_{i+1} \\ q_L &= q^L_{i+1/2} = q_i \end{aligned} \tag{3.6}$$

would result in a spatially first order scheme. The scheme is however not limited to first-order accuracy, approximations of second order are discussed in Section 3.1.4.
Condition 3 is necessary to ensure that the Roe matrix is consistent with the exact Jacobian and the linearized solution is recovered from the non-linear one smoothly. **Condition 2** ensures that the new linearized system is truly hyperbolic. **Condition 1** ensures that if a single discontinuity is located at the boundary, then the solution of the linearized problem gives the exact solution to the Riemann problem. For the construction of the (locally) constant matrix $\tilde{A}$, the above-mentioned conditions must be satisfied. It is easy and straightforward to construct the constant matrix to meet condition 1 and 2.

The existing of $\tilde{A}$ satisfying conditions 3 gives:

$$\underbrace{\begin{pmatrix} 0 & 1 \\ -\frac{4}{3}\tilde{u}^2 & \frac{8}{3}\tilde{u} \end{pmatrix}}_{\tilde{A}} \cdot \underbrace{\begin{pmatrix} \delta_R - \delta_L \\ \delta_R u_R - \delta_L u_L \end{pmatrix}}_{\Delta q} = \underbrace{\begin{pmatrix} \delta_R u_R - \delta_L u_L \\ \frac{4}{3}\delta_R u_R^2 - \frac{4}{3}\delta_L u_L^2 \end{pmatrix}}_{\Delta f} \tag{3.7}$$

The exact solution for the averaged particle velocity $\tilde{u}$ is given from the previous equation as:

$$\tilde{u} = \frac{\sqrt{\delta_R} u_R + \sqrt{\delta_L} u_L}{\sqrt{\delta_R} + \sqrt{\delta_L}} \tag{3.8}$$

A representation for the averaged layer thickness can be chosen arbitrarily. Since its selection will not affect the Jacobian matrix $\tilde{A}$, which is only a function of $\tilde{u}$. Similar to the choice of density in the numerical solution of shallow water equations (also known as Saint-Venant equations), the layer thickness will be simply chosen to be:

$$\tilde{\delta} = \sqrt{\delta_R \delta_L} \tag{3.9}$$

The rest of the averaged variables can be calculated with the two averaged conserved $\tilde{\delta}$ and $\tilde{u}$. Once the averaged Roe matrix is obtained for every numerical interface, the Roe's numerical fluxes are computed at each inter-cell boundary $(i + 1/2)$ as:

$$\tilde{f}_{Roe} = \frac{f(q_R) + f(q_L)}{2} - \frac{1}{2}\sum_{n=1}^{2} |\tilde{\lambda}_n| \tilde{\alpha}_n \tilde{r}_n \tag{3.10}$$

with:

$$\tilde{\alpha}_n = \tilde{l}_n (q_R - q_L) \tag{3.11}$$

Note that $\left\{\tilde{\lambda}_1 = 2\tilde{u} \quad , \quad \tilde{\lambda}_2 = \frac{2}{3}\tilde{u}\right\}$ and $\left\{\tilde{r}_1 = (1 \quad 2\tilde{u})^T \quad , \quad \tilde{r}_2 = (3 \quad 2\tilde{u})^T\right\}$ are respectively the averaged eigenvalues and right eigenvectors of the linearized Jacobian matrix $\tilde{A}$. The left eigenvectors $\tilde{l}_n$ verify the condition of normalization with the right eigenvectors.

Definition 3.1 (Normalization condition of left eigenvectors)**.** *A set of left and right eigenvectors* $\{y_m \mid m \in 1, 2\}$ *and* $\{x_n \mid n \in 1, 2\}$ *is said to be orthonormal with respect to the matrix* A *if they verify:*

$$y_m^T x_n = \varsigma_{mn} \quad \textit{and} \quad y_m^T A x_m = \lambda_m \varsigma_{mm} \tag{3.12}$$

with ς_{mn} *denoting the Kronecker delta:*

$$\varsigma_{mn} = \begin{cases} 0 & \textit{if} \quad m \neq n \\ 1 & \textit{if} \quad m = n \end{cases} \tag{3.13}$$

However, there is still a major issue with the classic Roe-scheme since it automatically admits discontinuities into its calculation. In reality, it is not a valid physical solution of the governing equations. The Roe's linearization may lead to non-entropic weak solutions of the equations, due to the approximation of the exact solution of the Riemann problem through constant states separated by discontinuities. According to Harten [46], rarefaction waves at sonic transition points can turn into expansion shocks violating the entropy condition. For the calculation of the numerical flux as expressed in Equation (3.10), the term $\tilde{A} \cdot [q_R - q_L]$ can be regarded as an additional numerical viscous flux which prevents entropy-violating solutions. As shown in Chapter 2, in the basis of the eigenvectors the viscosity matrix is diagonal, namely, $|\Lambda| = diag\left(|\lambda_1|, |\lambda_2|, ..., |\lambda_n|\right)$. Therefore, it is necessary to prevent any eigenvalue λ_i from becoming zero, in order to prevent vanishing viscosity. So a correction to filter this possibility and to modify the absolute value of the eigenvalues when becoming too small is often applied. A good candidate for such corrections is the one suggested by Harten and Hyman [46], which consists of the following smoothing function $Q(\tilde{\lambda})$:

$$Q(\tilde{\lambda}) = \begin{cases} \dfrac{\tilde{\lambda}^2 + \varepsilon^2}{2\varepsilon} & \text{for} \quad |\tilde{\lambda}| < \varepsilon \\ |\tilde{\lambda}| \quad \text{for} & |\tilde{\lambda}| \geq \varepsilon \end{cases} \tag{3.14}$$

with ε being a very small constant parameter defined as:

$$\varepsilon = max\left(0, \tilde{\lambda} - \lambda_L, \lambda_R - \tilde{\lambda}\right) \tag{3.15}$$

The corrected Roe's numerical flux is then given by the following equation:

$$\tilde{f}_{Roe} = \frac{f\left(q_R\right) + f\left(q_L\right)}{2} - \frac{1}{2}\sum_{n=1}^{2} Q(\tilde{\lambda})\tilde{\alpha}_n\tilde{r}_n \tag{3.16}$$

A final remark about the scheme (3.4) is that the time step Δt must satisfy a Courant-Friedrich-Lewy (CFL) type condition [31]:

$$\Delta t = C_{CFL}\frac{\Delta x}{|u^n_{max}|} \tag{3.17}$$

where $0 < C_{CFL} < 1$ is the CFL-factor and u^n_{max} denotes the maximum velocity in the whole physical space for $t = n\Delta t$. From a mathematical point of view, the condition (3.17) ensures that the numerical domain of dependence of the solution is larger than the physical one. From a physical point of view, this condition ensures that the propagation speed of any physical perturbation (e.g., the propagation speed of the particles) is always smaller than the numerical velocity $v_N \equiv \Delta x/\Delta t$. As schematically shown in Figure 3.2, the CFL-condition (3.17) prevents the propagation of any physical signal for more than a fraction of a grid-zone during a single time step and it is therefore a *necessary* condition for stability (and hence for convergence).

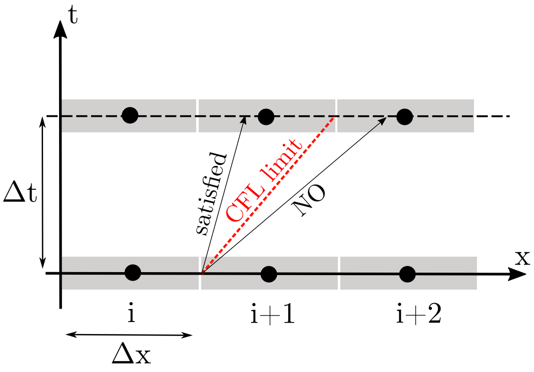

Figure 3.2: CFL condition for first order upwind scheme

3.1.2 Upstream difference scheme

Let's recall the discretization of the equation system in Equation (2.14) on a regular equal-spaced grids as presented previously in Equation (3.4). Assuming small time steps, the non-linear terms can be linearized over the time interval Δt. The value of q_i at the time step $(n+1)$ can be computed with an explicit numerical scheme as follows:

$$q_i^{n+1} = q_i^n - \frac{\Delta t}{\Delta x}\left(f_{i+\frac{1}{2}}^n - f_{i-\frac{1}{2}}^n\right) + \Delta t S_i^n \tag{3.18}$$

Where $f_{i+1/2}^n = f\left(q_{i+1/2}^n\right)$ and $f_{i-1/2}^n = f\left(q_{i-1/2}^n\right)$ denote the convection fluxes at the cell boundaries $x_{i+1/2}$ and $x_{i-1/2}$ respectively. A first-order upstream difference scheme can be computed with the following definitions of the numerical values at the boundaries:

$$\left(q_{i+1/2}^n\right)^{jk} = \begin{cases} \left(q_i^n\right)^k & \text{if} \quad \left(a_{i+1/2}^n\right)^{jk} \geq 0 \\ \left(q_{i+1}^n\right)^k & \text{if} \quad \left(a_{i+1/2}^n\right)^{jk} < 0 \end{cases} \tag{3.19}$$

The upper subscripts $(\cdot)^{jk}$ indicate the cell boundary value of the k^{th}-component of the corresponding vector ($k=1$ for $q=\delta$, $k=2$ for $q=\delta u$) in the j^{th}-equation ($j=1$ for the mass conservation, $k=2$ for the momentum conservation equation). The convective speed $\left(a_{i+1/2}^n\right)^{jk}$ is obtained with the Rankine-Hugoniot jump condition [71]:

$$\left(a_{i+1/2}^n\right)^{jk} = \begin{cases} \dfrac{\left[\left(f_{i+1}^n\right)^j - \left(f_i^n\right)^j\right]}{\left[\left(q_{i+1}^n\right)^k - \left(q_i^n\right)^k\right]} & \text{if} \quad \left(q_{i+1}^n\right)^k \neq \left(q_i^n\right)^k \\ a_{jk} & \text{if} \quad \left(q_{i+1}^n\right)^k = \left(q_i^n\right)^k \end{cases} \tag{3.20}$$

Where a_{jk} are the elements of the Jacobian matrix defined in Equation (2.20).

3.1.3 NOC NT-Scheme

The necessity of a compromise between stable and monotonous first-order finite difference methods and less dissipative second-order difference schemes led to the development of a new family of high-resolution methods [138]. The non-oscillatory central difference scheme introduced by Nessyahu and Tadmor (NOC NT-scheme) [88], which is a second-order extension of the classical Lax-Friedrich scheme LxF [68], will be considered in this section. The main idea of this extension relies on the idea of replacing the first-order piecewise constant solution which is behind the original LxF-scheme with van Leer's MUSCL-type piecewise-linear second-order approximation. Unlike the Roe-scheme, there is no need to solve Riemann problems. This scheme is based on different cell reconstruction techniques. Instead of considering only the values of the cell averages, physical variables will be reconstructed all over the cell [138]. The NOC NT-scheme offers then higher resolution while retaining the simplicity of the Riemann-solver-free approach. The NOC scheme is widely used to solve the Savage Hutter model describing the granular avalanche flows [110] [127]. Due to similarities between our model and the Savage Hutter equations, the NOC-scheme will be implemented in the frame of this work on a staggered grid to test its performance and accuracy compared to the other mentioned schemes.
The linear reconstruction over the cell of the model written in the general vector form in Equation (3.1) is defined as follows:

$$q\left(x,t^n\right) = q_i^n + \left(x - x_i\right)\left(\frac{\partial q}{\partial x}\right)_i^n \tag{3.21}$$

$$= q_i^n + \left(x - x_i\right)\sigma_i^x \tag{3.22}$$

The vector q_i^n denotes the cell average over the interval $\left[x_{i-1/2}, x_{i+1/2}\right]$ and σ_i^x is the discrete slope of q in the x-direction. This cell mean derivative can be determined with a central WENO (weighted essentially non-oscillatory) cell reconstruction [72], or with one of the Total Variation Diminishing (TVD) limiters, discussed in Section 3.1.4. Similar to the Lax-Friedrich scheme, the NOC scheme is a predictor-corrector method based on the use of a staggered grid. A predictor-corrector method consists of two main steps. The first step is to determine the physical values at the cell boundaries at time $t+\Delta t/2$. These values are then used in the corrector step to determine the physical values at the new time $t+\Delta t$ in the cell centers. The NOC-scheme consists in evaluating the conservative variables at the cell boundaries $q_{i+1/2}^{n+1}$ at time $t+\Delta t$ from available values at the cell centers at time $t+\Delta t/2$. Hence, Equation (3.1) is discretized on a regular grid $x_i = i\Delta x (i : 0 \rightarrow l)$ and then linearized over a determined time interval Δt:

$$q_{i+\frac{1}{2}}^{n+1} = \frac{1}{2}\left(q_{i+\frac{1}{4}}^n + q_{i+\frac{3}{4}}^n\right) - \frac{\Delta t}{\Delta x}\left(f_{i+1}^{n+\frac{1}{2}} - f_i^{n+\frac{1}{2}}\right) + \frac{\Delta t}{2}\left(S_{i+\frac{1}{4}}^{n+\frac{1}{2}} + S_{i+\frac{3}{4}}^{n+\frac{1}{2}}\right) \tag{3.23}$$

The cell centers at the time t turn into new cells boundaries at the new time $t+\Delta t$ (see Figure 3.3). As those boundaries were the cell centers, the polynomial reconstruction at these points is smooth. This is only valid for the old time interval $[t+\Delta t[$. This statement allows to determine the transport flux f at the boundaries of the new cells utilizing the Taylor extrapolations in time [127]:

$$f_i^{n+\frac{1}{2}} = f\left(q_i^{n+\frac{1}{2}}\right), \quad q_i^{n+\frac{1}{2}} = q_i^n + \frac{\Delta t}{2}\left(\frac{\partial q}{\partial t}\right)_i^n \tag{3.24}$$

The temporal derivative $\left(\frac{\partial q}{\partial t}\right)_i^n$ is defined as:

$$\left(\frac{\partial q}{\partial t}\right)_i^n = -\left(\frac{\partial f}{\partial x}\right)_i^n + S_i^n = -A_i^n \sigma_i^n + S\left(q_i^n\right) \tag{3.25}$$

Where A is the Jacobian of f. The values of $q_{i+1/4}^n$ and $q_{i+3/4}^n$ are evaluated by means of the reconstruction over a space interval $[x_i, x_{i+1}]$:

$$q_{i+\frac{1}{4}}^n = q_i^n + \frac{\Delta x}{4}\sigma_i^x, \quad q_{i+\frac{3}{4}}^n = q_{i+1}^n - \frac{\Delta x}{4}\sigma_{i+1}^x \tag{3.26}$$

To solve Equation (3.24), the source terms at space coordinate x_i and at time $t + \Delta t/2$ are still needed to be computed. Those values can be calculated with the space-time extrapolation:

$$S_{i+\frac{1}{4}}^{n+\frac{1}{2}} = S\left(q_{i+\frac{1}{4}}^{n+\frac{1}{2}}\right), \quad S_{i+\frac{3}{4}}^{n+\frac{1}{2}} = S\left(q_{i+\frac{3}{4}}^{n+\frac{1}{2}}\right) \tag{3.27}$$

$$\text{with} \begin{cases} q_{i+\frac{1}{4}}^{n+\frac{1}{2}} = q_i^n + \dfrac{\Delta t}{2}\left(\dfrac{\partial q}{\partial t}\right)_i^n + \dfrac{\Delta x}{4}\sigma_i^x \\ q_{i+\frac{3}{4}}^{n+\frac{1}{2}} = q_{i+1}^n + \dfrac{\Delta t}{2}\left(\dfrac{\partial q}{\partial t}\right)_{i+1}^n + \dfrac{\Delta x}{4}\sigma_{i+1}^x \end{cases} \tag{3.28}$$

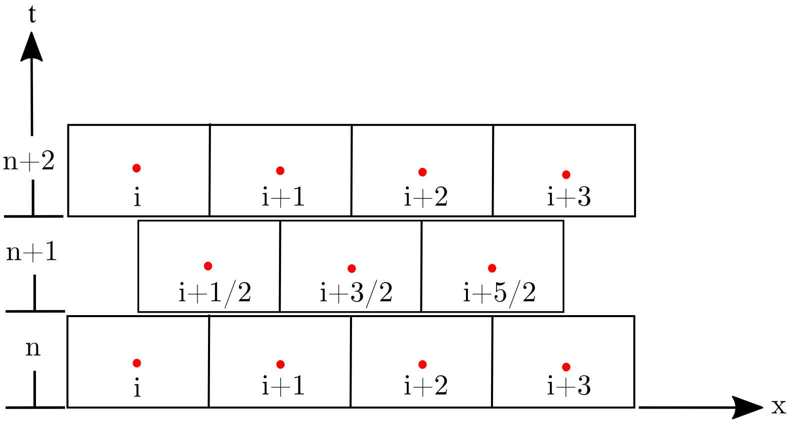

Figure 3.3: Diagram of the staggered grid in x-t-plane

3.1.4 Slope limiters

The physical domain is split into cells $C_j (j : 0 \rightarrow n)$, which are defined as:

$$C_j = \{x \mid |x - x_j| \leq \frac{\Delta x}{2}\} \tag{3.29}$$

In each cell, the conservative variables are stored in the cell center as averaged values. The local value in each position of the domain can be then reconstructed from the nearly known centers assuming a linear interpolation function (in the present case, it is needed to compute the states q_L and q_R at the cell interfaces). To keep the slope of the interpolation at moderate values, a TVD (Total Variation Diminishing) slope limiter is introduced (see Appendix A). A piecewise linear reconstruction of the vector of the conservative variables $\left(q(x,t^n) \mid x \in \left[x_{j-\frac{1}{2}}, x_{j+\frac{1}{2}}\right]\right)$ can be achieved with:

$$q(x,t^n) = q_j^n + (x - x_j)\left(\frac{\partial q}{\partial x}\right)_j^n = q_j^n + (x - x_j)\sigma_j^n \tag{3.30}$$

For a scalar physical variable q_1, i.e., a component of q, the slope limiter σ_j^n is defined as:

$$\sigma_j^n = \phi_j^n \frac{q_{1_{j+1}} - q_{1_j}}{\Delta x} \tag{3.31}$$

with ϕ_j^n is a function of the ratio of the constitutive gradients (i.e., the ratio of backward to forward differences) θ_j^n:

$$\phi_j^n = f(\theta_j^n) \quad \text{and} \quad \theta_j^n = \frac{q_{1_j} - q_{1_{j-1}}}{q_{1_{j+1}} - q_{1_j}} \tag{3.32}$$

There are various selections for the function $\phi_j^n = f(\theta_j^n)$, which can be employed to ensure second-order accurate cell reconstruction (except at points of local extrema) and eliminate unwanted oscillations for the smooth solutions over the cell. If $\phi = f(\theta)$ is defined by the lower boundary of the second-order TVD-region (displayed in blue color in Figure 3.4), it leads to the definition of the so-called Minmod limiter:

$$\phi^{\text{Minmod}} = f(\theta) = max(0, min(1,\theta)) \tag{3.33}$$

Due to its simplicity, the minmod limiter is used extensively in TVD numerical methods. Actually, it consists of a function that selects the smallest number from a set when all have the same sign but is zero if they have different signs.

However, the Superbee limiter is obtained with the upper boundary of the second-order TVD region:

$$\phi^{\text{Superbee}} = f(\theta) = max(0, min(1,2\theta), min(2,\theta)) \tag{3.34}$$

The Woodward limiter lies between the two functions, as defined above:

$$\phi^{\text{Woodward}} = f(\theta) = max(0, min(2, 2\theta, 0.5(1+\theta))) \tag{3.35}$$

An other smoother limiter function was introduced by van Leer [134] as:

$$\phi^{\text{vanLeer}} = f(\theta) = \frac{\theta + |\theta|}{1 + |\theta|} \tag{3.36}$$

In fact, the Superbee and the Minmod limiters are the least and most diffusive of all the presented functions, respectively. The van Leer and Woodward functions lie in-between. All the introduced limiter-functions are implemented as options in the FORTRAN code. Note that the first order scheme is recovered by choosing $\phi = f(\theta) = 0$.

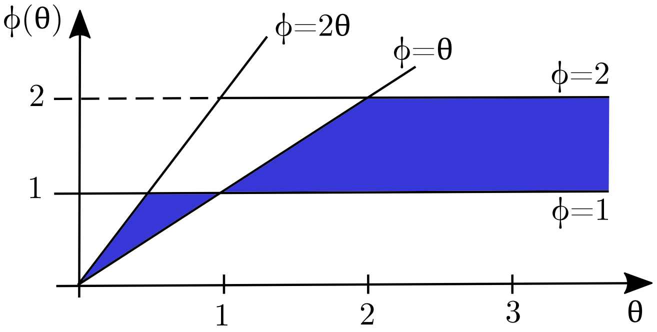

Figure 3.4: Admissible limiter region (in blue) for second-order TVD schemes

3.2 Numerical experiments

3.2.1 Numerical results with the Roe-solver

After the implementation of the presented Roe-solver in FORTRAN, two numerical experiments including the debris bed formation in a closed system (i.e., with closed boundary conditions) and bed formation in an open system (characterized by an open boundary on its right side) as shown in Figure 3.5 are considered in the present section for its numerical evaluation. Both geometries have closed boundaries on the left side, representing the symmetry axis of the bed. For both test cases, a continuous inflow of particles (with $v_{y_{y=\delta}} = -10^{-2}\ \mathrm{m \cdot s^{-1}}$) is considered to be pouring through the opening $\Delta w = 0.055$ m into the systems. The results of the first test case in the closed system are displayed in Figure 3.6, where Figure 3.6a represents the growth of the layer thickness in time, and on the right side, the total height (the sum of h and δ) is depicted in Figure 3.6b. It can be deduced that the bed height and the layer thickness are increasing over time. A moving layer front can be seen as a result of the new deposed particles on the static bed. It is moving down the slope in the form of small avalanches until reaching the bottom,

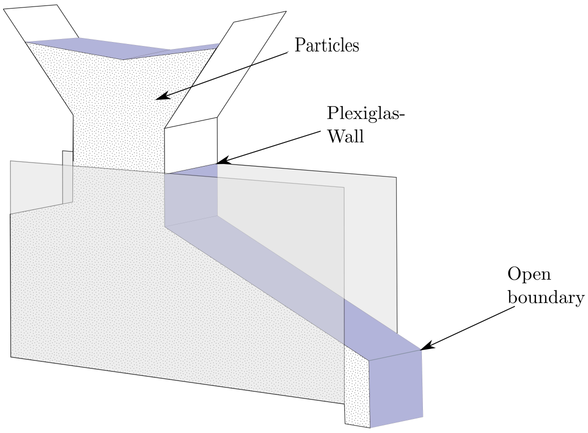

Figure 3.5: Open System and the corresponding boundary conditions

leading to a corresponding increase in the bed height. By reaching the closed boundary on the right side of the system, a reflection on the wall can be obviously seen, and the bed height continues to increase in time, preserving the same angle of settlement.

The results of the second test case in the open system are displayed in Figure 3.7. Similarly to the closed system in the first 528 s, the bed is growing in time until reaching the open boundary, where it remains constant, and the new deposed particles are flowing within a constantly thick layer down the slope without being eroded or absorbed by the static bed, until reaching the open boundary and leaving the system. It can be concluded from Figure 3.7b, that a steady state is achieved

3.2.2 Performance of the various schemes

A numerical example is used to verify the performance of each of the mentioned schemes in Section 3.1. A homogeneous continuous mass of mono-dispersed particles (mean diameter $d_p = 5$ mm) is released at $t = 0$s from the top into the closed system (i.e., closed boundaries) with a constant flowrate $v_{y_{y=\delta}} = -10^{-2}\text{ms}^{-1}$. The poured jet of particles has the width of six cells ($\Delta x = 10^{-3}$). The material has the angle of settlement $\beta_s = 28°$, and the angle of movement is equal to $\beta_m = 40°$. The computation domain is $x \in [0, 1]$ in dimensionless length unit. Figure 3.8 illustrates the growth of the total height $(h + \delta)$ of the formed heap and the variation of the layer thickness over the time in a closed system, obtained with different numerical schemes: ROE-scheme, NOC-scheme, and upwind-scheme.

For the Roe- and upwind-simulations, the angle of the heap increases continuously until reaching the angle of repose. Then the slope remains constant. The height of the heap rises continuously. The simulated bed is composed of a lower heap where particles are either eroded or absorbed and an upper layer of particles sliding down the slope in waves. The simulation results obtained with the ROE- and upwind-scheme are similar. The only

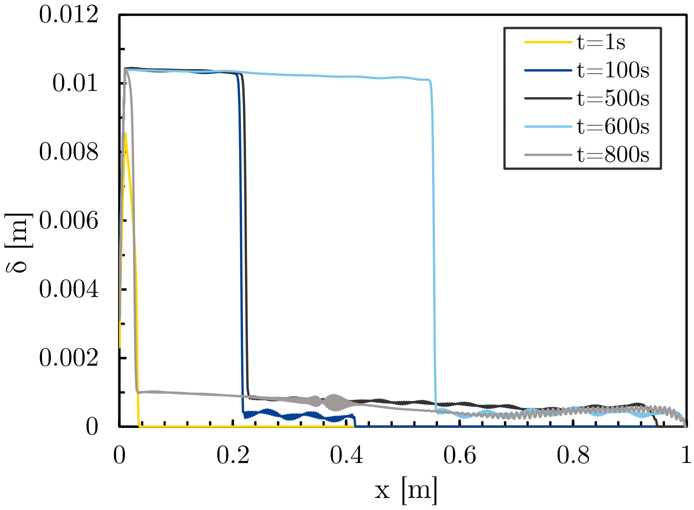

(a) Layer thickness

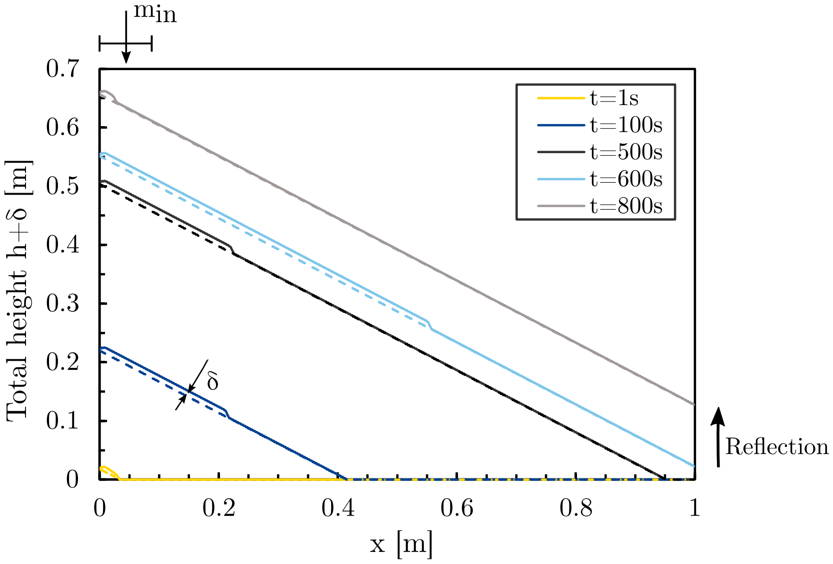

(b) Bed height

Figure 3.6: Bed formation in a closed system

difference between the Roe and upwind scheme consists in the layer thickness for $x = 0$, which is equal to 0 for the upwind case.

However, the simulation results of the NOC-scheme show effects of a very high viscosity: The simulated heap does not rise similar to the other schemes. The formed bed is much flatter and broader, i.e., very low angle of repose. After a short time, the bed leading edge reaches the right boundary of the bed. In general, the family of central schemes suffers from excessive numerical viscosity when a sufficiently small time step is enforced. On top of that comes the effect of the staggered grids. The numerical viscosity in the

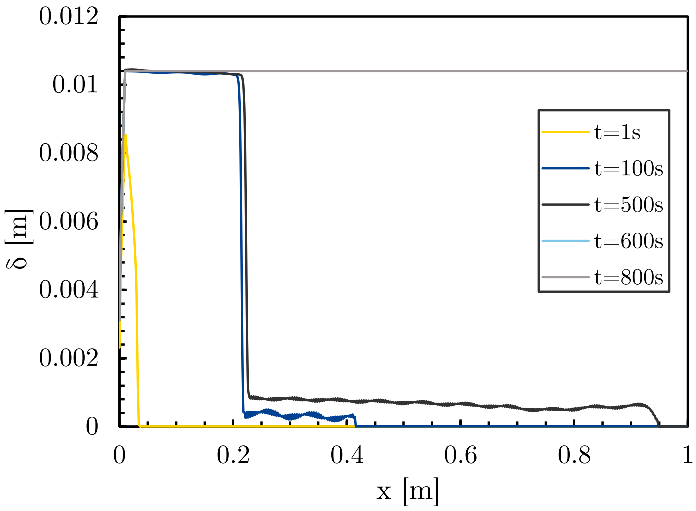

(a) Layer thickness

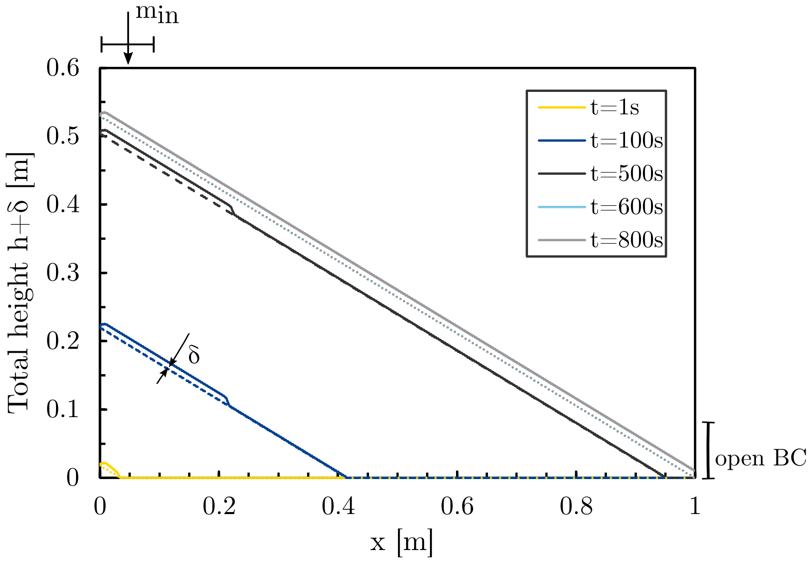

(b) Bed height

Figure 3.7: Bed formation in an open system

NOC-scheme is of order $\mathcal{O}(\Delta x^{2r}/\Delta t)$. Better results could be achieved by increasing the time step Δt, hence by lowering the amount of numerical viscosity, as shown in Figure 3.9. Although, it is still more diffusive than the Roe-solver. The NOC-scheme is based on a staggered grid, which guarantees good results by chocks and discontinuities but it can lead to high diffusive results. An alternation between the successive staggered grids is required due to the specific structure of this grid, which leads to an additional viscosity.

The computed numerical experiments demonstrated that the main disadvantage of the

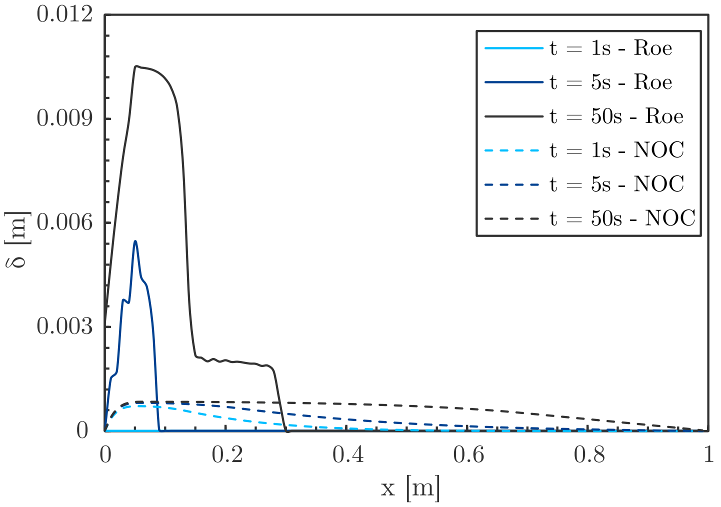

(a) Layer thickness

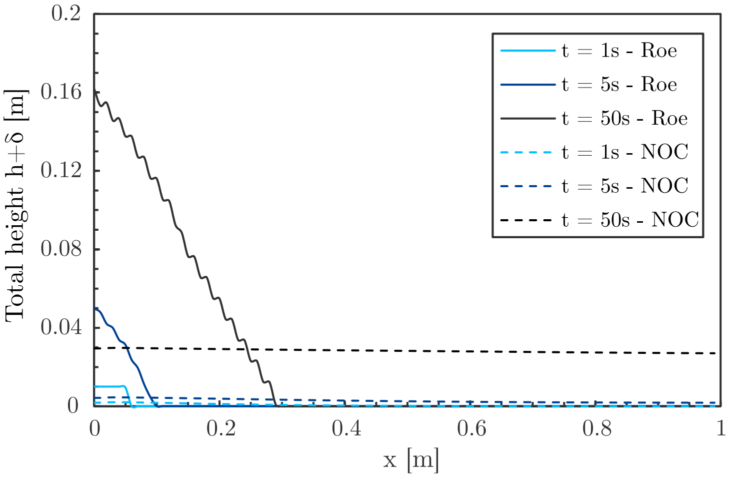

(b) Bed total height $h + \delta$

Figure 3.8: Comparison between the Roe-solver and the NOC-scheme

high-order NOC-scheme, as proposed by Nessyahu and Tadmor, lies in its large numerical dissipation in the used staggered grid. A non-staggered and hence less dissipative version of the NOC-scheme; as presented by Jiang et al. in [55]; may lead to more accurate results of the bed formation process. For the present work, it can be concluded that the Roe-solver is sufficiently good for delivering satisfying results of the bed formation process. Furthermore, the Roe-method requires less storage than the NOC-scheme. By avoiding staggered meshing, where we have to alternate between two staggered grids, which is mainly cumbersome near the boundaries, the Roe-scheme together with the cell

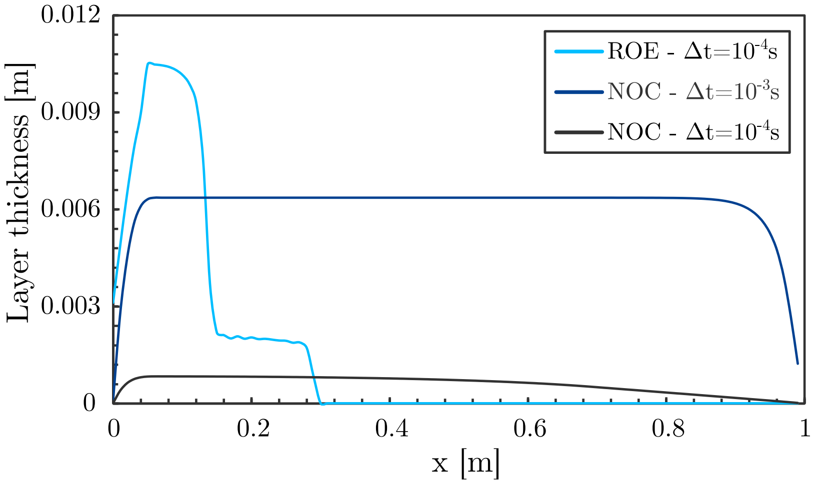

Figure 3.9: Layer thickness in a closed system with different schemes (ROE-scheme, NOC-scheme) and different time steps ($\Delta t = 10^{-3}$s, $\Delta t = 10^{-4}$s)

reconstruction techniques offers more simplicity in the implementation without sacrificing the high resolution or the accuracy.

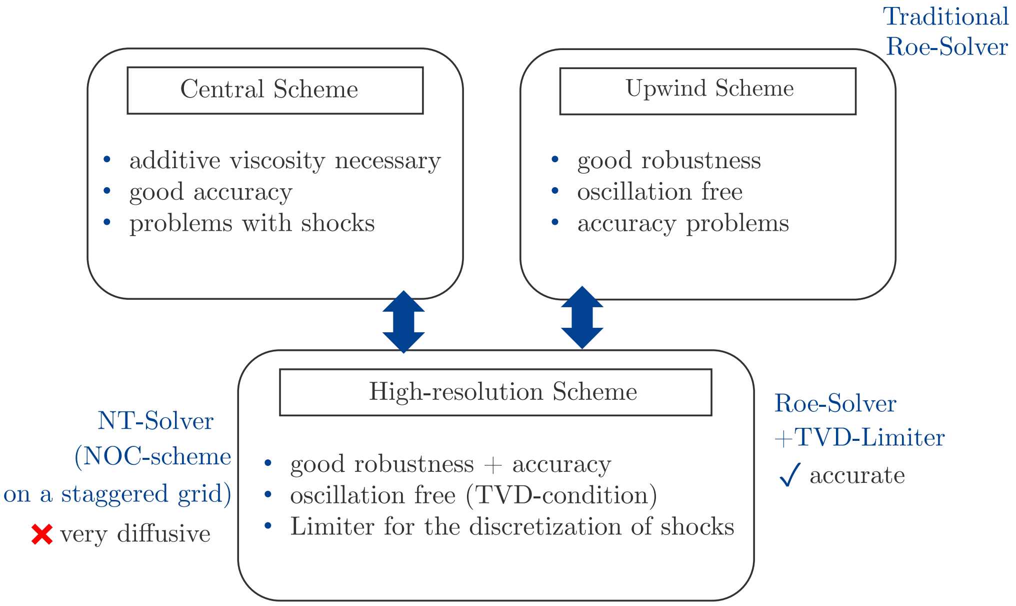

Figure 3.10: Summary of the used numerical methods

3.3 Numerical verification

In its guidelines [V&V 10-2006] the ASME, American Society of Mechanical Engineers, defines the verification as "*the process of determining that a computational model accurately represents the underlying mathematical model and its solution.*" Verification addresses the question, "are we solving the equations correctly?". Hence, verification implies a comparison with reference equation solutions or with analytic solutions, if they exist.

3.3.1 Qualitative comparison

In this section, it will be first verified if the performed simulations in Section 3.2.1 adhere to the laws of physics. It is obvious that the newly deposed particles from one single point form a delta-shaped bed characterized by a typical angle of repose (which depends on the material properties [see Figure 3.6]). By exceeding a maximum value for this angle of repose, the particles will flow within a thin layer on the top of the stationary heap in the form of "*episodic avalanches.*" If the flow hits the closed boundary condition, it will get stopped from the wall leading to particles accumulation on this side. In the case of open boundaries, the bed will remain stationary, and the newly deposed particles will leave the system. These observations are qualitatively in a perfect agreement with the physical phenomena expected to be seen in the reality and with the assumptions taken to describe mathematically the particles dynamics and the bed formation process (see Chapter 2). These observations will also be validated in Chapter 4 with experimental data and observations.

3.3.2 Analytical solution

As shown in Section 3.2.1, the height of the bed in an open system will remain constant after a certain time. When reaching the open boundary, a steady state is achieved. This state is characterized by a constant thickness and constant particles velocity in the flowing layer.
In a steady state ($\partial\delta/\partial t = 0, \partial u/\partial t = 0$) and according to Equation (2.13) (for sufficiently thick layer), the conservation equations system (2.14) is simplified to the following system:

$$\begin{cases} \gamma\delta\dfrac{\partial\delta}{\partial x} = v_{y_{(y=0)}} - v_{y_{(y=\delta)}} \\ \gamma^2\delta\dfrac{\partial\delta}{\partial x} = -g\dfrac{sin(\beta_m - \beta)}{cos(\beta_m)} - \gamma v_{y_{(y=\delta)}} \end{cases} \tag{3.37}$$

Combining both equations of the system yields:

$$v_{y_{(y=0)}} = \frac{-gsin(\beta_m - \beta)}{\gamma cos(\beta_m)} \tag{3.38}$$

Figure 3.7b shows the solution with the Roe-solver of the total height $(h+\delta)$ growth over time. In this numerical experiment, a steady state is achieved for $t > t_c = 528s$, where particles are neither eroded nor absorbed $\left(v_{y_{(y=0)}} = 0\right)$. According to Equation (3.38), the angle β should be constant and equal to β_m and the particles are flowing with a constant velocity in a constantly thick layer $(\partial\delta/\partial x = \partial u/\partial x = 0)$. These results are satisfyingly confirmed with the observations of the present numerical experiment.
Furthermore, it can be concluded that the flow rate of the poured particles $\dot{m}_{in}$ into the system through the opening Δw is equal to the flow rate of the flowing particles in the layer on the top of the steady heap. The layer thickness in the steady state can be analytically solved as follows:

$$|v_{y_{(y=\delta)}}|\Delta w = \delta u \Longrightarrow \delta_{analytic} = \sqrt{\frac{2|v_{y_{(y=\delta)}}|\Delta w}{\gamma}} \tag{3.39}$$

As shown in Figure 3.11, the numerical simulations with the Roe-solver are in excellent agreement with the analytical solution in Equation (3.39).

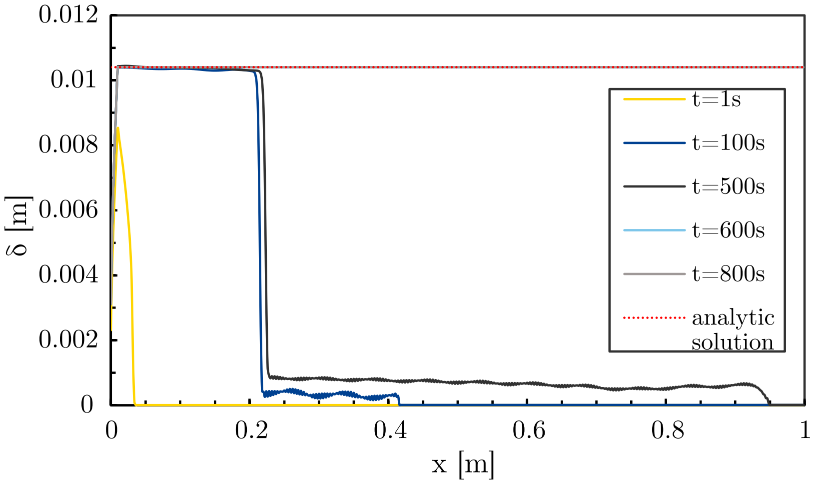

Figure 3.11: Comparison of the numerical simulations and the analytic solution in an open system

3.4 Discretization error analysis

Grid convergence study always plays a fundamental role in verifying the reliability of the numerical models. In general, error types, that could be quantified in verification activities include unacknowledged errors (including the usage or the computer programming errors), and the acknowledged errors (examples include the modeling errors, round-off error, far-field boundary error, temporal convergence error in time-dependent simulations, and grid convergence [or discretization] error). The latter error source is the focus of the present section.

Discretization errors occur from the approximation of the derivatives in the governing equations as finite differences in a discrete domain of space. As the mesh is refined, and the grid spacing tends to zero, the numerical model will approach the continuum representation of the equations, and the spatial discretization errors should asymptotically tend to zero, but it comes with an increased computational cost. One of the most reliable methods for the quantification of the spatial convergence errors are a posteriori approaches based on Richardson extrapolation [100] [101]. A summary of these methods is presented by Roache in his book [104]. He has also suggested a grid convergence index GCI as a uniform manner for reporting the results of grid refinement studies and providing error bars of the numerical solutions) [102]. In fact, the grid convergence study is of most concern to the users of CFD-codes applied on complex geometries and grids, because it gives an evaluation of the grid quality. Indeed, in the present case with simple grid, a refinement study is conducted as a part of the verification process to quantify the numerical error bands which will serve for the validation activities and as a mean to study the order of convergence and accuracy of the implemented solver, since errors may develop in different positions of the calculation domain due to presence of discontinuities and shocks.

3.4.1 Mesh refinement method and Richardson extrapolation

The recommended method for discretization error estimation is the Richardson extrapolation (RE), also known as h^2-extrapolation. It was first used by Richardson in 1910 [100], and later embellished in 1927 [101]. It has been widely investigated and generalized by many authors [22][34][35][102][103][104][107].

The discretization error (ε_h) for a solution variable f on a mesh with spacing h can be formally defined as the difference between the exact solution to the mathematical model $\tilde{f}$ and the numerical solution f_h to the discrete equations:

$$\varepsilon_h = f_h - \tilde{f} \tag{3.40}$$

Here is a brief presentation of the main features of Richardson extrapolation. The RE-method is based on Taylor series expansion of the numerical simulation for a uniform mesh:

$$f_h = \tilde{f} + \sum_{k=1}^{\infty} C_k h^k \tag{3.41}$$

with:

$$C_k = \frac{1}{k!}\frac{\partial f_h^k}{\partial^k h} \tag{3.42}$$

The functions C_k are independent of the grid spacing h and they represents the k^{th}-order error term coefficient. For a formally second-order accurate numerical scheme, the C_1 coefficient will be zero and the general error expansion becomes:

$$\varepsilon_h = f_h - \tilde{f} = C_2 h^2 + C_3 h^3 + \mathcal{O}\left(h^4\right) \tag{3.43}$$

The Richardson extrapolation (3.43) can be generalized to p^{th}-order and the discretization error expansion becomes:

$$\varepsilon_h = f_h - \tilde{f} = C_p h^p + C_{p+1} h^{p+1} + C_{p+2} h^{p+2} + \cdots \tag{3.44}$$

Computing the quantity f on two grids systematically refined of spacing h_1 and h_2, with $h_1 = h$ being the finer (smaller) spacing. The grid refinement factor is defined as the ratio of the coarse to the fine spacing as:

$$r = \frac{h_2}{h_1} > 1 \tag{3.45}$$

and the coarse grid spacing can thus be written as $h_2 = rh_1 = rh$. The error equations on the two nested grids can be written as:

$$\begin{aligned} f_1 = f_h &= \tilde{f} + C_p h^p + \mathcal{O}\left(h^{p+1}\right) \\ f_2 = f_{rh} &= \tilde{f} + C_p \left(rh\right)^p + \mathcal{O}\left(h^{p+1}\right) \end{aligned} \tag{3.46}$$

Combining both equations in(3.46) by eliminating the C_p-coefficient and neglecting the higher-order terms, an approximation of the exact solution at zero grid spacing $\tilde{f} = f_{\Delta x=0}$ (or *generalized Richardson extrapolate*) results in:

$$\tilde{f} = f_{\Delta x=0} \cong f_h + \frac{f_h - f_{rh}}{r^p - 1} \tag{3.47}$$

This estimate $f_{\Delta x=0}$ is considered generally a $(p+1)$-order accurate estimate of the exact solution to the mathematical solution unless additional error cancellation occurs in the higher-order terms.

In Equation (3.47), the correction of $f_1 = f_h$ is obviously an error estimator of the fine grid solution. Expressing this as an *estimated fractional error* E_1 for the fine grid solution:

$$E_1 = \frac{\epsilon}{r^p - 1} \tag{3.48}$$

with ϵ being the relative error:

$$\epsilon = \frac{f_2 - f_1}{f_1} \tag{3.49}$$

The actual fractional error A_1 of the fine grid can be expressed as:

$$A_1 = \frac{f_1 - f_{\Delta x=0}}{f_{\Delta x=0}} \tag{3.50}$$

Using Equations (3.47)-(3.50), the actual fractional error can be expressed as:

$$A_1 = E_1 + \mathcal{O}\left(h^{p+1}, E_1^2\right) \tag{3.51}$$

Thus, the estimated fractional error E_1 is an *ordered error estimator*, i.e., an ordered approximation to the actual fractional error of the fine grid solution. E_1 is a good approximation of the discretization error when the solutions f_1 and f_2 were obtained with good accuracy, i.e., when $E_1 \ll 1$.
On the other hand, the quantity ϵ in Equation (3.49), which is commonly reported in grid refinement studies, should not always be used as an error estimator since it does not take into account r and p. This quantity could be made (artificially) small, just by choosing a grid refinement $r \to 1$.

A final remark about the Richardson extrapolation is that several assumptions are required in order to perform this method straightforwardly and ensure that the Richardson extrapolation estimates the exact solution to the mathematical model:

- **Assumption 1**: Since Richardson extrapolation is based on a Taylor series representation as indicated in Equation (3.41), f has to be a smooth solution of the exact differential equations. The coefficients C_k defined in Equation (3.42) are functions of the solutions derivatives. The RE-method will tend to break down in regions of discontinuity in any of the dependent variables or their derivatives. The *observed* order of accuracy can be reduced to lower order in the presence of discontinuity or singularities, regardless of the *formal* (theoretical) order of accuracy of the numerical model [5] (see Section 3.4.5).
- **Assumption 2**: The grid spacing Δx is small enough to ensure that the leading-order error is dominating the total discretization error. This is also called the asymptotic range of discretization, in which the convergence is monotone [104] (see Section 3.4.3).
- **Assumption 3**: The formal order of grid convergence p_f is known a priori, and it is empirically demonstrated by the computer code.

3.4.2 Observed order of accuracy

It must be mentioned that a numerical code of *formal (theoretical) order* p_f, does not necessarily mean that the computational result will also have the same order p_f. In fact, the boundary conditions, the solver characteristics, and the mesh will influence this theoretical value so that the observed order of accuracy p will likely be lower. In order to ensure a reliable model verification, it is highly advisable always to ascertain the real observed order and use it for the Richardson extrapolation.
Recall the error expansion for the p^{th}-order accurate scheme given by Equation (3.44):

$$\varepsilon_h = C_p h^p + \mathcal{O}\left(h^{p+1}\right) \tag{3.52}$$

Neglecting higher order terms and applying the logarithm function on both sides of Equation (3.52):

$$\mathrm{Ln}\left(\varepsilon_{\mathrm{h}}\right) = \mathrm{Ln}\left(\mathrm{C_p}\right) + \mathrm{p} \cdot \mathrm{Ln(h)} \tag{3.53}$$

For sufficiently available data, the order of convergence p can be then graphically obtained from the slope of the curve of $\mathrm{Ln}(\varepsilon_h)$ vs. $\mathrm{Ln}(h)$ (or from its fitting curve). When the exact solution is not known, the order of convergence can be directly evaluated from three numerical solutions $\{f_{h_1}, f_{h_2}, f_{h_3}\}$ computed on systematically-refined meshes with a constant refinement ratio r:

$$\begin{aligned} f_{h_1} &= \tilde{f} + C_p h^p + \mathcal{O}\left(h^{p+1}\right) \\ f_{h_2} &= \tilde{f} + C_p \left(rh\right)^p + \mathcal{O}\left(\left(rh\right)^{p+1}\right) \\ f_{h_3} &= \tilde{f} + C_p \left(r^2 h\right)^p + \mathcal{O}\left(\left(r^2 h\right)^{p+1}\right) \end{aligned} \tag{3.54}$$

If the higher order terms are sufficiently small, the subtractions of the numerical solutions yield:

$$\begin{aligned} \varepsilon_{32} &= f_{h_3} - f_{h_2} = C_p r^p h^p \left(r^p - 1\right) \\ \varepsilon_{21} &= f_{h_2} - f_{h_1} = C_p h^p \left(r^p - 1\right) \end{aligned} \tag{3.55}$$

The observed order of accuracy can then directly evaluated with the following function:

$$p = \frac{\mathrm{Ln}\left(\dfrac{\mathrm{f_{h_3}} - \mathrm{f_{h_2}}}{\mathrm{f_{h_2}} - \mathrm{f_{h_1}}}\right)}{\mathrm{Ln(r)}} = \frac{\mathrm{Ln}\left(\dfrac{\varepsilon_{32}}{\varepsilon_{21}}\right)}{\mathrm{Ln(r)}} \tag{3.56}$$

When the three numerical solutions do not converge monotonically as the grid is refined, then $\left(\dfrac{\varepsilon_{32}}{\varepsilon_{21}} < 0\right)$ and the definition (3.56) is undefined. This issue of oscillatory (non-monotonic) convergence is not occurring in any of the simulation cases. A further discussion on non-monotonic convergence can be found in [22].

3.4.3 Asymptotic range of convergence

One of the key requirements for the reliability of the discretization error estimation is that the grid is sufficiently refined such that the numerical solutions are in the asymptotic range of discretization. Examining the discretization error expansion defined in Equation (3.44), the asymptotic range is achieved when the spacing h is sufficiently small that the h^p-term is much larger than all of the higher-order terms combined. That yields a constancy of C_p:

$$C_p = \frac{\varepsilon}{h^p} \tag{3.57}$$

Another check of the asymptotic range will be introduced in the following section.

3.4.4 Grid convergence index

As introduced in Sections 3.4.1 and 3.4.2, when the observed order of convergence matches the formal order, then one can have high confidence in the traditional error estimation and the error estimate can be used to correct the numerical solution. However, in the most common cases there is a difference between the observed and the formal order of convergence, the error estimate is not more reliable, and it should be converted into a numerical uncertainty.

Roache [102] proposed the grid convergence index (GCI) as a method for uniform reporting of grid refinement studies and a consistent manner to provide an error or uncertainty band for the numerical solution. The GCI is based on the based upon the mesh refinement error estimator derived from the generalized Richardson method. It measures an error band (in percentage) on how far the computed solution is away from the asymptotic numerical value. A small value of GCI indicates therefore that the computation is within the asymptotic range of convergence.

For the computation of GCI, only two levels of grid refinements are needed. However, it is highly recommended to use at least three systematically-refined grids in order to estimate the actual order of convergence and to check that the solution is within the asymptotic range. The GCI is defined for the fine grid solutions f_1 and f_2 as [102]:

$$GCI = \frac{F_s}{r^p - 1} \left| \frac{f_2 - f_1}{f_1} \right| \tag{3.58}$$

where $F_s = 1.25$ is a factor of safety[1].

It is important that the computed solutions on each grid level are in the asymptotic range of convergence. In addition to the condition (3.57), that can also be checked with the GCI values over three consecutively refined grids 1, 2, and 3:

$$\frac{GCI_{23}}{r^p GCI_{12}} \rightarrow 1 \tag{3.59}$$

3.4.5 Examples of grid convergence studies

Assessing the numerical accuracy of the implemented code is now possible with the use of the techniques of the spatial convergence study introduced in the last sections. Five systematically-refined grids are then used in the following examples, in which the considered space domain ($x \in [0, 4.5]$) will be divided in twice the number of cells in the previous grid (with constant refinement ratio $r = 2$). The simulations are conducted with the same parameters mentioned in Section 3.2. In the present study, three different results will be considered: the maximal bed height, the bed height at $x = 1.26$ and the bed width. Table 3.1 summarizes the grids information where the last line indicates the spacing of each mesh normalized by the spacing of the finest grid Grid_1 (which is equal to $\Delta x = 5.625 \cdot 10^{-3}$).

---

[1] When solutions on only 2 grids are available $F_s = 3$. For comparisons over three or more grids $F_s = 1.25$ [107].

Table 3.1: The different used grids with a constant refinement ratio

Grid	1	2	3	4	5
Normalized grid spacing	1	2	4	8	16

Grid convergence study for the maximal bed height

The maximal bed height h_{max} with varying grid spacing is plotted in Figure 3.12a. As the grid spacing reduces, the bed height approaches an asymptotic zero-grid spacing value. The observed order of convergence at this point $x = 0$ can be determined from the plotted values of grids 1, 2 and 3 (see Equation (3.56)):

$$p = \mathrm{Ln}\left(\frac{\mathrm{h_{max_3}} - \mathrm{h_{max_2}}}{\mathrm{h_{max_2}} - \mathrm{h_{max_1}}}\right)/\mathrm{Ln(r)} = 1.66 \tag{3.60}$$

Note that the calculated order of convergence is different from the formal order $p_f = 2$ of the implemented Roe-solver. This difference is due to the presence of discontinuities and chocks at this position because of the deposed particles flow. Through applying the Richardson extrapolation (as defined in Equation (3.47)) using the two finest grid, the maximal bed height at zero grid spacing can be estimated as:

$$h_{max_{\Delta x=0}} = h_{max_1} + \frac{h_{max_1} - h_{max_2}}{r^p - 1} = 0.902 \tag{3.61}$$

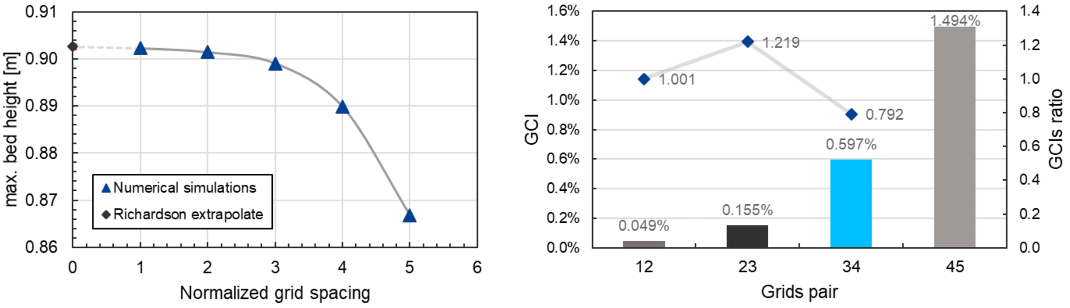

(a) Richardson extrapolation

(b) GCI and GCIs ratio

Figure 3.12: Grid convergence study for the top bed height

The GCI values of the different used grid are summarized in Figure 3.12b. The GCIs ratio between two consecutive refinements can be defined as the ratio of the actual GCI value to the value of the previous coarser grid multiplied by r^p. Through the check of the indices ratio gives:

$$\frac{GCI_{23}}{r^p \cdot GCI_{12}} = 1.001 \rightarrow 1 \tag{3.62}$$

It can be clearly seen according to Equation (3.62) that the determined solutions are within the asymptotic range of convergence. Based on this study it can be concluded that the bed height $(t = 300s, x = 0)$ with the mentioned conditions is estimated to be 0.902 with an error band of 0.049%.

Grid convergence study for the local bed height at $x = 1.26$

The same approach will be then applied for the calculation of the bed height at $x = 1.26$. The calculated values are summarized in the following Figure 3.13a.

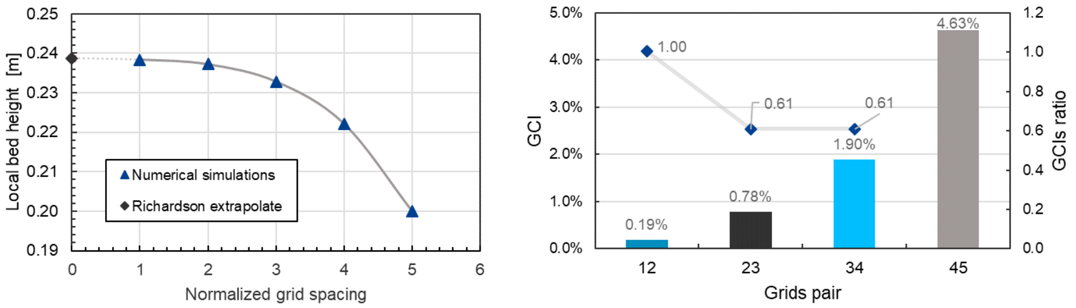

(a) Richardson extrapolation

(b) GCI and GCIs ratio

Figure 3.13: Grid convergence study for the bed height at $x = 1.26m$

The order of convergence in this position is determined from the observed results as follows:

$$p = \mathrm{Ln}\left(\frac{\mathrm{h}_3 - \mathrm{h}_2}{\mathrm{h}_2 - \mathrm{h}_1}\right) / \mathrm{Ln(r)} = 2 \tag{3.63}$$

The order of convergence is equal to the theoretical formal order. In fact, unlike the interval of falling particle flow, there are no discontinuities and chocks in this considered position. The Richardson extrapolate at zero grid spacing is estimated to be $h_{\Delta x=0}(x = 1.26) = 0.239$. The GCIs values are computed and summarized in Figure 3.13b. From the calculated GCIs ratio, it can be concluded, that the performed simulations with the two finest grids are within the asymptotic range. Based on this study, the bed height for $(t = 300s, x = 1.26)$ is estimated to be 0.239 with an error band of 0.19%.

Grid convergence study for the bed width

The last considered evaluation variable is the bed width W, which is summarized for the different refinements in Figure 3.14a. The order of convergence in this position is computed as:

$$p = \mathrm{Ln}\left(\frac{\mathrm{W}_3 - \mathrm{W}_2}{\mathrm{W}_2 - \mathrm{W}_1}\right) / \mathrm{Ln}(\mathrm{r}) = 1 \tag{3.64}$$

Due to the different signs of slope gradients in the considered field, the value of the Minmod-Limiter is then equal to zero. Therefore, the theoretical order of the numerical model on the point with the maximal width will be reduced to 1, which is in agreement with the determined order of convergence in Equation (3.64). Figure 3.14b summarizes the determined grid convergence indices, where it can be proved that the asymptotic range is achieved. Based on this study it could be concluded that the bed width (for $t = 300s$) is estimated to be equal to 1.62 with an error band of 0.44%.

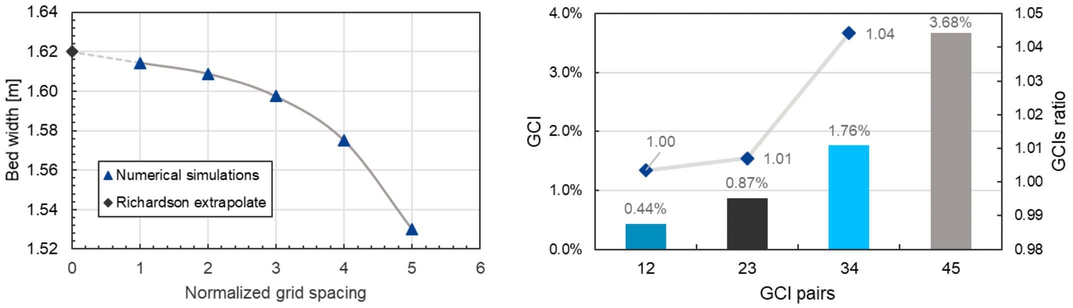

(a) Richardson extrapolation

(b) GCI and GCIs ratio

Figure 3.14: Grid convergence study for the bed width

By means of the grid convergence study and GCI, it is possible not only, to evaluate the influence of the grid refinement on the provided numerical results and check the local order of convergence, but also to get error bands, which are useful for the validation of the model with experimental data.

3.5 Uncertainties and sensitivity analysis

Sensitivity and uncertainty analysis are the main instruments for dealing with the scarce knowledge of the input parameters used in numerical models.
Uncertainty is defined in *AIAA Guidelines* as:

- **Uncertainty**: *a potential deficiency in any phase or activity of the modeling process that is due to the lack of knowledge [AIAA G-077-1998]*

In fact, uncertainty is only a potential deficiency which may or may not be present during the modeling/simulation process. It arises from the scarce knowledge of the physical system of interest (e.g., not well-defined boundary and initial conditions, unknown material properties in the (physical) state of interest) or from inherent variations of the material data. The sources of uncertainties can be thus singled out and represented as randomly distributed functions (i.e., probabilistic distributions) using Monte Carlo simulations, or they can be simulated using a known range of values with the sensitivity analysis.

In this section, the sensitivity analysis has the role in analyzing the influence of aleatory uncertainties in physical input parameters on the prediction of the bed height, and to quantify the most significant contributors to uncertainty in model responses

There is no agreement in the literature when sensitivity analysis should be performed. Roache [104] states that it should be performed only after model validation with experimental data. On the other hand, the ASME suggests in its guidelines, that the uncertainties should be quantified and classified prior to model validation to elucidate the model characteristics that will be important to monitor during experimental tests, and it can be revisited if necessary following the model validation. With the findings from the sensitivity studies, it is possible to analyze to which parameters are the model outputs highly sensitive. By this means, the validation experiment could be effectively designed to exert more control over this particular input a priori, saving a considerable amount of time and effort. The latter point of view will be adopted in the present work, and the sensitivity study is performed prior to experimental validation for the reason mentioned previously, but should also be considered as an integral component of the entire verification and validation (V&V) process.

3.5.1 Ranges and distributions of input parameters

In this section, the aim is to consider all the influencing input parameters for the debris bed formation model and establish their possible ranges and variations, relying on the present knowledge of the processes occurring in the course of reactor severe accidents. The sensitivity analysis is carried out with the variation of the mean particle diameter d_p, the velocity of the falling particles $v_{y_{y=\delta}}$, the jet diameter Δw (as a multiplicity of a constant mesh width Δx), the angle of settlement β_s, and the angle of movement β_m. Table 3.2 summarizes these input parameters together with the probable ranges and the associated distribution functions. The choice of these ranges was set according to the distribution functions and physical properties obtained in different experiments and studies (such as [7] [9] [10] [105], FARO-experiments on melt jet/water mixing and quenching behavior [76] [77] [78], and DEFOR-experiments [66] [67]).

Generally, it can not be assumed that all the parameters are stochastically independent of each other. Therefore, a (population-related) dependency between the opening Δw and the absolute value of velocity $|v_{y_{y=\delta}}|$ was considered with the following association matrix of Pearson correlation coefficients.

Table 3.2: Input parameters with the corresponding uncertainty ranges

Input parameter		Uncertainty range		Distribution type	Distribution parameters
		Lower boundary	Upper boundary		
d_p	[mm]	0.9	6	normal	$\mu = 3$, $\sigma = 0.6$
$-v_{y_{y=\delta}}$	[m·s^{-1}]	0.005	0.5	uniform	$min = 0.005$, $max = 0.5$
Δw	[$\times \Delta x$]	3	10	normal	$\mu = 6$, $\sigma = 3$
β_s	[°]	25	38	uniform	$min = 25$, $max = 38$
$\Delta\beta = \beta_m - \beta_s$	[°]	3	10	uniform	$min = 3$, $max = 10$

$$\begin{array}{cc} & \begin{pmatrix} d_p & -v_{y_{y=\delta}} & \Delta w & \beta_s & \Delta\beta \end{pmatrix}^T \\ \begin{pmatrix} d_p \\ -v_{y_{y=\delta}} \\ \Delta w \\ \beta_s \\ \Delta\beta \end{pmatrix} & \begin{bmatrix} 1 & 0 & 0 & 0 & 0 \\ 0 & 1 & 0.7 & 0 & 0 \\ 0 & 0.7 & 1 & 0 & 0 \\ 0 & 0 & 0 & 1 & 0 \\ 0 & 0 & 0 & 0 & 1 \end{bmatrix} \end{array}$$

The sample generation was conducted with the program SUSA (Software for Uncertainty and Sensitivity Analyses) of the GRS (Gesellschaft fuer Anlagen- und Reaktorsicherheit). In total, 200 sets of stochastic combinations of these parameters are randomly generated. For practical reasons, the calculations are limited to simulate debris bed formation for 300 s in the spatial interval $x \in [0, 4.5]$. This time period was considered sufficient to obtain representative results in most cases. Figure 3.15 shows the generated distributions of the input parameters in the form of histograms of random samples and the underlying cumulative probability distributions. A scatter plot showing the dependency between the Δw and the absolute value of velocity $|v_{y_{y=\delta}}|$ is presented in Figure 3.16.

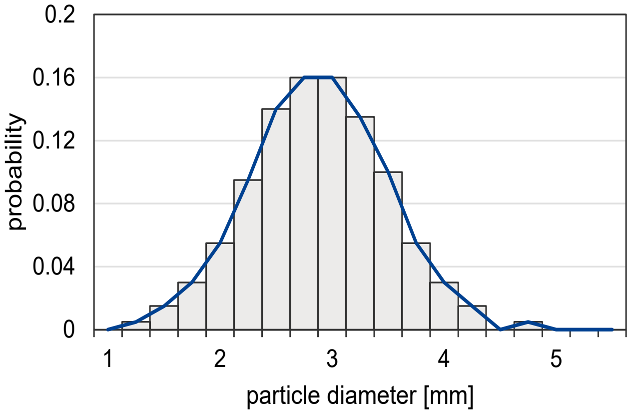

Figure 3.15: Input distribution

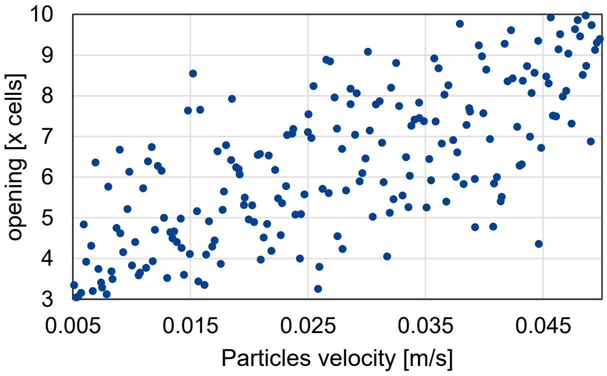

Figure 3.16: Scatter plot of the generated random values of Δw and $|v_{y_{y=\delta}}|$

3.5.2 Results of uncertainty and sensitivity analysis and ranking of input parameters

One scalar (not time- or index-dependent) and integral output variable is chosen to be evaluated statistically in this uncertainty study, which is the maximum bed height h_{300} after 300 s. Figure 3.17 shows the empirical cumulative distribution function for the maximum bed height h_{300} obtained with a statistical evaluation of all the simulation results. It is evident that the function is normally distributed with the mean $\mu = 1.514$ m. The uncertainty analysis gives that 95% of values are within 2 standard deviations ($\sigma = 0.554$ m) of the mean. It yields that 95% of the results are between 0.4068 m and 2.6228 m. The highest formed bed is 2.6534 m high, and the lowest height is 0.47461 m. In more than 70% of the computational cases the formed beds are higher than 1.837 m. These results could be highly significant for the simulation of the debris beds coolability.

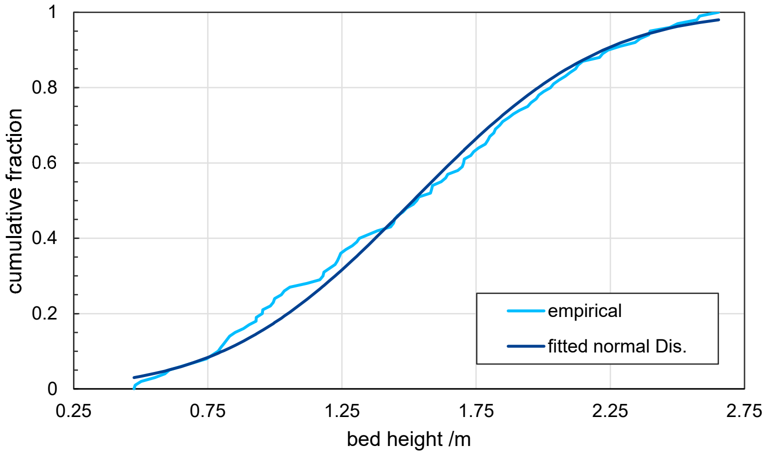

Figure 3.17: Empirical distribution function of the output variable h_{300}

In addition to the distribution of the simulation results, it is also important to investigate how the output parameter depends on the inputs and to get a ranking of these uncertain parameters with respect to their contributions to the uncertainty of the output variable. In the context of this statistical evaluation, different groups of correlation coefficients can be calculated to characterize the linear and non-linear dependencies and measure the sensitivity. In this work, the following correlation coefficients are used for the evaluation:

- **Pearson's ordinary correlation** (also called Bravais-Pearson correlation [91]): is a dimensionless measure of the degree of linear correlation between two variables, which can take values between -1 and 1, where the value 1 (or -1) corresponds to a total positive (or negative respectively) linear correlation. A value of 0 implies that there is no linear correlation between the two variables. However, the two variables may still be depending on each other in a non-linear way. Thus, the Pearson coefficient is not always an ideal measure of the stochastic dependence.

- **Blomqvist's medial correlation**: for two random variables X and Y with the medians μ_X and μ_Y respectively, the population version of the medial correlation coefficient (also known as Blomqvist's β_v) is given by the following Probabilities $\mathbb{P}$ difference [14]:

$$\beta_v = \mathbb{P}\left[(X-\mu_X)(Y-\mu_Y)>0\right] - \mathbb{P}\left[(X-\mu_X)(Y-\mu_Y)<0\right] \tag{3.65}$$

- **Spearman's rank correlation** (named after Charles Spearman [123] and commonly referred to as ρ-rank): is a non-parametric[2] measure of statistical monotonic

---

[2] non-parametric test ≡ distribution-free test: this means that it does not depend upon the assumptions of the underlying distributions (for example, it will not be assumed that the data came from a normal distribution). In parametric tests, assumptions will be made about a population's parameters (e.g, the mean or standard deviation).

dependency between the rankings of two variables X and Y (rank correlation). It measures how well any monotone function can describe the relationship between two variables without making any assumptions about the probability distribution of each variable. It is equivalent to the Pearson correlation between the rank values Rg_X and Rg_Y of those two variables:

$$\rho_S = \frac{\mathrm{Cov}(Rg_X, Rg_Y)}{\sigma_{Rg_X}\sigma_{Rg_Y}} \tag{3.66}$$

The operator Cov denotes the covariance and σ the standard deviation. If Y is increasing for an increasing X, the Spearman coefficient is positive and it becomes negative for a decreasing Y. When X and Y are perfectly monotonically related, ρ_{Rg_X,Rg_Y} becomes 1 and it is equal to 0 when there is no clear tendency for Y to increase or decrease for increasing X. Unlike Pearson's correlation, it does not need the assumption that the relationship between the variables is linear.Therefore, the Spearman's rank correlation has the advantage of being less sensitive than the Pearson correlation to strong outliers due to the fact the its coefficient ρ_S limits the outlier to the value of its rank.

- **Kendall's rank correlation** (named after Maurice Kendall and called also Kendall's τ [59]): similar to Spearman's ρ-rank correlation coefficient, the non-parametric Kendall's τ asses the statistical association between random variables based on the ranks of the data. For a set of (unique) observations $\{(x_1, y_1), (x_2, y_2), ..., (x_n, y_n)\}$ of the random variables X and Y, the Kendall correlation coefficient τ_K is defined as:

  $$\tau_K = \frac{\text{(number of concordant pairs)} - \text{(number of discordant pairs)}}{n(n-1)/2} \tag{3.67}$$

  Where a pair of observations (x_i, y_i) and (x_j, y_j) are called concordant for different i and j, when the ranks for both elements agree (i.e., when both $x_i > x_j$ and $y_i > y_j$, or both $x_i < x_j$ and $y_i < y_j$). Otherwise, they are said to be discordant. For equal sets, it is neither discordant nor concordant. In most of the situations, the Kendall's τ-correlation has usually smaller values than Spearman's ρ-correlation [126].

Figure 3.18 shows the correlation coefficients computed from the 200 calculation sets between the output variable (the max. bed height h_{300}) and the influencing input parameters listed in Table 3.2. The scalar sensitivity analysis shows that the bed height is "mainly" determined and influenced by the velocity $v_{y_{y=\delta}}$ and the opening Δw. As expected, the bed will become higher for increasing values of those both inputs (i.e higher beds for increasing mass flow rates of the solidified particles). Less decisive is the angle of settlement β_s. It is observed that the bed becomes flatter for higher difference between both characteristic angles $\Delta\beta = \beta_m - \beta_s$. Compared to other variables, it can also be concluded that the particles diameter does not have a significant influence on the bed

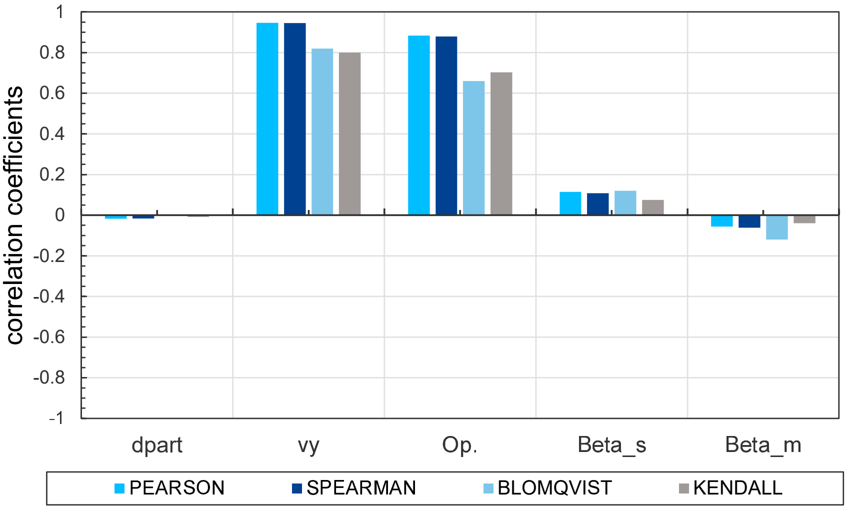

Figure 3.18: Scalar sensitivity analysis for the max. bed height ($R_p^2 = 0.9906$, $\rho_S^2 = 0.987$)

height (however, both the particles diameter and the porosity are crucial for the coolability).

In SA, graphical techniques are useful tools to interpret the results provided by the numerical sensitivity study. Scatter plots are among the most used graphical tools to analyze relations between each input parameter and the model output and detect some trends in their functional relation. However, they can not capture some interaction effects between the different inputs. Whereas on the other hand, cobweb plots, also called parallel coordinate plots, allow to visualize all the combinations of the input variables which lead to a specific range of model outputs and provide a better understanding of the sensitivity results. Figure 3.19 draws such a graph. Vertical parallel lines separated by equal distances are used to represent the sampled values of a given number of inputs/-outputs. Each vertical line is used for a different input/output, and either the raw values or the ranks may be represented (the ranks are considered in the present case). Sampled values/ranks are marked in each vertical line, and jagged lines connect the values corresponding to the same simulation run (in Figure 3.19, the mark on the first axis corresponds to the output variable). For the sensitivity interpretation, it is interesting to select, among those lines, the ones which correspond to a specific range of the output variable.

In Figure 3.19, the simulations leading to the 10% lowest values of the model output h_{300} have been highlighted (i.e., the simulation runs with the 20 lowest results of bed height). This allows to immediately understand that the lowest beds are obtained with the lowest values $v_{y_{y=\delta}}$ and Δw and they are corresponding to different particles diameters and angles of repose scattered over the whole uncertainty ranges.

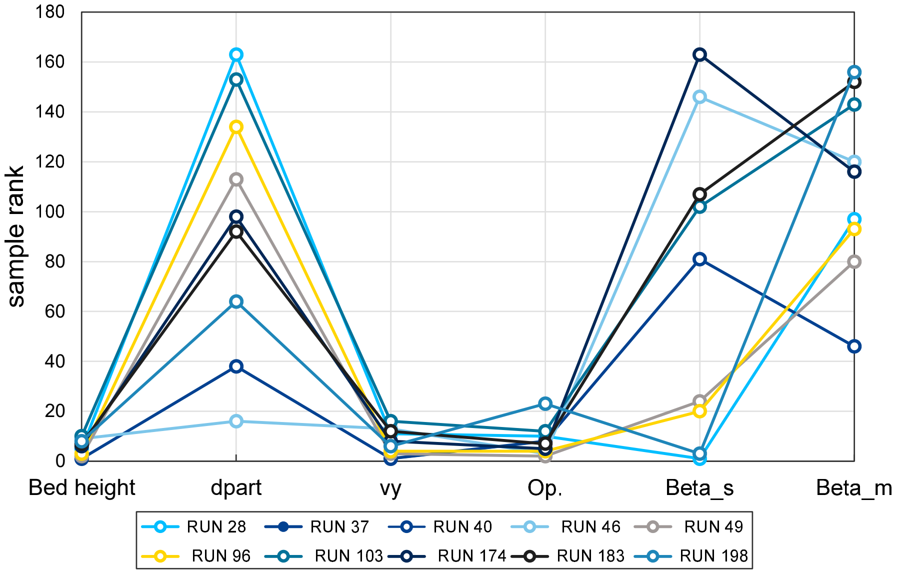

Figure 3.19: Cobweb plot of ranks for lowest 20 results of bed height

4

Model Validation and Experimental Investigation

In the context of developing an accurate and credible simulation code, it is a major concern whether the presented model and its results are "correct." This concern is addressed through model verification and validation (V&V). Model verification consists of ensuring that the computer programming and implementation are an accurate representation of the developer's conceptual description and specifications (see Section 3.3). Model validation is often defined as "*the process of determining the degree to which a model [and its associated data] is an accurate representation of the real world from the perspective of the intended uses of the model*" [AIAA G-077-1998]. In other words, validation assessment focuses on the systematic comparison of simulations results and their associated uncertainties with experimental data (with their respective uncertainties). Therefore, the test facility "BeForE" has been newly designed and built at the Institute of Nuclear Technology and Energy Systems (IKE) within the framework of this thesis aiming at delivering the needed experimental data for the validation process.

4.1 Test facility "BeForE"

The primary goal of the BeForE-facility (**Be**d **For**mation **E**xperiment) is to study visually phenomena of particles deposition and relocation forming debris bed with the water presence and an upward-flowing gas. The whole set-up of the experimental facility is depicted in Figure 4.1. The apparatus consists of three major parts: (i) the viewing bin, (ii) the particles pouring system, and (iii) the compressed air injection system.

To facilitate the optical observation and quantitative measurement, **the viewing bin** is a quasi-two-dimensional (2D) transparent vessel made with two vertical Plexiglas walls

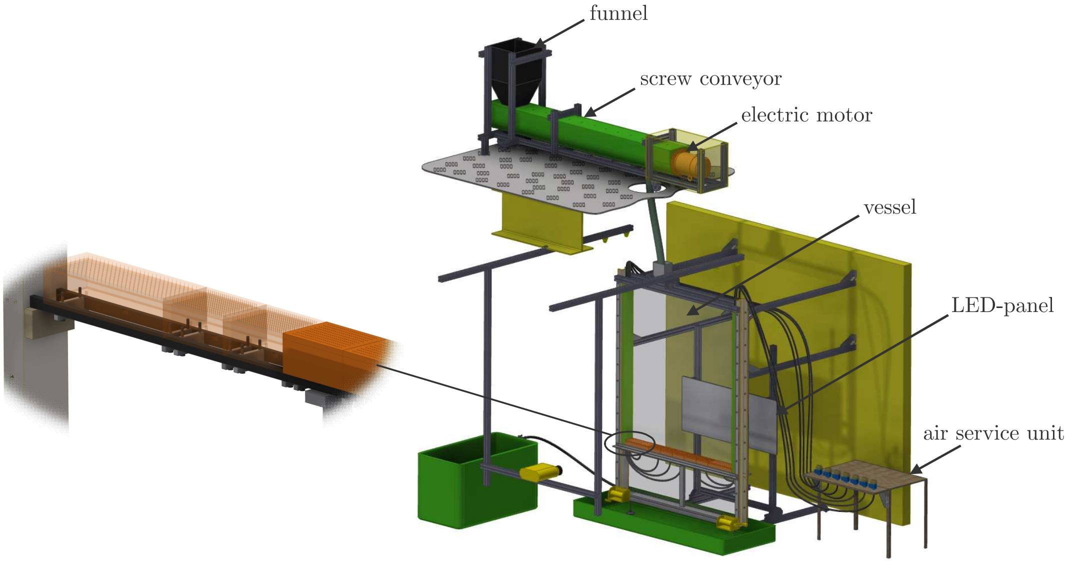

(a) (b)

Figure 4.1: CAD-model of the BeForE-facility: (a) air injection chamber; (b) the main apparatus

separated by a gap $T = 100$ mm. The adoption of a bin with a gap thickness of 100 mm achieves a good balance between experimental operation, physical requirements (avoiding wall effect on falling particles), and the reliability of experimental results within 2D-conditions. The transparent walls are 1950 mm in height and 1450 mm in width. As illustrated in Figure 4.2, the two Plexiglas plates and the sealing tape are held on both sides of the container with steel U-Channels and clamped by a flat steel frame (support pad). Due to the permanent exposure to water, all the steel parts in the facility are varnished with a special paint designed for naval applications.

The particles pouring system consists of a feed hopper and a motor-driven screw conveyor, serving as variable rate feeder. It is placed at the top of the viewing bin on a separate structural base at the height of 3200 mm to isolate the vessel from the vibrations resulting from the motor. The walls of the hopper are steep enough, and its geometry is properly designed to avoid the *no-flow problem* during the discharging. This problem can result either from bridging or from ratholing:

- **Bridging** (arching) occurs when an obstruction in the shape of an arch forms over the outlet and blocks the flow. It can be an interlocking bridge, when large particles mechanically interlock forming an obstruction, or a cohesive bridge, in the case of wet particles.

- **Ratholing** occurs when particles flow takes place only in a channel located above the hopper outlet. As a result of cohesive forces, the stagnant material outside the

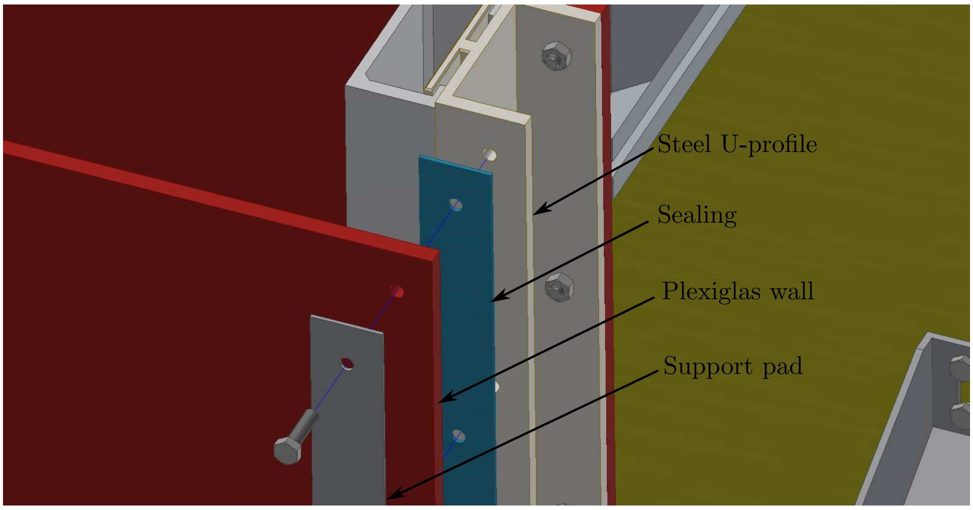

Figure 4.2: CAD-model of the main vessel assembly

channel will not flow into it, forming a stable rathole.

To avoid the potential dispersion of particles during their falling, the granular mass is discharged into the bin through a flexible release pipe with variable diameter. In order to adjust the position of the falling particles, the pipe can also be horizontally displaced on the upper side of the bin.

The conceived facility aims not only at investigating bed formation characteristics and validating the numerical model, but it also studies the bed formation under the influence of time-dependent natural convection of steam bubbles as illustrated in Chapter 5. In the BeForE-facility, purified compressed air is used as a simulant of steam generated from the flooded corium particles in the real case. As shown in Figure 4.1(a), **the compressed air injection system** is made up of 7 separated Plexiglas air chambers, which are perforated on the upper side (0.5 mm diameter holes), proportional valves and a separate control circuit for controlling the entire air flow. At the height h = 450 mm inside the transparent vessel, the air chambers are placed to hold the falling particles and to control locally the time-dependent air injection into the bed. Depending on the granulate mass on the top of each chamber, air flow rate is monitored and adjusted singly by motor-driven control valves (Buerkert Type 3280). In order to have similar conditions for both gases, the steam and air flow should have equivalent Blake- and Euler-Numbers (air flow rate distribution and characteristics will be discussed in details in Chapter 5). The air supply network provides a maximum flow of 460 l·min^{-1} at a maximum pressure of 5 to 6 bar. On each air leg, a manometer and a rotameter are deployed as additional monitoring instruments of the air pressure and flow rate.

4.2 Preliminary measurements and experimental condition

To simulate the fuel debris, 4 kinds of particles with different sizes and shapes were used. A series of experiments were conducted using gravel and aluminum particles, the properties of which are listed in Table 4.1. In order to have a reliable validation, the main physical properties of particles influencing the developed model are measured and determined in the following subsections.

Table 4.1: Physical properties of particles

	aluminum	sand	fine gravel	coarse gravel
Particles morphology	irregular	edge rounded		
Bulk density [g/cm^3]	2.33	2.54		
Size distribution [mm]	2.0 - 4.0	1.0 - 2.0	2.0 - 3.15	5.6 - 8.0
Equivalent diameter [mm]	3.75	1.45	2.13	6.48
Static angle of repose [°]	40	30	32	35
Porosity [%]	35.3	38.3	40	39.3

4.2.1 Porosity

Porosity ε describes the measure of void spaces in a representative control volume. It is defined as the ratio of the hollow volume V_{void} to the total volume V_{total}:

$$\varepsilon = \frac{V_{void}}{V_{total}} \tag{4.1}$$

The bed porosity can be determined indirectly by the measurement of auxiliary variables in two different ways:

- calculate the mass of water needed to fill the void volume in a particle bed:

$$\varepsilon = \frac{V_{water}}{V_{total}} = \frac{m_{water}}{\rho_{water} V_{total}} \tag{4.2}$$

- with the help of the density ρ_p and the total mass of particles m_p:

$$\varepsilon = 1 - \frac{V_p}{V_{total}} = 1 - \frac{m_p}{\rho_p V_{total}} \tag{4.3}$$

Due to the lesser uncertainties in the first method, it is privileged to use it for the measurement of the mean porosity of each sample bed (see Section 4.5.1). Notice, that the porosity is influenced by the particles shape and size distribution. The more irregular and

bigger the particles are, the larger the holes are, and thus the porosity is higher. On the other hand, a polydispersed mixing with different particles mixing has a smaller porosity. This reduction of porosity can be explained by the fact, that the smaller particles will fill the void regions between the bigger ones. This can explain the measurements in the case of coarse gravel mixing, which has a relatively larger size distribution than the others.
In real debris bed, the coolability depends strongly on the bed porosity (see Section 1.3). The bed is better coolable with higher porosity. Bigger void regions yield more coolant presence inside the bed, and thus more heat can be removed through water evaporation. On the other hand, the vapor can escape consequently easier from the bed, due to the decreasing friction and pressure losses.

4.2.2 Equivalent diameter

In the case of beds of irregularly shaped particles or polydispersed ones, it is appropriate to define an equivalent diameter. It can be determined according to the Ergun's law.
As fluid flows through a porous media packed with stationary particles, it experiences a pressure loss due to friction. The prediction of these frictional pressure drops can be calculated with the use of the Ergun equation [36]:

$$-\frac{\Delta p}{H} = 150\frac{(1-\varepsilon)^2\mu}{d_p^2\varepsilon^3}U + 1.75\frac{(1-\varepsilon)\rho}{d_p\varepsilon^3}U^2 \tag{4.4}$$

where Δp represents the pressure drop over the height H of the bed. The first term on the right side of Equation (4.4) corresponds to the viscous loss ($\backsim$ superficial velocity U), and the second term is the inertial loss ($\backsim U^2$). Although the Ergun equation was initially derived for mono-sized spherical particles, the flow resistance in the packed bed composed of non-spherical and irregularly shaped particles can be predicted by the Ergun equation, by taking d_p as an equivalent particle diameter. The applicability of the Ergun's law to polydispersed beds was beheld and proven in the works of Leininger [69], Li et al. [73] and Clavier et al. [29]. They have also demonstrated, that the equivalent diameter can be taken as the product of Sauter mean diameter[1] and a shape factor (also called sphericity[2]).
To find this equivalent diameter, an experimental study was carried out in a separate small facility (Debris air-water experiment) to determine the frictional pressure drops of fluid flows in porous beds packed with the sample particles. Figure 4.3 illustrates the test section, which is water/air single and two-phase flow loop for porous media. It consists of a transparent Polycarbonate tube (L = 600 mm, D_i = 100 mm), in which the particles are located. The fluid (air and/or water) is supplied from the bottom and

---

[1] Sauter diameter is defined as the diameter of a sphere that has the same [volume/(surface area)] ratio as the particle of interest.

[2] Sphericity is defined as the ratio of the surface area of the equivalent-volume sphere to that of the actual particle.

flows upwards through the porous bed. The facility has four pressure measuring points, and the pressure differences are measured between different heights ($\Delta h_1 = 100$ mm and $\Delta h_2 = 300$ mm) with two piezoresistive differential pressure transmitters (Keller Type PD-23/8666: measuring range 10 kPa - accuracy class 0.1). In the present study, air is chosen as the working fluid, and the air flow is adjusted with two hot-wire anemometers. Furthermore, a thermocouple (type N Nicrosil-Nisil) is located in the sample bed to determine the relevant temperature-dependent physical properties (viscosity and density) of the fluid. In addition to the calibration of instrumentation, the measurement and the data acquisition systems are qualified by preliminary tests of single-phase flow through beds packed with monodispersed particles with a well-known form and diameter. Then, the validity of the small facility and the accuracy of its instruments could be confirmed by the excellent agreement of the pressure drops in these tests with the Ergun equation [36].

In the present experiment, the particles are sieved in advance with different sieves, to have the desired size distribution. Then, they are uniformly loaded in the test tube. To establish steady-state conditions and to make sure that the fluid has access to all the pores, the measurement of the pressure starts first 15 minutes after the air inflow. Data are recorded with the acquisition system, and the procedure is repeated for other flow rates (e.g., superficial velocities). Figure 4.4 illustrates the variation of the experimental frictional pressure gradient with respect to the superficial velocity (plotted with various discrete markers). The values can be perfectly approximated with a parabolic distribution $\Delta p = C_1(d_{eq})U^2 + C_2(d_{eq})U$ similar to the Ergun equation (4.4). The dashed lines in Figure 4.4 represent the corresponding polynomial approximations for the different particle types. The equivalent diameter d_{eq} of each bed is then deduced from the constants C_1 and C_2 and summarized above in Table 4.1.

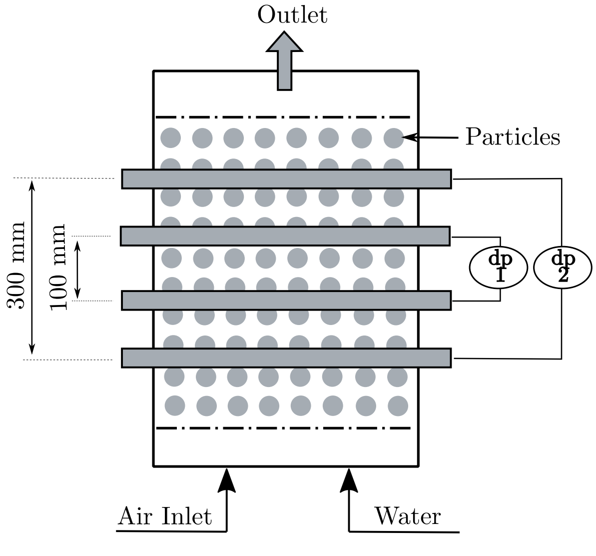

Figure 4.3: Schematic diagram of the Debris air/water experiment

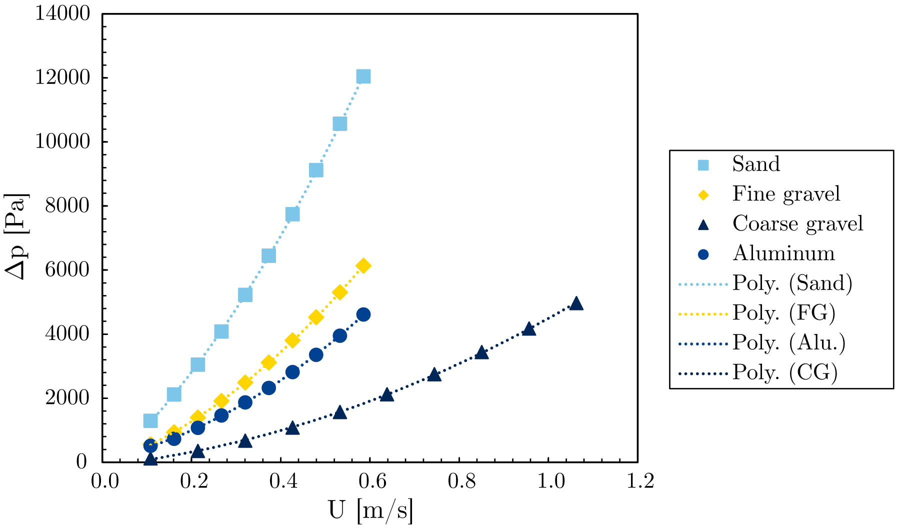

Figure 4.4: Pressure loss in different porous beds (air, $\Delta h_1 = 100$ mm)

4.2.3 Angle of repose

The angle of repose is determined experimentally with another small dedicated facility, shown in Figure 4.5. The tests were performed in dry and wet conditions (i.e., with water presence) several times on the trot, in order to reduce the measurements uncertainties.

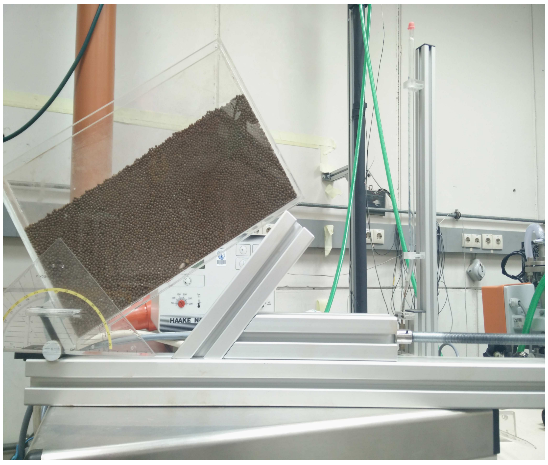

Figure 4.5: Photo of the small facility for the measurement of the angle of repose

4.2.4 Experimental procedure

The experimental procedure in BeForE was conducted as follows. In the beginning, a specific mass of particles is sieved and measured, and its physical properties (as mentioned in the previous subsections) are determined. Then, the particles are packed in the funnel. Second, the pouring rate is adjusted with the screw feeder, and the particles are poured into the vessel, where the water level is held at the constant level 1850 mm. The conducted experiments can be classified into two different test series. In the first series, the primary concern is only the validation of the bed formation without the boiling effect and the presence of air flow during or after the bed formation. In the second test series, the effect of boiling on the debris bed will be studied in Chapter 5. So, in the latter case, compressed air was injected from the bottom of the bed. The air flow rate was monitored and measured by a dedicated data acquisition system (see Chapter 5 for more details). In all the test series, the whole experimental process is recorded with a digital video camera aiming at determining the bed geometry visually.

4.3 Images acquisition and processing

As already mentioned in the description of the test set-up, one of the most significant features of the BeForE-facility is the visual access that allows for non-intrusive video recording of bed formation process. To determine the bed geometry and its progress in time, a high-resolution CCD camera (Prosilica GX1050C) is employed. It is able of recording tens of frames per second at full resolution. The formed bed needs to be detectable to a degree where it can be clearly distinguished from the background. In order to have a good optical arrangement with good contrast and high-quality record, a LED panel with the dimensions 1200×450 mm^2 and 1000 lux lightening intensity is mounted at the back of the vessel. Upon recording, each image needs to be analyzed using image processing techniques as described in Figure 4.6. After reducing the noise in each image with a median filter, the first step is to separate the formed bed and the moving particles from the static background. Second, the resulting images have to be converted into binary images using locally adaptive thresholding. Thresholding algorithm converts the input grayscale image to a binary image by setting all pixels whose luminance values are above a threshold to a foreground value (= 1 white) and all the remaining pixels to a background value (0 black). Unlike the conventional global thresholding, the local adaptive method changes its threshold dynamically over the image, by computing the local mean intensity around each pixel[3]. This technique takes into account the spatial variations in illumination. Hence, it is the most appropriate for our image binarization because of the considerable background noise and variation in contrast and illumination existing in the present case, there exist many pixels, which cannot be easily classified as foreground or background.

---

[3] This technique is also called Bradley's method [16].

Then, the contrast is artificially increased. Afterwards, a filling-operator (as defined in -Morphological Image Analysis-) is performed on the binary images to remove the isolated pixels and to fill the small holes (local minima) in the connected white forms. In the next step (Figure 4.6(c)), small foreground objects are extracted from the binary images by setting the limit of having a surface area bigger than few particles diameter. From the remaining objects, the image processing program has to detect the area with the biggest surface area (biggest blob operator counts the number of pixels in each blob), that should represent the formed particles bed (Figure 4.6(d)). In the last step, the exterior boundaries are traced, and the dimensions of the bed (width and length in every section) are saved in order to compare it with the numerical results.

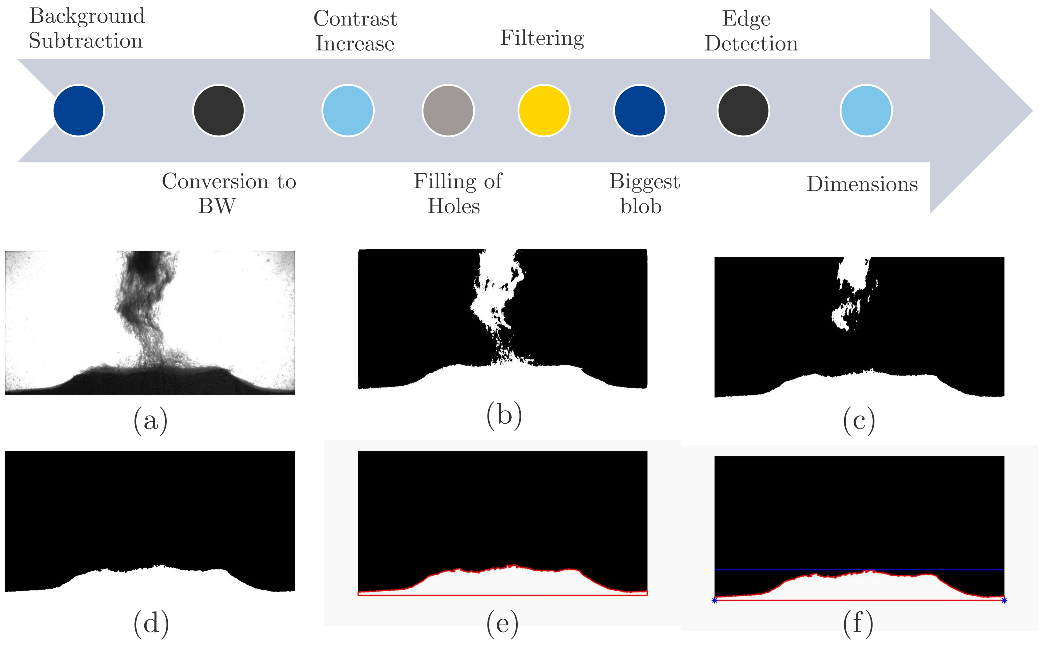

(a) (b) (c)

(d) (e) (f)

Figure 4.6: The image processing techniques

4.4 Test reliability and repeatability

The principle of reliability is a fundamental cornerstone of the experimental validation. The idea behind the test reliability is that any significant results must be more than a one-off finding and be inherently repeatable under the same conditions. A replication study is a way of ensuring that the measuring instruments are giving the same results every time and that we are conducting a reliable and valid experimental methodology and interpretation.

Repeatability is then defined as the closeness of agreement between independent and successive experimental results obtained with the same method on identical test cases, under the same conditions (same objectives, same apparatus, same operator, same instrumentation, same boundary and laboratory conditions, and after short intervals of time). It can be measured with the *repeatability standard deviation* σ_{RSD}, which may quantify the amount of dispersion within the obtained results of the same test case under the above-mentioned repeatability conditions.

In some contexts, repeatability may be defined as the value below which the absolute difference between two single test results obtained under the above conditions may be expected to lie with a specified probability.

Repeatability tests were carried out for all the tests in this work. At least 4 tests for each condition were carried out for the bed formation test series, and at least 3 repetitions for each test in the self-leveling series (see Chapter 5). For the bed formation experiment, the standard deviation σ_{RSD} of the mounds heights is between 4.2% for the aluminum beds and 8.9% for the coarse gravel. This dispersion can be mainly attributed to the random uncertainties caused by the screw conveyor in the particles pouring system, in which some particles can be in some cases blocked leading to a non-systematic uncertainty in the mass of the poured particles. Comparing the mounds total shape of the repetitive tests, a higher standard deviation can be found ($\sigma_{RSD} \simeq 14.6\%$) due to the randomness in the particles morphology and hence in the inter-particle friction explaining the fact of having a varying angle of repose along the slope surface of the bed.

4.5 Evaluation of measurement uncertainties

An experiment designed to estimate the numerical value of a physical variable will always be affected by errors or uncertainties due to instrumentation, methodology, or presence of confounding effects. Hence, the experimental uncertainty analysis deals with estimating the uncertainty in measurement in order to assess the confidence in the results.

In the present study, these measurement uncertainties were present during the preliminary measurements of the porosity and the equivalent diameter, due to the uncertainties in the instruments and also during the image processing of the results.

4.5.1 Uncertainties in the preliminary measurements

Let's consider in general the test quantity X_i whose value is estimated from n independent observations $X_{i,k}$ of X_i obtained under the same repeatability conditions. The best estimate of this test quantity $\overline{X_i}$ is obtained as the arithmetic sample means of the individual observations as:

$$\overline{X_i} = \frac{1}{n}\sum_{k=1}^{n} X_{i,k} \tag{4.5}$$

The experimental variance of the individual observations $X_{i,k}$, which estimates the variance σ^2 of the probability distribution of X_i, is given by:

$$\sigma^2 = \frac{1}{n-1} \sum_{k=1}^{n} \left(X_{i,k} - \overline{X}_i\right)^2 \tag{4.6}$$

The objective is to calculate how far the estimated means $\overline{X_i}$ is likely to be from the true means of the observations sample. This difference is given by:

$$\sigma_{\overline{X}_i} = \frac{\sigma}{\sqrt{n}} = \sqrt{\frac{1}{n(n-1)} \sum_{k=1}^{n} \left(X_{i,k} - \overline{X}_i\right)^2} \tag{4.7}$$

and it is termed as *the experimental standard deviation of the means*, and it may be used as the uncertainty measure for the present observations series, i.e., the result for a given physical measurand X_i after completing a replication series takes the form:

$$X_i = \overline{X}_i \pm \sigma_{\overline{X}_i} \tag{4.8}$$

Note that in the case of small sample sizes (i.e., if the number of the measured values is low $n < 30$), the standard deviation of the mean value must be then scaled with a correction factor t, obtained from the so-called *Student's t-distribution.* The reason behind is that the assumption of having normally distributed values, which is underlying the calculation of the standard deviation, may not be always fulfilled for low populations of random variables.

In the case, where the measurand Y is not measured directly, but it is determined from L other *uncertain* observations quantities X_1, X_2,..., X_L through the following functional relationship:

$$Y = f\left(X_1, X_2, ..., X_L\right) \tag{4.9}$$

In that case, the uncertainties in the input variables of f propagate to the uncertainty of Y and the Gaussian uncertainty propagation can be applied according to the following formula to determine the combined standard uncertainty of the Y:

$$\sigma_Y = \sqrt{\sum_{i=1}^{L} \left(\frac{\partial f\left(X_1, X_2, ..., X_L\right)}{\partial X_i}\right)^2 \cdot \sigma_{X_i}^2} \tag{4.10}$$

In this study, the particles were weighed with an electronic scale (Kern DS $30K0.5$) with a measuring uncertainty of ±0.5 g. In addition to the uncertainty in the measuring beaker, this mass uncertainty could propagate to the measurement of the porosity, as explained in Section 4.2.1. In fact, the porosity can be calculated with two different methods (The first one P_1 is defined in Equation (4.2) and the second method P_2 is explained in Equation (4.3)). Table 4.2 lists the average and the standard deviations for the repeated porosity measurements with both approaches. It confirms that lesser uncertainties can be achieved in the first method due to the elimination of the scale errors.

Table 4.2: Results of repeatability tests of porosity measurements

Particles	Method P_1		Method P_2	
	Average	confidence limit	Average	confidence limit
Sand	38.3%	±1.1%	36.2%	±2.2%
Fine gravel	40.0%	±1.0%	37.0%	±2.0%
Coarse gravel	39.3%	±1.0%	35.9%	±2.1%
Aluminum	35.3%	±1.0%	34.6%	±2.0%

For the uncertainty analysis of the equivalent diameter (as defined in Section 4.2.2), different input variables uncertainties are contributing to its evaluation, including: the uncertainty of the pressure transmitters, the uncertainty in the temperature-dependent physical properties due to the instrument uncertainty of the thermocouple, errors in the mass flow rate control, and also the bed porosity. The results of the experimental uncertainty analysis for the equivalent diameter are summarized in Figure 4.7, where the dark blue markings correspond to the mean particles, the light blue boxes to the size distribution after sieving, and the black intervals represent the calculated confidence limits for each particles sample.

Note also that the uncertainty of the mass flow controller for the total air supply in the self-leveling experiments is less than 3 L/min, and that of the rotameters for controlling the air flow rate of each air chamber was maximum 1 L/min.

4.5.2 Uncertainties in the image processing

The main error source in the experimental procedure is the uncertainty during the image processing. Due to the low contrast between the formed bed and the falling particles, the binarization of the frames will lead in some cases to an inaccurate tracing of the bed boundaries and to outliers in the height curve. Since the compactest particles mass is usually falling in the middle of the vessel, the most considerable deviations can be mostly seen over the middle block. For the correction of this deficiency in the processing tool, fitting and filtering functions were implemented in the MATLAB script during the real-time processing of the frames (i.e., at the same time with the image acquisition) and also for the post-processing of the results. For example, the heights values, which are higher than 110% of the maximal bed height at the end of the test will be filtered. In order to detect the outliers in the first few seconds of the experiment, further criteria need to be set. In the range between 0 and 5 seconds, all height values beyond the constant O_1 are

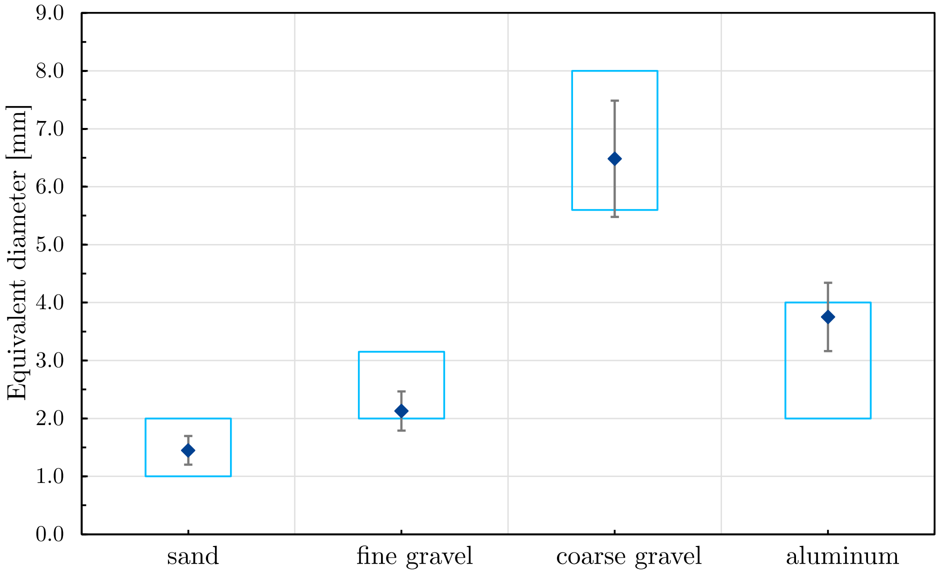

Figure 4.7: Equivalent diameter of the different particles and the corresponding uncertainties

removed and in the range of 5 to 10 seconds all values bigger than a higher constant O_2 are filtered. The constants O_1 and O_2 are listed for the various particles[4] in Table 4.3. These constants were determined and validated from previous repetitions.

Table 4.3: Filtering limits of the outliers in the image processing

Time $[s]$	Filtering limits	aluminum	fine gravel	coarse gravel
$[0, 5]$	O_1	8 cm	12 cm	8 cm
$[5, 10]$	O_2	12 cm	16 cm	12 cm
> 10		$h < 1.1 \cdot h_{end}$		

One further criterion to ensure accurate filtering of the outliers is the control of the gradient between every successive measuring points. Height values with gradients exceeding 5 cm/s or below -10 cm/s exceed the criterion limited by the maximum possible mass flow, and they are therefore not taken into account.

---

[4] No correction was needed for sand, since no strong deviations occur due to the small size of the particles.

4.6 Experimental results of bed formation without air injection and model validation

4.6.1 Test results interpretation and discussion

In order to gain first insights into the bed formation process, a series of experimental runs are initiated, by discharging the same amount (20 liters) of particles with various sizes (coarse gravel: $5.6 - 8$ mm/ aluminum: $2 - 4$ mm/ fine gravel: $2 - 3.15$ mm /sand: $1 - 2$ mm) and shapes (rounded edges and irregular shaped) into the two-dimensional water vessel. Figure 4.8 depicts the effect of particle diameter [(a)-(c)] and the shape [(b) and (d)] on the bed formation process and the motion of the particles in the water.

Based on the quantitative observations of the recorded runs, characteristics of the bed formations behavior were analyzed and compared to all the runs. It is found, that due to the various interactions between solid particles and the water vessel, different particles deposition and relocation regimes could be identified. Three different regimes could be recognized depending on the particles diameter and density. Depending on our observations, each regime is characterized as follows:

- **Sliding regime (inertial-dominant regime)**: this regime can be observed for gravel particles with $d_p \geq 3$ mm approximately. Due to their inertia, particles are falling down vertically in the water vessel and form a delta-shaped bed until reaching the critical angle of repose. Then the slope will remain constant, and the particles are "sliding" down the slope within a thin layer on the top of the nearly-quiescent heap, as initiated and assumed in Chapter 2. Unlike the below presented regimes, the sedimentation was not heavily influenced by the fluid convection flows inside the vessel or by the following particles jet. This regime is dominated by the particles inertia and the particle-particle interactions (friction, collision) listed in Chapter 2.

- **Convection-dominant regime**: this regime is found to exist for gravel and aluminum particles with 1.5 mm$< d_p <$ 3 mm. Forced by the continuous inflow of particles, a pool convection can occur leading to a lateral displacement of the smaller (and lighter) particles. At the early stage, the pool convection may lead to the formation of (initially) concave beds with two mounds at its top. Depending on the mass flow rate and the jet diameter (more precisely depending on the ratio d_p/W_p, with W_p being the release pipe/jet diameter), the final mound top shape may change from concave to convex. The relative smaller particles can also be pushed away by the subsequent particles flow, leading to a decreasing of the bed height.

- **Particle-suspension regime**: for sand particles, this regime could be observed for $d_p \leq 1.5$ mm. Due to their decreasing inertia, these light particles are more likely to be suspended in the water vessel. The poured particles tend to be ejected

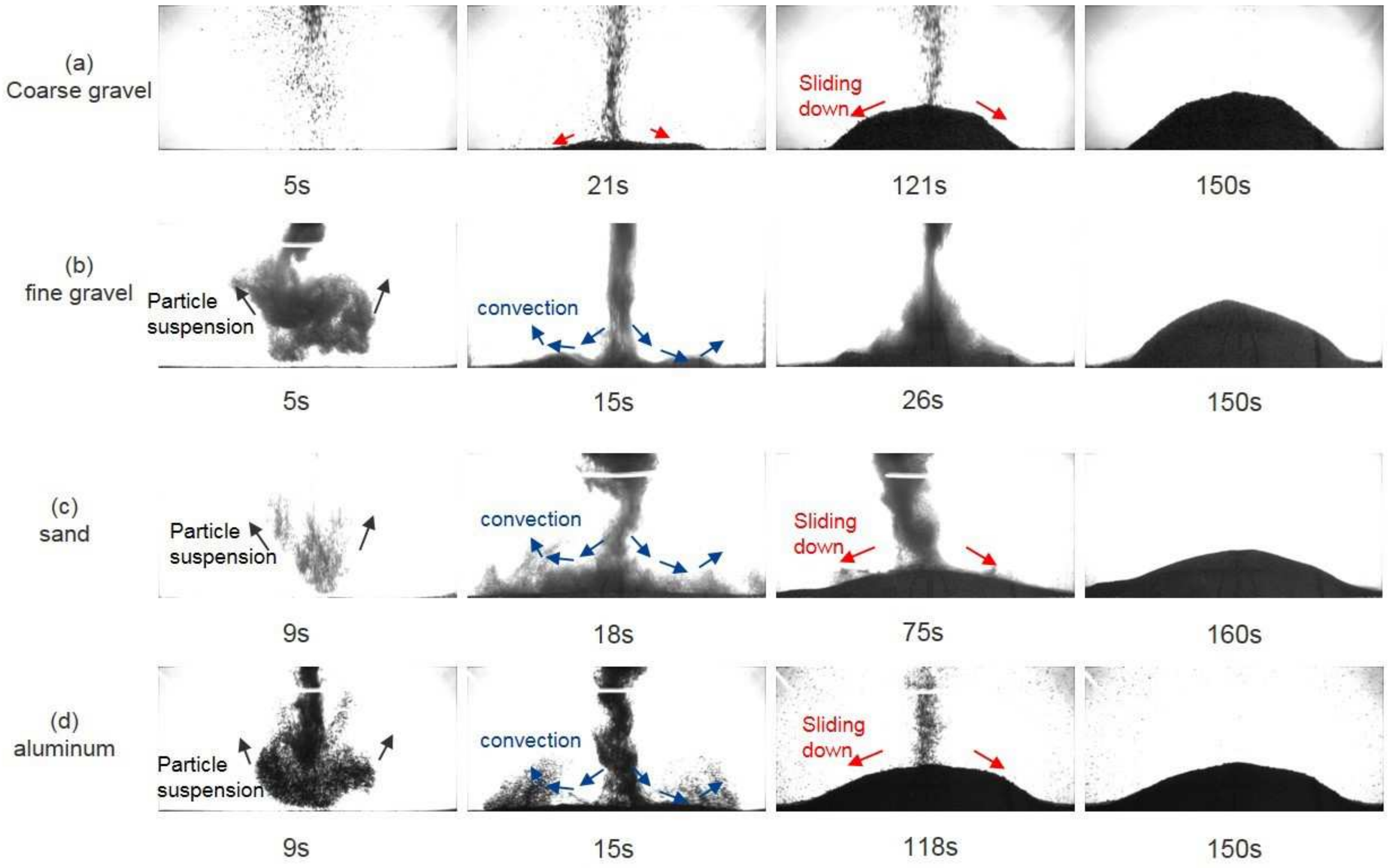

Figure 4.8: Time sequence snapshots of bed formation for several particles ($V = 20\text{L}$)

by the fluid convection inside the bed and to also be distributed (nearly in a uniform way) inside the vessel. The suspended particles will sediment gradually on the pool bottom leading to the flattering of the bed.

- Since the used samples are composed of poly-dispersed particles with different size ranges, it is possible that more than one regime can occur simultaneously during the formation process. Besides, **transitional** regions can also be seen between the different regimes, since its margins cannot be certainly and precisely determined.

In the present experimental work, the following conclusions can be drawn from the regimes identification above.

In addition to the assumption taken in Chapter 2 that the falling particles will settle around the center to slide down the slope within a thin layer on the top of a nearly quiescent bed (see the red arrows in Figure 4.8(a)), a pool convection could also be observed for smaller particles (see Figure4.8(b)-(d)). This convection is caused by the entrainment of debris into the water driving the particles laterally in the vessel. The particles are also forced by the continuous inflow of the following particles to be pushed away from the center forming two small mounds at the bottom (see Figure 4.8(b) t = 15s). This lateral relocation of the particles has a big influence on the final dimensions leading to the leveling of the bed and its extension horizontally. It could also be observed, that the smaller particles (< 1 mm) are ejected by the jet flow and suspended around the vessel due to their light weight and settle uniformly on the bottom. This small particles suspension leads to the flattering of the bed and diminution of the height.

4.6.2 Analyses of experimental parameters

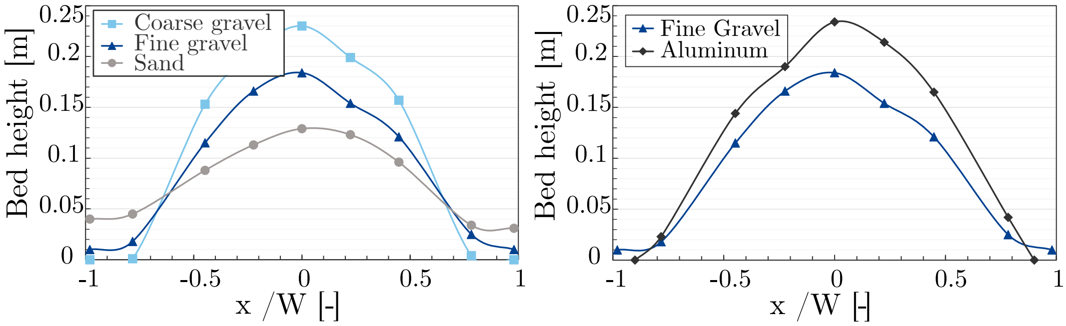

(a) Effect of particles size

(b) Effect of particle shape

Figure 4.9: The effect of particles properties on bed height profiles (20L of particles)

Figure 4.9a shows the influence of the particles size on the bed height profiles of sand/ gravel particles qualitatively. Here, the y-axis indicates the bed height, while x/W stands for the distance to the vessel centerline (normalized by half of the vessel width W). It shows that the bed becomes flatter and broader for decreasing particles sizes. As discussed in the previous section, the coarse gravel particles; due to increased inertial; become more difficult to be suspended or to be driven to the sides by the convective flow. Another finding that can be understood from Figure 4.9b is the effect of the particles shape on the bed formation. The fine gravel and alumina particles have an equivalent size range and comparable densities but different forms. It is found that for rounded-edged particles (fine gravel) the height is much less than for the aluminum bed. It can be explained by the decreasing effect of particle-particle and particle-bottom friction. Less friction drives the bed to have a smaller angle of repose and to have more particles sliding down the slope.

4.6.3 Numerical model validation

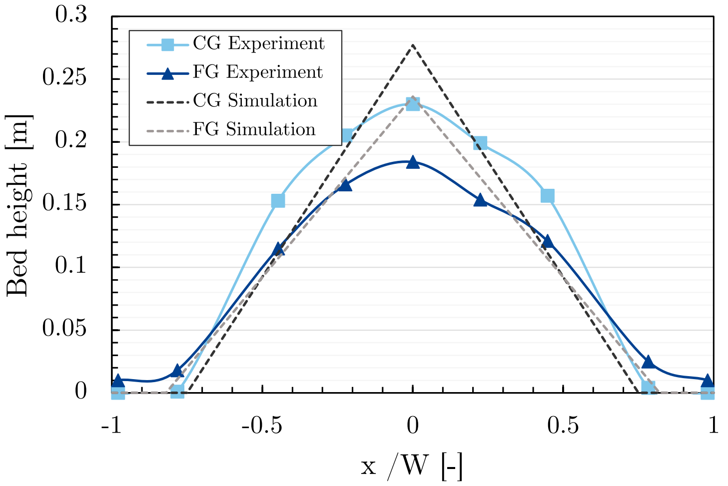

Figure 4.10: comparison of the height profiles for the coarse (CG) and the fine (FG) gravel beds between the numerical and experimental results

Figure 4.10 shows a comparison between the experimental results and the numerical simulations for the fine and coarse gravel. The model could give a good numerical prediction of the bed height (with a mean error of 17.5% for coarse gravel and 27% for fine gravel). The model is overestimating the bed height and underestimating its width. In addition to the measurement uncertainties, this deviation between the numerical model and experimental data can be explained by the fact that this continuum model is only taking into account the particles sliding and cannot simulate the convection flow or the suspension of individual particles (as illustrated in Section 4.6.1). Therefore, the numerical simulation is in better agreement with the reality for the case of the bigger particles (i.e., for $d_p \geq 3$ mm approximately → mainly for coarse gravel), which should be owing to the absence of these phenomena. Nevertheless, it can still deliver a very good prediction of the reality for smaller particles. From Figures 4.8-4.10, it could also be pointed, that, unlike in the numerical results, the angle on the mound summit is lower than the base angle. In addition to the explained phenomena, it can also be explained by the effect of the collision of the falling particles on the summit. It leads to higher deviation from the reality by the simulation of the angle of repose in this region (deviations up to 8.3% in some cases).

5

Boiling Effect on Debris Bed Formation

After studying the dynamics of the solidified melt particles and the derivation of a numerical model describing the debris bed formation from particles deposition and relocation, this chapter aims at giving the present work more breadth and broadening it by further investigating the influence of the steam production inside the hot debris bed on the particles spreading and hence on its heat removal capability.

5.1 Phenomenology and state of the art

It has been shown in Chapter 1 and many other studies [128][129] that the bed shape and height are among the most important factors determining the decay heat removal capability by natural convection of the coolant in order to stabilize the debris temperature and avoid a possible remelting and a threat to the containment integrity.
However, coolant boiling and two-phase flow caused by decay heat, serve as a source of mechanical disturbance, which might lead ultimately to leveling of the debris bed [143]. This mechanism, as illustrated in Figure 5.1, defines the term "*debris bed self-leveling.*"
Viewing the importance of this process and its influence on bed geometry and coolability, few experimental studies have been conducted on this subject, tough scanty. Gabor (1974) [40] was one of the pioneers in the field demonstrating experimentally the existence of these phenomena by volume heating a particle bed composed of UO_2-salt water. He has implied the contribution of the boiling inside the bed to its flattering and that the self-leveling can even happen in the low equivalent heat flux. As part of the ETABUL research program, Alvarez et al. (1982) [86] evaluated the influence of boiling to leveling kinetics, in the form of temporal variation of the angle of repose. They introduced a

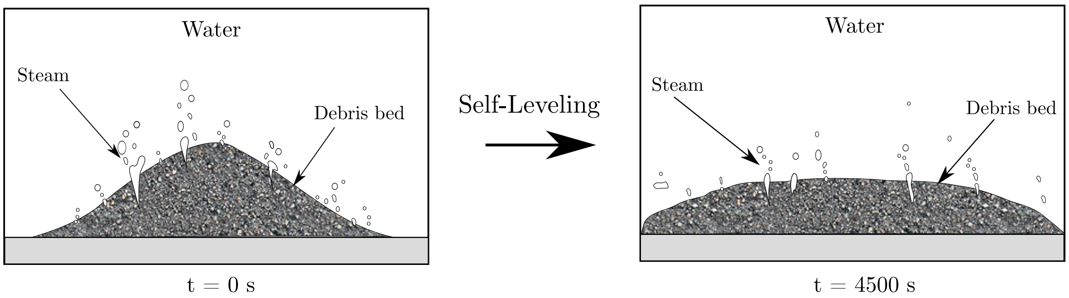

Figure 5.1: Debris bed leveling

resistor in a water-immersed bed, in order to simulate the residual power. They concluded that the boiling in the fluid promotes leveling and the obtained angles of repose are small. For a specific power in water of 3.1 W/cm^3, a limiting angle of repose of less than 2° is obtained after a time interval of between 1 and 3 hours. In a more recent series of experimental studies by Zhang et al. (2011) [144] depressurization water boiling and bottom heating were both employed to compare each other and to determine the importance of the particle physical parameters (size, density, shape) and the boiling intensity for the variation of the inclination angle, and hence for the self-leveling. Nevertheless, the steam generation density in these tests was two orders of magnitude smaller than in the real accident conditions. Cheng et al. [26] also conducted several visualization experiments to investigate the flow characteristics inside particle beds. By percolating nitrogen gas uniformly through a porous bed, Cheng et al. [27] also proposed an empirical model, to evaluate the transient variation in the inclination angle during the leveling process. A relatively good agreement was found to exist between the experimental data and the predicted inclination angle. However, it should be noticed that compared to the real accident scenario, all the above-mentioned experiments were performed with a low range of gas injection and the extrapolation of the modeling results to prototypical severe accident scenarios is not straightforward. Furthermore, all the proposed numerical models are based on empirical closures and assumptions, and the dynamics of the relocated particles induced by the boiling is still not sufficiently modeled and physically described.

5.2 Requirements for the experimental setup

In this chapter, the gas inflow effect on the debris formation process will be investigated experimentally using the BeForE-facility (already presented in Section 4.1). Steam bubbles generated from the decay heat in the corium particles were simulated using locally controlled injection of compressed air into the bottom of the bed. The dynamics of the porous bed under the influence of "space-" and "time-dependent" natural convection with an increasing rate of airflow resulting from the increased quantity of settled particles was simulated in a stepwise manner thanks to a real-time image processing and control system.

5.2.1 The air injection control

In order to study the effect of steam production on debris bed spreading, compressed purified air, used as a steam simulant, is injected from the bottom into the porous bed. In a hypothetical severe accident, because of the high temperatures and the generated decay heat, the corium debris is likely to generate more steam bubbles as more particles accumulate. Therefore, the steam generation rate increases with increasing bed height h. Hence, more air needs to be supplied to each of the air chambers according to the height of particles mound accumulated above it. The airflow rate in every air chamber is monitored and adjusted in time with motor-driven proportional valves (Buerkert Type 3280), which are in their turn controlled with an 8-channel analog voltage output system (Omega OM-USB-3103). Each channel is controlled with a self-developed DACS (data acquisition and control system) to deliver a voltage output range of 0 to 10 V.
Assuming a homogeneous bed with uniform heat release $W = 250$ W/kg at atmospheric pressure and saturated water, the superficial velocity of the generated steam can be estimated as follows:

$$v_{steam} = \frac{\rho_p \cdot (1-\varepsilon) \cdot W \cdot h}{\rho_s \cdot H_e} \tag{5.1}$$

Here, $H_e = 2.258$ MJ/kg is the latent heat of evaporation and ρ_p and ρ_s are the particle and steam densities, respectively. In order to achieve dynamically similar conditions for the steam production and the air injection into the porous bed, both flows must have the dimensionless **Blake**- and **Euler**-Numbers defined as:

$$\begin{aligned} B_{steam} = B_{air} &\Rightarrow \frac{\rho_s \cdot v_{steam} \cdot d_p}{\eta_s \cdot (1-\varepsilon)} = \frac{\rho_{air} \cdot v_{air} \cdot d_p}{\eta_{air} \cdot (1-\varepsilon)} \\ Eu_{steam} = Eu_{air} &\Rightarrow \frac{\Delta p_{steam}}{\rho_s \cdot v_{steam}^2} = \frac{\Delta p_{air}}{\rho_{air} \cdot v_{air}^2} \end{aligned} \tag{5.2}$$

The Blake-Number B is a generalization of Reynolds number for flow through the porous bed and is defined as the ratio of the inertial to the viscous forces. The Euler-Number Eu is used to characterize energy losses with the ratio of the frictional pressure drop inside porous beds to the kinetic energy per volume of the flow. From Equations (5.1)-(5.2), the superficial air velocity in each chamber can be estimated as a function of the local bed height by:

$$v_{air}(h) = \frac{\eta_{air}}{\eta_s} \cdot \frac{\rho_p \cdot (1-\varepsilon) \cdot W}{\rho_s \cdot H_e} \cdot h \tag{5.3}$$

Concretely and as illustrated in Figure 5.2, the gas flow rate is controlled locally on the top of every air chamber from the calculation of the averaged heap height on its upper side. And as a function of the bed height the steam velocity is then calculated and integrated over the chamber width to get the steam flow rates and the equivalent air flow rates Q_{air_i}.

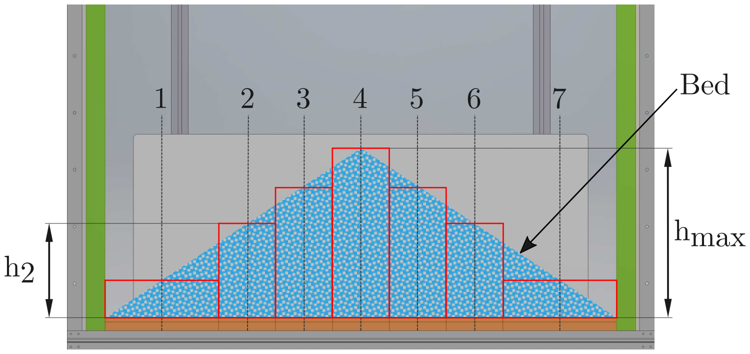

Figure 5.2: Calculation of the compressed air flow rates

5.2.2 Data acquisition and control system

During the experiments, the variation of the bed geometry is recorded by a digital video camera as motion pictures. In order to achieve a (nearly) real-time control of the proportional valves, the following control system; as illustrated in Figure 5.3; is set up:

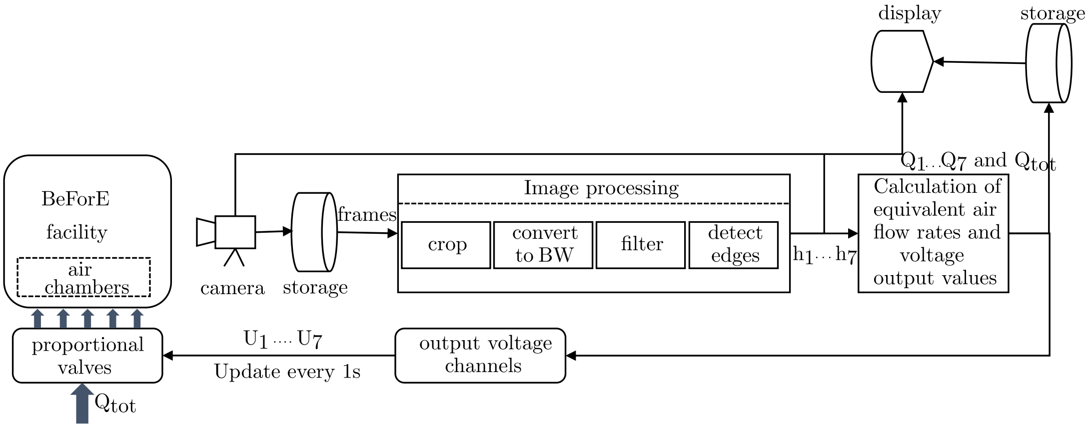

Figure 5.3: Data acquisition and control system

After the image processing of the stored frames equivalent air flow rates and the required voltage output values are calculated from the determined bed heights and via the output voltage every valve is controlled and updated every second.

5.2.3 Test procedures

Three groups of test scenarios were carried out: one was the bed formation under two-phase conditions (TPI: two-phase influence) with bubble-induced two-phase natural convection flow due to injection of air, and the other one was without bubble generation, which provided a reference situation (RE: reference experiment). The third group is the Self-Leveling of already built debris bed (SLE: Self-Leveling Experiments).

5.3 Experimental Observation

Previous studies have almost exclusively focused on the self-leveling of initially formed beds or only on the particles sedimentation without the influence of coolant boiling. This section points out some of the novel experimental findings encountered during the investigation of the influence of coolant boiling of the formation process.

5.3.1 Influence of gas injection on debris bed formation

Figure 5.4 shows a comparison between the cross-sectional profiles of debris beds formed with (TPI) and without (RE) the influence of interstitial gas flow for aluminum and coarse gravel respectively. Although all the four tests are carried out in the same experimental conditions, it can be concluded that, for the aluminum particles, in the absence of the gas inflow the particles are falling (mostly) in a narrow area in the center of the viewing bin, and the bed grew rapidly (see Chapter 4 for bed formation without coolant boiling). In the TPI tests, the upward gas flow was intersecting with the downward particles flow, altering its trajectory and broadening the particles over a wider region of the vessel. The resulting bed is then flatter and broader and rises slower than in the reference test. On top of the influence on the falling particles jet, the two-phase flow induces a movement of the upper surface of the already formed bed, which will start flowing in the form of episodic avalanches within a thin layer down the slope, contributing to the flattering of the bed. These results concur with the other studies alluded in Section 5.1 which have shown that the coolant boiling will lead to the flattering of particulate beds. However, the comparison of the coarse gravel beds in Figure 5.4 has shown that the resulting bed with TPI is higher than in the reference experiment[1]. In fact, without the two-phase influence (RE), the coarse gravel particles tend (under certain conditions) to form a concave bed, characterized by a dimple on the mound top (see Figure 5.5). This might be due to the differences in mass between the polydispersed particles and also due to the particles convection and its lateral entrainment forced by the continuous inflow of the following (heavier) particles (particles pushing is depicted by blue arrows on Figure 5.5). So, lighter particles tend to be pushed aside mainly by collision with the falling larger particles forming two small mounds separated by a dimple at the top.

---

[1] Note that the gas injection during the TPI experiment is only active during the formation process and stopped directly afterward.

Nevertheless, with increasing gas flow, the concavely shaped bed (bent inwards) turns into a convex one (curved outwards) due to the redistribution of the particles on the top of the quiescent formed bed and due to the resulting convective flow inside the vessel. To get a better understanding of this mound shape rearrangement, Figure 5.6 shows an example of the leveling of an already formed concave bed due to the gas injection from the bottom. It can be clearly seen how the particles are redistributed on both sides of the two heap tops leading to the flattering of the bed and the filling of the concavity at the top.

As a result, the formed bed with the larger concavity, i.e., without the two-phase influence, has a lower height than the same bed built under TPI conditions. It can also be deduced, that contrarily to what is always expected and initiated in former studies, the two-phase flow will not "always" lead to a flatter bed "during the formation process," and it can also change the typical mound shape of the debris bed from concave to convex shape, and hence change its coolability capabilities.

The conditions of the formation of concave beds have been addressed by a number of authors. For example, Shamsuzzaman et al. have observed in their investigation of particles sedimentation [119] that the dimple formation depends mainly on the particle diameter, nozzle height, and nozzle diameter (corresponding to the particles jet diameter in our study). By gravity driven discharge of slid particles from a nozzle into a cylindrical water pool, it was evinced that a transformation from convex to concave mound was observed by increasing either nozzle diameter or decreasing the particle diameter. The dimple area is also found in an increasing trend with the nozzle diameter.

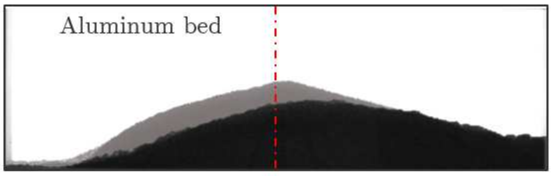

Background (gray) without flow (RE), foreground with flow (TPI)

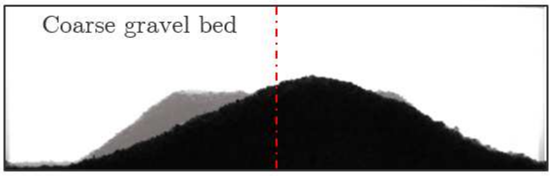

Background (gray) without flow (RE), foreground with flow (TPI)

Figure 5.4: Comparison of the formed bed with and without the two-phase flow

On the other hand, Sheikh et al. have investigated in their study [120] the sedimentation behavior of particles mixtures with different sizes. Their findings are in line with the

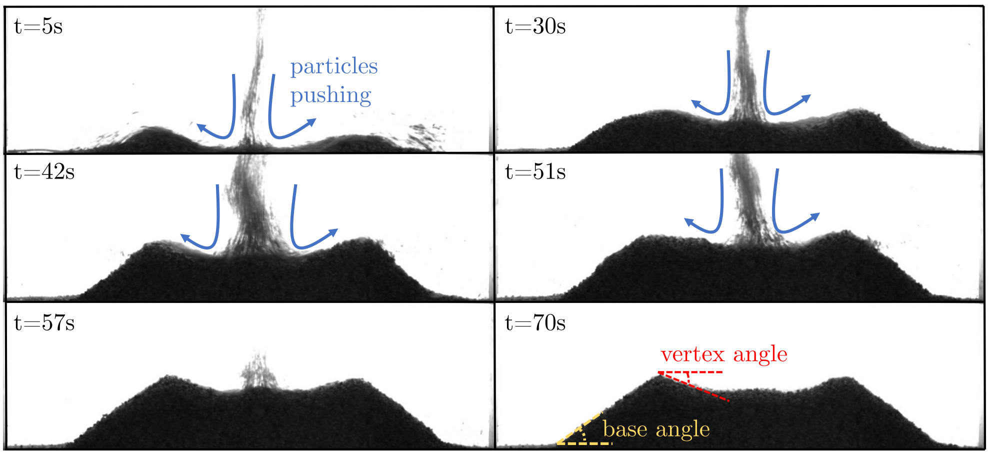

Figure 5.5: Formation of a concave bed
(Coarse gravel - without two-phase flow (RE))

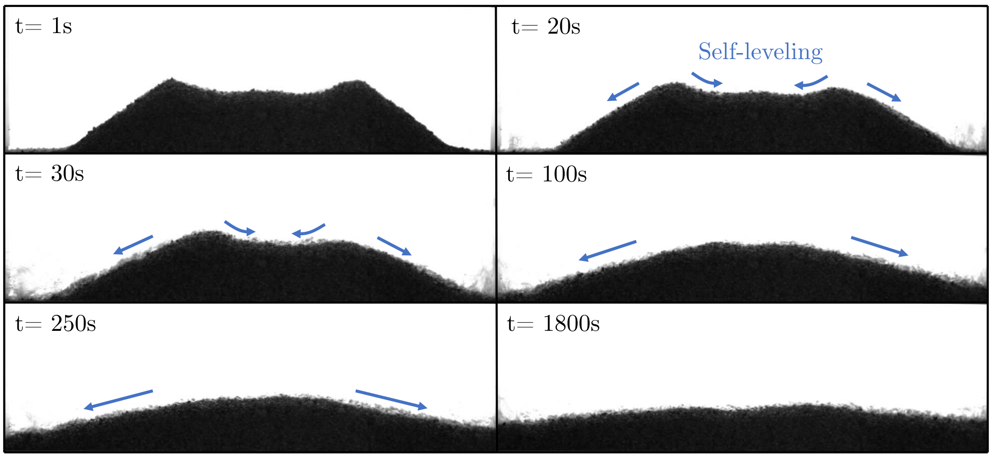

Figure 5.6: Self-leveling of already formed concave bed (Coarse gravel)

present work and the results evinced above and displayed in Figure 5.5. It was observed that due to the difference in volume and mass between the large and the smaller particles in binary multi-size mixtures, the lighter particles tend to be pushed aside by the larger particles, leading to a dimple formation and causing a lower bed height. It was also confirmed that a more significant concavity effect could be seen for larger diameter difference in the particles multi-size mixtures.

When dealing with the bed formation without coolant boiling, these experimental studies are in accordance with the present study. Moreover, it was shown in our research that the two-phase flow inside the vessel can change the mound shape of customarily formed concave beds in the quiescent conditions to a convex type with a higher bed height "at least in the beginning." Certainly, the continuous boiling will lead to the flattering of the bed afterward; nevertheless, this effect should be taken into account, since it is crucial for the bed coolability that the time scale of the self-leveling is smaller than the time scale for reaching dryout.

In real reactor conditions, the full melt jet fragmentation in the residual water of the lower plenum will lead to the formation of different solid particles with a size distribution between 0.6 and 6 mm. The formation of concave beds is therefore highly possible, and the consideration of this case in safety analysis codes would be of particular interest.

5.3.2 Self-leveling of initially formed beds

Investigating the self-leveling process of already formed beds with the same volume (20 L), Figure 5.7 shows the effect of particles diameter and the initial bed shape on the self-leveling process. Built under the same experimental conditions, clear deviations in the initial geometries can be observed (see Figure 5.7 *(left)*): aluminum forms a convex packed bed with a distinct mound top. Both the fine and the coarse gravel form a flatter bed with a slightly concave plateau. This results in a deviation in the starting height, and the direct comparison is only possible by comparing the relative height defined as the ratio of the actual to the starting heights. Both the aluminum and the fine gravel beds lose about 22% of their starting heights. In the same period, the coarse gravel bed loses about 26% of the starting height.

Comparing the bed cross-sections, it can be clearly seen that the coarse gravel forms a very compact bed that has two continuous flanks with angles of about 40°. Aluminum and fine gravel bed are more widely distributed, reducing the average angle of repose. A large angle of repose favors the movement and thus the displacement of the particles downslope. The faster coarse gravel spreading can also be explained with the effect of the wider particles size distribution. Another finding that can be deduced from this comparison is the effect of the particle shape on the bed leveling. The fine gravel and alumina particles have an equivalent size range and comparable densities but different forms. It is found that the leveling for rounded-edged particles (fine gravel) is slightly faster than for the sharped-edged ones (the aluminum bed). It is due to the decreasing effect of particle-particle and particle-bottom friction.

The effect of the gas flow intensity in the self-leveling of the coarse gravel bed can be seen in Figure 5.8. As mentioned, in other works [7], the bed self-leveling is normally slower for decreasing gas flow rates. Hence for $Q_2 \approx 1.3 \cdot Q_1$, the bed is 6% flatter than in the first experiment. For this gas intensity range, these observations are consistent with what has been found in previous studies.

However, for higher gas flow rates than 410 l/min a deviation from the expected progression can be observed. A higher airflow leads contrarily to expectations to the slowest self-leveling. This is caused by the high turbulent currents inside the vessel. In fact, the gas bubbles released from the bottom into the vessel induce the liquid as they rise due to the buoyant force, leading to bubble-driven flow, or the so-called bubble plume. The upward-moving buoyant jet will be redirected horizontally at the water surface into

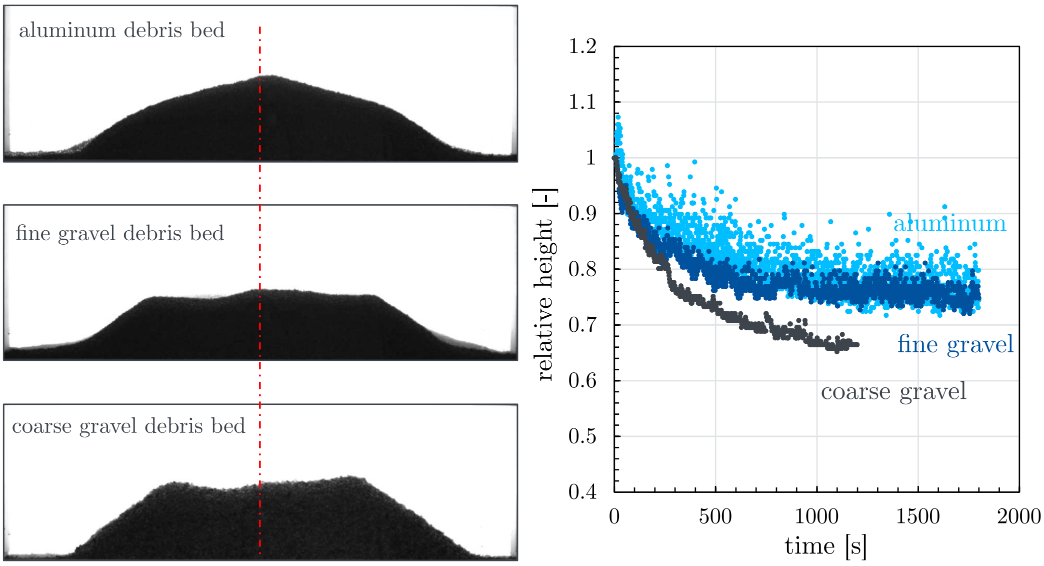

Figure 5.7: Effect of particle diameter and initial bed shape on the self-leveling: (left) initial bed shape; (right) relative bed height flattering

a radial spreading layer. And due to the wall effects, this bubble plume will be then redirected downward entraining more liquid and inducing a large-scale recirculation and vortexes inside the vessel. As shown schematically in Figure 5.9, the turbulent jet resulted from the bubble plume will entrain the particles to the center of the vessel against the self-leveling direction altering this process and leading to higher beds than expected, which can explain the slower flattering of the particles beds with higher gas intensities.

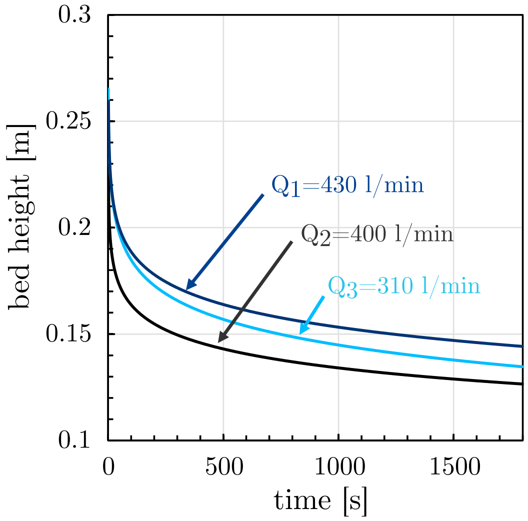

Figure 5.8: The influence of gas flow intensity on the debris bed height for the coarse gravel bed

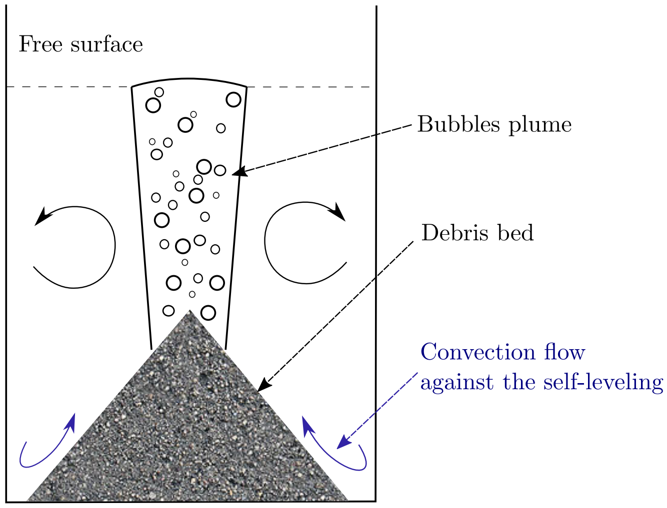

Figure 5.9: The effect of the bubble plume on the self-leveling process

5.4 Influence on the numerical modeling

The effect of a fluidizing gas on the formation process of debris bed is studied theoretically in this section. In line with previous experimental studies conducted by Basso et al. [8], the video recordings of the bed formation with gas injection and the leveling process have shown that two distinct regimes of particles spreading can be distinguished:

- **(i)** first, a rapid avalanche-like particles motion occurs at the beginning (for initially formed beds (SLE) or during the formation process for TPI-tests) until reaching a new stable angle of repose,

- **(ii)** and subsequently a slow particles spreading takes place until reaching a flat bed configuration. The latter regime is a slow process driven by the stochastic interactions of rising gas bubbles with the particles at the top bed surface.

The first observed behavior and the definition of this new angle of repose will be mathematically examined within the scope of this section.
The experimental observations have shown that for a gas flow below the minimum fluidization velocity, the particles on the top surface of the bed will start flowing in the form of episodic avalanches within a thin layer down the slope, similarly to the particles relocation and the avalanche-like motion on the bed top-surface already seen during the formation process (see Chapter 2). With the presence of coolant boiling, it was experimentally observed in the last sections that the bed will become flatter and wider depending on the local gas velocity. Hence the values of the angle of repose will be reduced until reaching a new value, which is different than the typical characteristic material property. This effect can be mathematically described and taken into account in the derivation and the adaption of the continuum model already developed in Chapter 2, which will be generalized for the description of the bed formation process as well for the further relocation of the particles due to the additional forces induced by the presence of the interstitial gas flow. The effect of momentum exchange and pressure drop in the porous flowing layer is included in its new description.
Therefore, the two-phase flow within the debris bed should be first described and modeled, before coupling it with the model simulating the particles surface flow.

5.4.1 Modeling of the two-phase flow within the bed

Three separate continuum phases, i.e. solid particles, liquid coolant, and the gas, are considered for the simplified modeling of the two-phase flow inside the porous bed. Assuming only vertical steam velocity, the mass conservation equations for the gas and liquid phases inside the bed are described one-dimensionally in the vertical direction as follows:

$$\begin{aligned} \frac{\partial\left(\varepsilon s_g \rho_g\right)}{\partial t}+\nabla \cdot\left(\varepsilon s_g \rho_g \overrightarrow{w}_g\right)&=\Gamma_{evap} \\ \frac{\partial\left(\varepsilon s_l \rho_l\right)}{\partial t}+\nabla \cdot\left(\varepsilon s_l \rho_l \overrightarrow{w}_l\right)&=-\Gamma_{evap} \end{aligned} \tag{5.4}$$

Where ε, $s_g=\alpha$, and $s_l=1-\alpha$ represent the porosity and volume fractions of gas and liquid in the porous bed respectively. α is the void fraction. Γ_{evap} represents the mass transfer rate due to evaporation/condensation. The terms $\overrightarrow{w}_g$ and $\overrightarrow{w}_l$ are the (physical) phase velocities and they are related to the superficial velocities $\overrightarrow{u}_g$ and $\overrightarrow{u}_l$ with:

$$\overrightarrow{u}_g=\varepsilon s_g \overrightarrow{w}_g \quad \text{and} \quad \overrightarrow{u}_l=\varepsilon s_l \overrightarrow{w}_l \tag{5.5}$$

Momentum conservation is assumed to be governed by friction between the fluids and solid particles, pressure gradient and buoyancy. Thus, time derivatives and inertial terms are neglected and the simplified momentum equations can be written as:

$$\begin{aligned} -\nabla p_g &= \rho_g \vec{g} + \frac{\vec{F}_{sg}}{\varepsilon s_g} + \frac{\vec{F}_{gl}}{\varepsilon s_g} \\ -\nabla p_l &= \rho_l \vec{g} + \frac{\vec{F}_{sl}}{\varepsilon s_l} + \frac{\vec{F}_{gl}}{\varepsilon s_l} \end{aligned} \tag{5.6}$$

Using the concepts of permeability κ and passability η (which are describing the capability of porous medium to transmit fluid), the solid-fluid frictional forces $\vec{F}_{sg}$ and $\vec{F}_{sl}$ can be then expressed as a function of the superficial velocities with the modified Ergun equations for two-phase flow through porous media as:

$$\begin{aligned} \vec{F}_{sg} &= \varepsilon s_g \left[\frac{\mu_g}{\kappa \kappa_{g_{rel}}} \vec{u}_g + \frac{\rho_g}{\eta \eta_{g_{rel}}} |\vec{u}_g| \vec{u}_g \right] \\ \vec{F}_{sl} &= \varepsilon s_l \left[\frac{\mu_l}{\kappa \kappa_{l_{rel}}} \vec{u}_l + \frac{\rho_l}{\eta \eta_{l_{rel}}} |\vec{u}_l| \vec{u}_l \right] \end{aligned} \tag{5.7}$$

With the relative permeabilities and passabilities defined as:

$$\kappa_{g_{rel}} = s_g^m \quad \text{and} \quad \kappa_{l_{rel}} = s_l^m \tag{5.8}$$

$$\eta_{g_{rel}} = s_g^n \quad \text{and} \quad \eta_{l_{rel}} = s_l^n \tag{5.9}$$

The exponents (m) and (n) are empirical constants that vary depending on the literature sources. For the relative passability, Lipinski (1982) [74] suggested $(m = 3)$, Reed (1982) [96] proposed $(m = 5)$, and Hue and Theonafous (1991) [48] suggested however $(m = 6)$. The relative permeability was always taken as $(n = 3)$. The single-phase permeability κ and passability η are given according to Ergun (1952) [36] by:

$$\kappa = \frac{\varepsilon^3 d_p^2}{150 \cdot (1-\varepsilon)^2} \tag{5.10}$$

$$\eta = \frac{\varepsilon^3 d_p}{1.75 \cdot (1-\varepsilon)} \tag{5.11}$$

which are also valid for irregularly shaped particles. The term $\vec{F}_{gl}$ in Equation (5.6) represents the interfacial friction between the fluids. There are two different approaches for the modeling of this drag force. Schulenberg and Mueller (1984) [115] proposed an empirical correlation for $\vec{F}_{gl}$ based on isothermal air/water experimental pressure drop measurements. Tung and Dhir (1988) [132] introduced another formulation where several flow regimes are distinguished and different interfacial friction coefficients were defined for each regime (i.e., the low and high void bubbly flow, the slug flow regime and the annular flow regime). A modified Tung and Dhir friction model was also developed and implemented in the system code MEWA by Rahman [95] and Schmidt [114], to increase its capability predicting the dryout heat flux (DHF) and to extend it for both top and bottom flooding situations over the whole bandwidth of particle size.

5.4.2 The combination of physical mechanisms and the adaption of the numerical model

When vertical stream of gas is passed through a granular bed, an additional drag force as a result of the gas pressure gradient is acting on the surface layer of the moving particles, which alters its movement. The balance between the main forces is shown schematically in Figure 5.10.

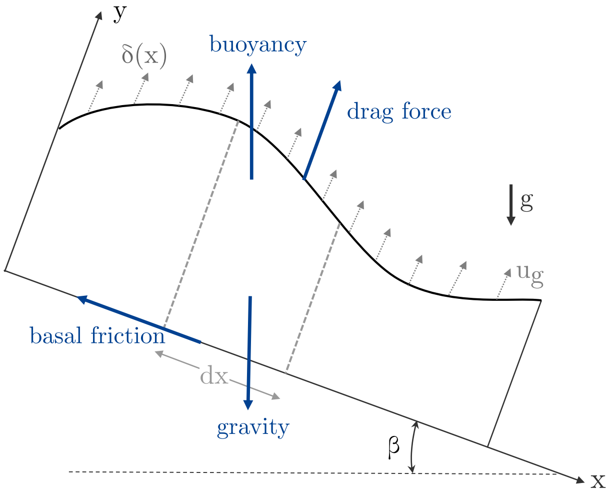

Figure 5.10: Schematic of the main forces acting on the surface flow of the moving particles

This additional drag force, changing the acting normal forces in the flowing layer, will influence the shear stress on the boundary between the layer and the quiescent bed. The Coulombic frictional stress can be then defined as follows:

$$\tau_{xy_c} = -\delta tan\left(\beta_s\right) \cdot \left(cos(\beta)\rho_s g - \nabla p_g\right) \tag{5.12}$$

Where $tan\left(\beta_s\right)$ is the effective coefficient of dynamic friction, and β_s is taken to be the characteristic angle of settlement of the used particles; as initiated in Chapter 2. A new modified static angle of repose $\tilde{\beta}_s$ can be calculated as a function of the bed height and the resulting gas flow according to the following definition:

$$\tau_{xy_c} = -\delta \rho_s g cos(\beta) tan\left(\tilde{\beta}_s(x,t)\right) \tag{5.13}$$

It yields:

$$tan\left(\tilde{\beta}_s(x,t)\right) = tan\left(\beta_s\right) \cdot \left(1 - \frac{\nabla p_g(x,t)}{\rho_s g cos(\beta)}\right) \tag{5.14}$$

The new definition of the angle $\tilde{\beta}_s(x,t)$ implied that the characteristic angle of settlement is no more a material property, which is constant across the entire calculation domain. However, the local angle of settlement $\tilde{\beta}_s(x,t)$ will decrease in time with higher beds under the influence of the increasing coolant boiling leading to a reduction of the friction forces and hence to an increase of the avalanche thickness on the mound top surface. According to this mathematical description and the experimental observations (see Figure 5.4 -upper photo-), the self-leveling of the particles bed will occur on the top surface of the bed in the form of episodic avalanches down the slope leading to a flatter and wider bed than the one built under quiescent conditions.

The same applies for the definition of the shear stress at the bed-avalanche interface $\tau_{xy_{y=0}}$ as described by Equation (2.12). It implies that the angle of movement β_m will be also similarly reduced. Thus, the new definition of the reduced angle of movement $\tilde{\beta}_m(x,t)$ is obtained:

$$tan\left(\tilde{\beta}_m(x,t)\right) = tan\left(\beta_m\right) \cdot \left(1 - \frac{\nabla p_g(x,t)}{\rho_s g cos(\beta)}\right) \tag{5.15}$$

Since the angle of movement β_m is defined as the maximum angle of repose, at which an avalanche starts flowing when exceeding it, it can be deduced from Equation (5.15) that the formed bed under two-phase flow conditions will settle at lower slope angles than the material's characteristic value. The slope angle at the mound top will be smaller than the angle of repose at its bottom, which will lead to an alteration of the bed overall shape.

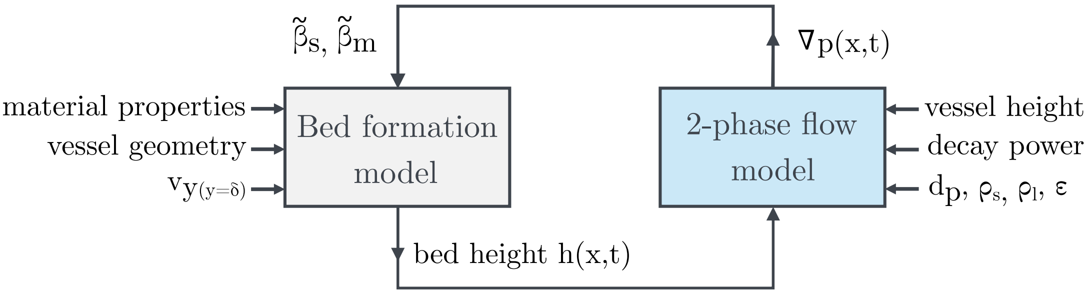

Figure 5.11: Coupling of the bed formation model with the two-phase model

A two-way coupling is considered between the model simulating the two-phase flow within the bed (as described in Section 5.4.1) and the bed formation model (as defined in Chapter 2). This is illustrated in Figure 5.11. The bed height function $h(x)$ is updated with the bed formation model at each time step. Based on the local height and the particles volume in each cell, the pressure drop ∇p will be actualized separately with the two-phase flow model, and the characteristic angles will be changed according to Equations ((5.14)) and (5.15). With these modified values, the bed formation model will be executed correspondingly at the subsequent time step.

The new simulation results of the coupled models are depicted in Figure 5.12-Figure 5.15. As can be seen from Figure 5.12, the particulate bed will be flatter and broader than the typically formed one under quiescent conditions (RE) (plotted with dashed lines). With increasing bed height, the angle of settlement will be correspondingly reduced (see Figure 5.13), and this decrease is at its maximum at the mound top, and it becomes less significant when going down the slope. This variable angle definition leads to the formation of slightly-bell shaped beds instead of the customarily conical shaped ones. An example of a heavily changed bed shape is plotted in Figure 5.14, where an artificially higher gas-liquid flow is applied leading to a significant reduction of the angle of repose and to a much flatter and wider bed than the original one formed without the two-phase influence with the same particles volume (plotted with the dashed line).

Figure 5.15 illustrates also the influence of the material density on the height leveling rate, defined as the percentage of the reduced height difference to the original height without the influence of coolant boiling. Apart from the observed increase of leveling effect with augmenting height, it is obvious that the low particles density favor the leveling process. The obtained leveling percentages and the obtained bed heights (during the formation process) are in accordance with the experimental results, performed under the same conditions (deviations of 2-3.4% were found, which is due to the influence of the convection flows and the suspension regimes already presented in Chapter 4).

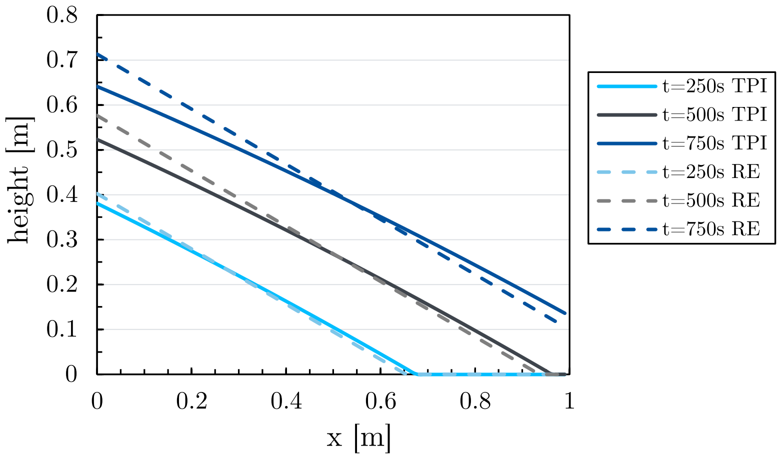

Figure 5.12: Comparison of the numerical results of the bed height with and without the influence of coolant boiling (closed system)

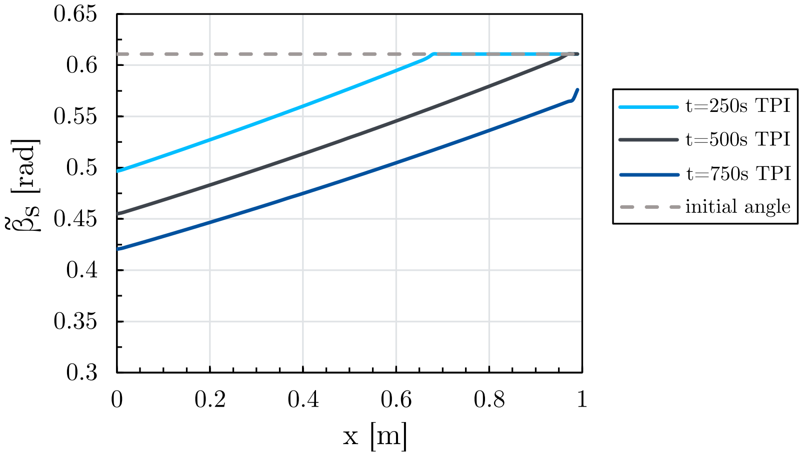

Figure 5.13: Influence of the coolant boiling on the angle of settlement

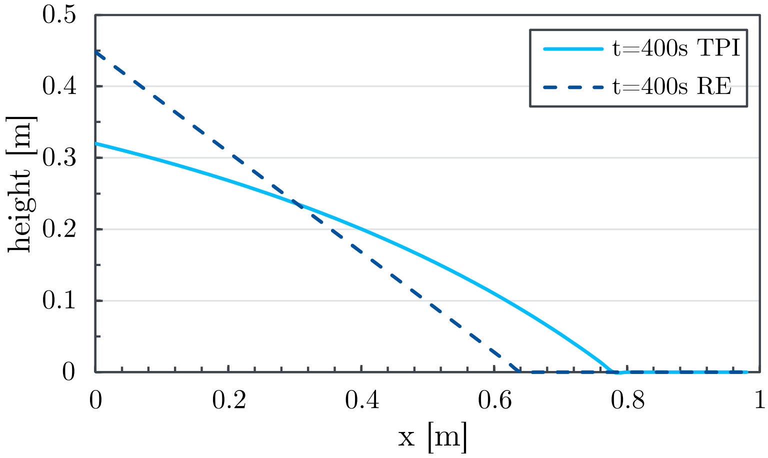

Figure 5.14: Influence of strong gas velocities on the numerical simulation of debris bed formation

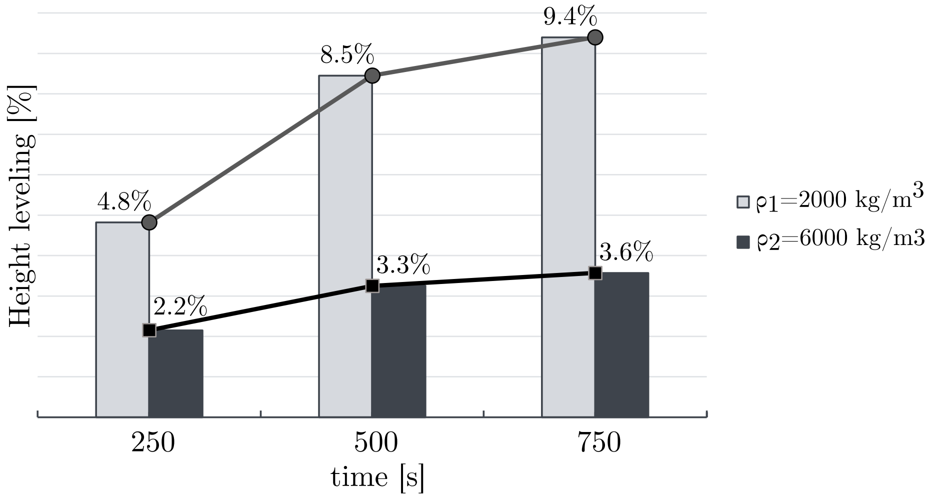

Figure 5.15: Influence of particles density on the bed leveling rate

The numerical simulations are consistent with the experimental findings and with the experimental results reported in other studies [8] [27] [40] [86]. Previous theoretical investigations on self-leveling were limited to the use of semi-empirical models to describe the height alteration process. With the coupling of the developed bed formation continuum model with a model simulating the two-phase flow within the bed, a fully-numerical model describing the first regime of avalanche-like particles motion during the leveling process could be provided. This allows a more accurate simulation of the bed formation process, which is of particular importance for the bed coolability and a decisive requirement for the nuclear accident progression and termination.

6

Model Discussion and Perspectives

In any model-based numerical simulations, few assumptions have to be made, in which subjective judgments could be involved to some degrees. In some cases, these assumptions can limit the applicability of the used equations. With the ultimate goal of producing an accurate and credible numerical results, the theories and the most important assumptions underlying the developed models in this work will be clearly stated and reviewed in the ensuing chapter in order to delineate the ranges of validity of the equations and asses whether the model representation of the problem is "reasonable" for its intended purpose. In general, knowing the assumptions and their possible effects will provide a good manner to discuss how the model could be extended and further developed to get a better accuracy or to extrapolate the results and the findings derived from this study. Hence, the second section in this closing chapter will consider the likely future of studies on the present physical problems and proposes some avenues for future research.

6.1 Assumptions and limitations in the numerical modeling

To investigate the particles deposition and relocation, the following assumptions were made:

- **Full fragmentation of the corium melt jet:** In the present study, it is assumed that the fully fragmented and solidified debris particles are behaving like cohesionless granular material. The full fragmentation requires a deep water pool in the cavity and a relatively small melt jet diameter to create a short jet breakup length. In an accident scenario, conditions such as failure of the reactor cavity flooding or very large melt discharge are therefore beyond the scope of this work. Agglomeration of partially liquid debris and formation of non-porous cake regions (as reported in some tests with prototypical corium melts [80] [124] or even with corium simulant materials [58][66]), occurring due to the incomplete melt jet fragmentation were not taken into account in the present study.

- **Bed homogeneity:** in this study, the focus is on the formation and the behavior of all-porous solid debris beds with homogeneous properties. The key assumption in this "continuum" modeling is that the internal structure of the bed is homogeneous and isotropic, regarding its main properties such as the porosity, particles diameter, permeability, and passability. The developed numerical model is based on the assumption of monodispersed particles. Therefore, an equivalent mean diameter was defined for all the used particles mixtures in the experimental validation. In the conducted sensitivity analysis, it could also be proved that uncertainty in the determination of the particles size does not have a big influence on the bed height and shape compared to other model inputs. The other previously treated issues related to the polydispersity of the debris particles (e.g., demixing and stratification during the sedimentation, lateral relocation of the light particles due to convection flows) are beyond the scope of this work. This means that single representative values for the particle size and the porosity are applicable throughout the bulk of the bed. However, in the real accident scenario, the jet fragmentation and solidification is more likely to lead to the formation of debris beds with complex internal structure (e.g., regions with different porosities within the bed), as stated in the post-accident examinations of TMI-2. The present study and the developed continuum models rely on an averaging of the bed properties since it is not always possible to account for all the bed configurations resulted from the corium discharge.

- **No particle remelting:** Particles remelting was not considered in the framework of this study; at least during the bed formation process. In reality, remelting and re-agglomeration of the melt after it reaches the pool bottom is possible when the average enthalpy of the particles is above that of the melting point.

- **Density preserving in the flowing layer (incompressibility):** since the dilatation of the flowing layer is small in the present slow flows, it is assumed that the bulk density in the thin flowing layer is constant and nearly equal to the bed density. In fact, the effect of dilatancy was neglected in the present modeling. In fact, volume changes can occur at the instants of flow inception and during particles settling, or due to wall effects [51] [136] [137], but the thickness changes due to the associated dilatation are still minimal, and they are not of great importance within the main flow region, and the assumption of a constant density will not influence the model results. The model equations are not a function of the material density. Therefore, the model can be applied to all kind of particles, behaving like cohesionless granular material.

- **Assumptions about the steam generation in the bed:** steam generation due to the coolant boiling in the debris bed was simulated by air injection from the bottom of the water vessel at room temperature, based on the assumptions of a homogeneous bed with uniform volumetric heat release rate, only vertical steam velocities, and saturated coolant conditions. In the real condition, the subcooling and pressure effect should be considered for the water and steam properties. Moreover, it is assumed that steam generation is determined only by the radioactive decay heat power of the corium particles, and it is not affected by the phenomena of the coolant ingression inside the particles bed.

The above-stated assumptions can be justified, and they are not invalidating the model to the extent that they would not be able to reproduce "sufficiently" accurately the debris bed formation. The model validation with experimental data have shown that a good agreement could be found between the numerical simulations and the corresponding experimental findings for the relative heavy particles, which is the fulfilled for the corium particles in the real reactor conditions (the density for the corium changes to 4 times as great than the used particles in the experimental facility). Actually, the investigations of samples obtained from the damaged reactor in TMI-2 showed that the density of the samples was between 7.45 and 9.4 g/cm^3, although the density of uranium dioxide (10.97 g/cm^3) and zirconium (5.6 g/cm^3) are outside the found range. However, these values are well expected due to the finding of a variety of materials within the sample and the porosity of the solidified corium.

In the end, it must be mentioned that even the violation of some of the above-listed assumptions (e.g., the density preserving in the flowing layer) may be minor or for short duration and length. But it is worth noticing that this (short-lived) violation will not lead to the failure of the model equations or a major limitation of its applicability.

6.2 Model extensions

Model extension regarding the bed formation

The bed formation modeling is based on the assumption of the monodispersity of the solid particles and the homogeneity of the bed (i.e., constant porosity in the bulk of bed). However, it has been shown in the conducted experiments that the use of polydispersed particle mixtures could lead to the formation of stratified beds. In fact, the underlying full melt jet fragmentation in the residual water of the lower plenum yields to the formation of solid particles with size distribution, in which approximately 95% of the mass is between 0.6 and 6 mm. During the sedimentation, the larger solid particles will fall more quickly to the bottom due to their smaller (cross-sectional area / volume) ratio, while smaller particles can "float" longer in the water or even be transported to the top (or laterally ejected) by the convection flows in the vessel. In this manner, a kind of particles segregation may take place in which smaller particles settle later on a previously formed heap of larger particles, which can lead to a layered bed with different porous zones. An example of the influence of inhomogeneous porosity and a non-symmetric geometry on the debris bed coolability is shown in the following MEWA-simulations conducted by Hartmann et al. [47], as illustrated in Figure 6.1. Therefore, an inhomogeneous particle bed (bed 3) having an inner zone of lower porosity covered by an outer zone of higher porosity was considered. In this dense inner region (about 30% of the bed volume), a low porosity of 20% is considered. Loose debris with a porosity of 40% is assumed around this inner region. The numerical results in Figure 6.1 and Table 6.1 show that the lower porosity limits water ingress through the less porous region. In bed 3, complete quenching cannot be achieved before reaching the melting temperature in the denser region.

Table 6.1: Comparison of the numerical results of quench simulations of different porosity configurations (MEWA3D) [47]

	Bed 1	Bed 2	Bed 3
Configuration	symmetrical homogeneous	non-symmetrical homogeneous	non-symmetrical inhomogeneous
Porosity	$\varepsilon = 0.4$	$\varepsilon = 0.4$	$\varepsilon_1 = 0.4 \rightarrow 70\%$ of the mass $\varepsilon_2 = 0.2 \rightarrow 30\%$ of the mass
Max. particle temperature	1985 K	1923 K	2802 K
Quench-time	2300 s	2150 s	4230 s

These findings confirm the necessity for a more detailed study of the stratification phenomenon and the influence of polydispersity on the bed formation and hence on the dryout behavior of inhomogeneous beds. The consideration of the polydispersity effect in the continuum modeling is though very challenging, and few dedicated experimental studies, empirical descriptions, and correlations may be certainly needed.

Model extension regarding the self-leveling

The experimental investigations have shown that high steam production due to the decay heat in the bed can lead to a deceleration of the self-leveling. This can be explained by the high convection currents inside the vessel due to the oscillating bubbles plume and its interaction with the particles and with the water surface. It was found that the convective flow will entrain the particles to the center of the vessel against the self-leveling direction altering this process and leading to higher beds than expected, and thus to less coolable debris beds. Therefore, a specific and more detailed numerical and experimental investigations of this mechanism and the interaction between the turbulent dispersed gas bubbles and the deposing particles will be required. In fact, the flow resulting from an underwater gas release and the hydrodynamics of bubble plume in general are also of practical interest for the applied ocean research and the chemical and process engineering. Models, equations, and experiments for the buoyant plume formed from air bubbles have

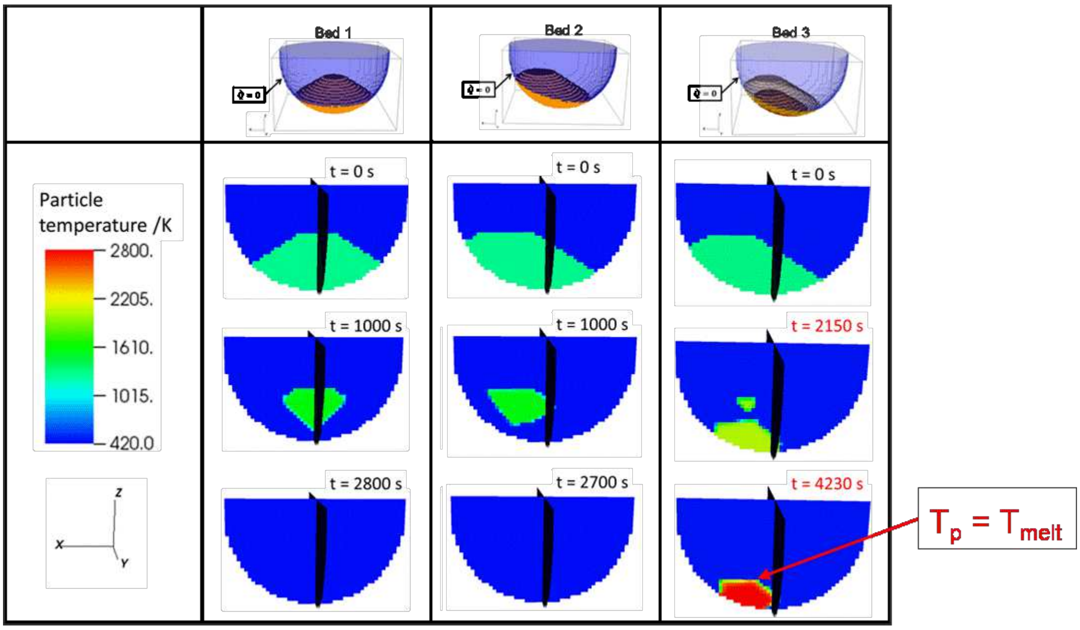

Figure 6.1: Distribution of the particle temperature in the bed (Simulations with MEWA3D) [47]

been developed by many authors in these fields of application [3] [17] [37] [121]. Based on these previous works, the modeling of a meandering bubble plume inside the vessel and specifically the study of the interaction between the turbulent dispersed air bubbles and the deposing particles as well as its coupling with the presented models in this work will contribute to a more realistic and reliable simulation of the debris bed behavior, the sedimentation and the self-leveling.

"How do we know that the creations of worlds are not determined by falling grains of sand? Who can understand the reciprocal ebb and flow of the infinitely great and the infinitely small, the echoing of causes in the abyss of being and the avalanches of creation?"

- Victor Hugo, Les Misérables -

7

Summary and Conclusions

The coolability of particulate debris beds is one of the crucial issues during the late phase of severe accidents in light water reactors. In a hypothetical severe accident, a deep pool of water can be employed in the lower drywell of the containment, to cool the core melt materials discharged from the reactor pressure vessel after its failure. By contact with water, the molten corium will fragment, solidify and settle at the bottom of the cavity forming a mound-shaped porous bed. The preeminent goal becomes how to prevent the re-melting of the debris in consequence of insufficient cooling and ensure its long-term coolability. It has been shown in many studies that bed shape and height are among the most critical factors determining the heat removal capability by natural convection of the coolant. Hence, the understanding of the bed formation process is of interest in the field of the nuclear safety analysis for the assessment of debris bed coolability.

Since most previous studies of ex-vessel severe accidents were limited to the assumption of the whole bed, being fixed and also initially established at a uniform temperature is not realistic, the present work concentrates on the development of a numerical module, simulating solid particles dynamics, and on its validation with experimental data, with the final aim of clarifying the bed formation mechanism.

Achievements

The modeling concept

According to different experimental findings and observations, it is assumed in the present work, that for fully fragmented melt jet, the solidified particles are behaving similarly to granular material. Once pouring on a vertical surface from a single point, a conically shaped bed will be most probably formed. By exceeding a characteristic maximum slope angle, an avalanche will start and particles will flow down the slope within a thin layer on the top of a nearly quiescent pile. The dynamics of the particles within this surface flow are described with a two-dimensional continuum model. The mathematical model is based on the depth-averaging of the mass- and momentum-conservation equations in this flowing layer, taking into account the newly deposed particles as well as the erosion and the absorption of the flowing particles from and into the particulate bed.

Implementation and model verification

The hyperbolic system of the model equations could be discretized and implemented in FORTRAN with the use of different numerical methods, which were compared regarding its accuracy and performance. For the present work, it was concluded that the Roe-solver could deliver satisfying results of the bed formation process. The presented model could also be verified with analytical solutions. It was shown that the numerical simulations with the Roe-solver are in excellent agreement with an analytical solution of the flowing layer thickness in the steady state, achieved during bed formation in a geometry with open boundaries. Moreover, a grid convergence study was performed and it showed, that the formally used second-order numerical method was reduced to first order at the discontinuities positions via the slope limiting procedure aiming at preventing numerical oscillations. The results of the systematic grid refinement study were uniformly reported with the use of the grid convergence index (GCI) suggested by Roache. Before model validation, the numerical uncertainties had been quantified and classified prior to this step to elucidate the model characteristics that will be important to monitor during experimental tests and to study the effect of the uncertainties in the input parameters on the bed geometry. The scalar sensitivity analysis showed that the bed height is "mainly" determined and influenced by the velocity of the deposed particles $v_{y_{y=\delta}}$ and the melt jet diameter (referred to as the opening Δw in the model). As expected, the bed will become higher for increasing values of those both inputs (i.e., higher beds for increasing mass flow rates of the solidified particles). Less decisive is the angle of settlement β_s. It is observed that the bed becomes flatter for higher difference between both characteristic angles $\Delta\beta = \beta_m - \beta_s$ (with β_s being the angle of settlement and β_m is the angle of movement). Compared to other variables, it could also be concluded that the particles diameter does not have a big influence on the bed height (however, both the particles diameter and the porosity are crucial and determinant for the coolability).

Model validation

With the aim of reducing the uncertainties in the simulation code and ensure the validity of the performed simulations, the bed formation model was validated with experimental data. Therefore, the test facility "BeForE" was newly designed and built at the Institute of Nuclear Technology and Energy Systems (IKE) within the framework of this thesis aiming at delivering the needed experimental data for the validation process. A series of tests were conducted using different shaped and multi-size mixtures of particles. During the experiments, the variation of the bed geometry was recorded by a digital video camera as motion pictures. In order to achieve a (nearly) real-time control of the facility, a dedicated data acquisition and control system (DACS) was developed and set-up. It was found, that due to the various interactions between solid particles and the water vessel, different particles deposition and relocation regimes could be identified depending on the particles diameter and density:

- **Sliding regime (inertial-dominant regime)**: this regime can be observed for the heavier particles (in the case of gravel $\rho = 2.54$ g/cm^3, it corresponds to $d_p \geq 3$ mm approximately). Due to their inertia, particles are falling down vertically in the water vessel and form a delta-shaped bed until reaching the critical angle of repose. Then the slope will remain constant and the particles are "sliding" down the slope within a thin layer on the top of the nearly-quiescent heap, as initiated and assumed in Chapter 2. Unlike the below-presented regimes, the sedimentation was not heavily influenced by the fluid convection flows inside the vessel or by the following particles jet. This regime is dominated by the particles inertia and the particle-particle interactions (friction, collision) already assumed in the modeling concept (see Chapter 2).
- **Convection-dominant regime**: this regime is found to exist for the less heavy particles (for gravel and aluminum particles with 1.5 mm$< d_p <$ 3 mm). Forced by the continuous inflow of particles, a pool convection can occur leading to lateral displacement of the smaller (and lighter) particles. At the early stage, the pool convection may lead to the formation of (initially) concave beds with two mounds at its top. Depending on the mass flow rate and the jet diameter (more precisely depending on the ratio d_p/W_p, with W_p being the release pipe/jet diameter), the final mound top shape may change from concave to convex. The relative smaller particles can also be pushed away by the subsequent particles flow, leading to a decreasing of the bed height.
- **Particle-suspension regime**: for the lightest particles (in our tests represented by the sand particles), this regime could be observed for small diameters (for sand $d_p \leq 1.5mm$). Due to their decreasing inertia, these light particles are more likely to be suspended in the water vessel. The poured particles tend to be ejected by the fluid convection inside the bed and to also be distributed (nearly in a uniform way) inside the vessel. The suspended particles will sediment gradually on the pool bottom leading to the flattering of the bed.

The comparison between the experimental results and the numerical simulations showed that the model is overestimating the bed height and underestimating its width (with a mean error of 17.5% for coarse gravel bed height in the performed test simulations). It can be explained by the fact that this continuum model is only taking into account the particles sliding and cannot simulate the convection flow or the suspension of individual smaller particles. Therefore, the numerical simulation is in better agreement with the reality for the case of the heavier particles, which should be owing to the absence of these phenomena. Nevertheless, it can still deliver a very good prediction of the reality for smaller particles. In real reactor application, the corium solidified particles have the same size distribution but a four-time greater density, which will lead certainly to a better agreement between the numerical simulations and the real corium behavior.

Study of the self-leveling process

The geometrical configuration of the porous bed, and hence its ability of decay heat removal, can also change due to the particles redistribution induced by steam production within the bed. In this work, the influence of steam production on bed formation was investigated experimentally with the same BeForE-facility. A series of experiments were conducted by discharging solid particles in two-dimensional viewing vessel, while air bubbles simulating the steam production are injected simultaneously from the bottom. Depending on the quantity of the settled particles on the top of each section of the vessel, air flow rate was so monitored and adjusted in real-time with the dedicated DACS to simulate the corresponding amount of steam produced by the similar quantity of debris. In addition to the expected outcome that two-phase flow inside the vessel alters the particles sedimentation process resulting in broader and flatter bed than under quiescent conditions, the experimental observations had provided new data for the investigation of the particles redistribution mechanism. It was shown that:

- In the case of customarily formed concave beds in the quiescent conditions (due to the differences in mass between the polydispersed particles or the lateral entrainment of smaller ones forced by the continuous inflow of the following (heavier) particles), the presence of the gas flow can change the mound shape to a convex type with a higher bed height in the beginning. So, contrarily to what is always expected and initiated in former studies, the two-phase flow will not automatically lead to the formation of flatter beds, and it can also change the typical mound shape of the debris bed from a concave to convex shape, which can influence in its turn the bed coolability.

- One of the other interesting findings is the influence of the gas flow intensity on the self-leveling. Most of the previously performed experiments on this topic were conducted with a low range of gas injection, and the extrapolation of the modeling results to prototypical severe accident scenarios is not straightforward. For example, and as mentioned, in other works [7], the bed self-leveling usually is faster for increasing gas flow rates. That was verified and confirmed in our experiments for gas flow rates smaller than a certain limit value (e.g. 410 l/min for gravel particles). However, for higher rates, a deviation from the expected progression can be observed. A higher airflow leads contrarily to expectations to the slowest self-leveling. This is caused by the high convection currents inside the vessel. The convection flow resulted from the bubble plume will entrain the particles to the center of the vessel against the self-leveling direction altering this process and leading to slower particles redistribution and consequently to higher beds than expected.

The effect of gas injection on the formation process of debris bed is then studied theoretically. The experimental observations have shown that for a gas flow below the minimum fluidization velocity, the particles on the top surface of the bed will start flowing in the form of episodic avalanches within a thin layer down the slope, similarly to the modeled avalanches seen during the formation process. The bed will become flatter and broader. Hence the values of the angle of repose will be reduced. When vertical steam of gas is passed through a granular bed, an additional drag force as a result of the gas pressure gradient is acting on the surface layer of the moving particles, which alters its movement. Through the balance between the main forces and the definition of the shear stress acting on the flowing particles layer, new definitions of the angles of repose are derived. It becomes not only a characteristic parameter of the particles but also dependent on the two-phase flow inside the bed and the resulting pressure drop on its surface. Under the influence of the coolant boiling, both β_s and β_m will become smaller leading to the formation of flatter and wider beds than the ones formed without the consideration of steam production.

The developed continuum model could be successfully adapted to take into account the self-leveling phenomenon by coupling it with a numerical model simulating the two-phase flow within the bed. This two-way model-coupling and the consideration of the reduced angles of repose enable more accurate numerical simulations of the bed formation process in degraded cores of light water reactors.

Models discussion

Predictions of complex events like bed formation and more generally granular material dynamics require simplifications of the process in the form of conceptual assumptions, as well as mathematical and physical models. In general, these models are a simplified and an abstract mirrors of the reality, which allow drawing conclusions about the real applications (here severe accident research), but it may at the same time be limited due to different theoretical and practical criteria. Therefore, the different assumptions underlying the developed models are clearly stated and reviewed in Chapter 6 in order to delineate the ranges of validity of the equations and asses whether the model representation of the problem is reasonable for its intended purpose, and if the data can be straightforwardly adapted or extrapolated to the different accident scenarios and reactor applications. The knowledge of the model limitations paves the way for the extension of the present models and can open up some entirely new avenues of research (see Section 6.2).

The above-mentioned conclusions and works are summarized in Figure 7.1, showing the different stages of the thesis.

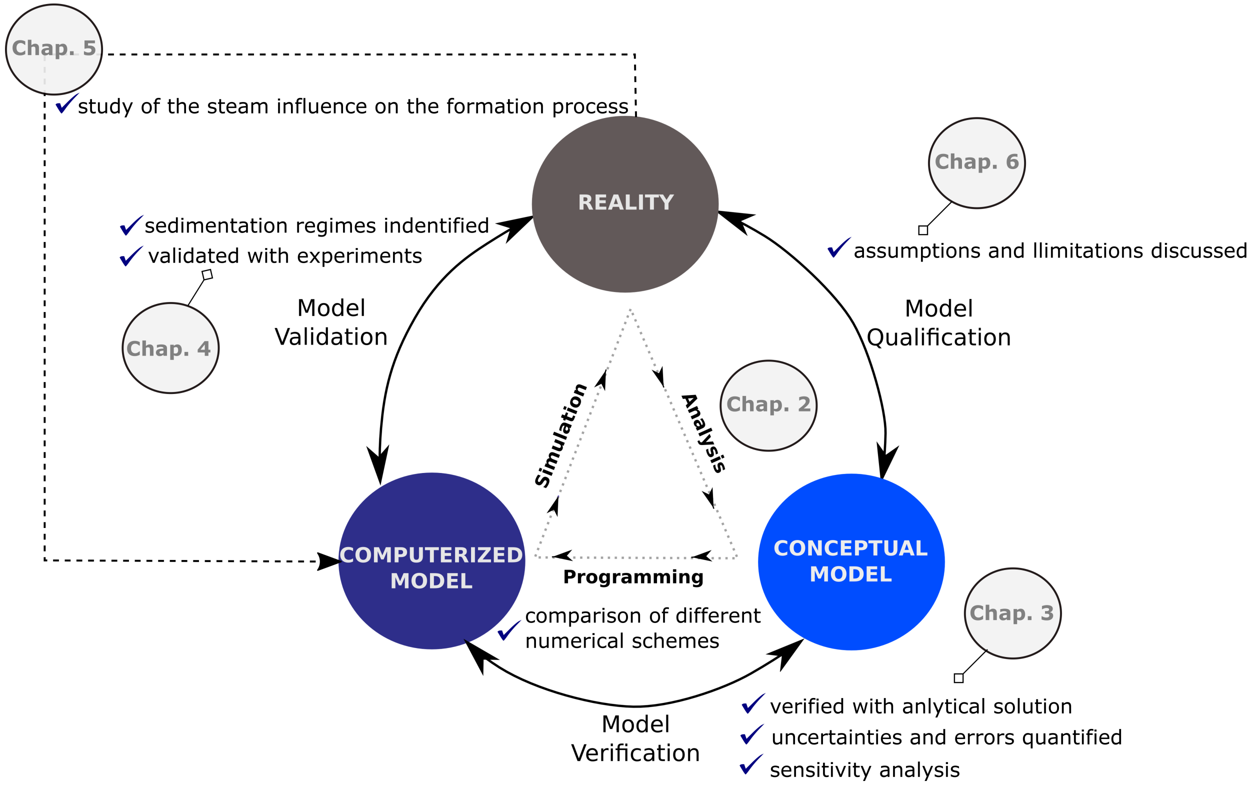

Figure 7.1: Summary of the present work

Bibliography

[1] *The Fukushima Daiichi Accident.* International Atomic Energy Agency, Vienna, Austria, 2015. (page: 7)

[2] H. Alsmeyer, G. Albrecht, G. Fieg, U. Stegmaier, W. Tromm, and H. Werle. Controlling and cooling core melts outside the pressure vessel. *Nuclear Engineering and Design*, 202(2-3):269–278, 2000. (page: 9)

[3] P. E. Anagbo and J. K. Brimacombe. Plume characteristics and liquid circulation in gas injection through a porous plug. *Metallurgical Transactions B*, 21(4):637–648, 1990. (page: 99)

[4] R. A. Bagnold. Experiments on a gravity-free dispersion of large solid spheres in a newtonian fluid under shear. *Proceedings of the Royal Society A: Mathematical, Physical and Engineering Sciences*, 225(1160):49–63, 1954. (page: 20, 23)

[5] J. W. Banks, T. Aslam, and W. J. Rider. On sub-linear convergence for linearly degenerate waves in capturing schemes. *Journal of Computational Physics*, 227(14):6985–7002, 2008. (page: 46)

[6] L. Barleon and H. Werle. Dependence of dryout heat flux on particle diameter for volume- and bottom-heated debris beds. Technical Report KfK–3138, 1981. (page: 10)

[7] S. Basso. *Experimental and Analytical Investigation of Particulate Debris Spreading.* Master thesis, KTH Engineering Sciences, Stockholm, Sweden, 2011. (page: 14, 52, 84, 104)

[8] S. Basso. *Particulate debris spreading and coolability.* PhD thesis, KTH, Nuclear Power Safety, 2017. (page: 14, 86, 93)

[9] S. Basso, A. Konovalenko, and P. Kudinov. Empirical closures for particulate debris bed spreading induced by gas–liquid flow. *Nuclear Engineering and Design*, 297:19–25, 2016. (page: 14, 52)

[10] S. Basso, A. Konovalenko, S. E. Yakush, and P. Kudinov. The effect of self-leveling on debris bed coolability under severe accident conditions. *Nuclear Engineering and Design*, 305:246–259, 2016. (page: 52)

[11] A. Bermudez and M. E. Vazquez. Upwind methods for hyperbolic conservation laws with source terms. *Computers & Fluids*, 23(8):1049–1071, 1994. (page: 29)

[12] D. Bittermann, U. Krugmann, and G. Azarian. EPR accident scenarios and provisions. *Nuclear Engineering and Design*, 207(1):49–57, 2001. (page: 9)

[13] C. Blahnik, C. S. Kim, R. Thuraisingham, and S. Nijhawan, editors. *Modular accident analysis program for CANDU reactors*, 1991. (page: 13)

[14] N. Blomqvist. On a measure of dependence between two random variables. *The Annals of Mathematical Statistics*, 21(4):593–600, 1950. (page: 55)

[15] F. Bouchut, A. Mangeney-Castelnau, B. Perthame, and J.-P. Vilotte. A new model of Saint Venant and Savage–Hutter type for gravity driven shallow water flows. *Comptes Rendus Mathematique*, 336(6):531–536, 2003. (page: 16)

[16] D. Bradley and G. Roth. Adaptive thresholding using the integral image. *Journal of Graphics Tools*, 12(2):13–21, 2011. (page: 66)

[17] I. Brevik and R. Killie. Phenomenological description of the axisymmetric air-bubble plume. *International Journal of Multiphase Flow*, 22(3):535–549, 1996. (page: 99)

[18] J. M. Broughton, P. Kuan, D. A. Petti, and E. L. Tolman. A scenario of the Three Mile Island Unit 2 accident. *Nuclear Technology*, 87(1):34–53, 1989. (page: 6)

[19] M. Buck. *Modelling of the late phase of core degradation in light water reactors.* PhD thesis, Universität Stuttgart. (page: 6, 7)

[20] M. Bürger, M. Buck, W. Schmidt, and W. Widmann. Validation and application of the WABE code: Investigations of constitutive laws and 2D effects on debris coolability. *Nuclear Engineering and Design*, 236(19-21):2164–2188, 2006. (page: 10)

[21] M. A. Carrigy. Experiments on the angles of repose of granular materials. *Sedimentology*, 14(3-4):147–158, 1970. (page: 21)

[22] I. Celik and O. Karatekin. Numerical experiments on application of richardson extrapolation with nonuniform grids. *Journal of Fluids Engineering*, 119(3):584, 1997. (page: 44, 47)

[23] S. Chapman, T. G. Cowling, and D. Burnett. *The mathematical theory of non-uniform gases: An account ot the kinetic theory of viscosity, thermal conduction and diffusion in gases.* Cambridge mathematical library. Cambridge Univ. Press, Cambridge, 3rd ed. reprinted. edition, 1999. (page: 20)

[24] P. Chatelard, J. Fleurot, O. Marchand, and P. Drai. *Assessment of ICARE/-CATHARE V1 Severe Accident Code.* 2006. (page: 13)

[25] P. Chatelard, N. Reinke, S. Arndt, S. Belon, L. Cantrel, L. Carenini, K. Chevalier-Jabet, F. Cousin, J. Eckel, F. Jacq, C. Marchetto, C. Mun, and L. Piar. ASTEC V2 severe accident integral code main features, current V2.0 modelling status, perspectives. *Nuclear Engineering and Design*, 272:119–135, 2014. (page: 13)

[26] S. Cheng, D. Hirahara, Y. Tanaka, Y. Gondai, T. Matsumoto, K. Morita, and K. Fukuda. Experimental study of bubble behavior in a two-dimensional particle bed with high solid holdup. In *Proceedings of the 18th International Conference on Nuclear Engineering: Volume 4, Parts A and B*, pages 697–704. ASME, May 2010. (page: 78)

[27] S. Cheng, Y. Tanaka, Y. Gondai, T. Kai, B. Zhang, T. Matsumoto, K. Morita, K. Fukuda, H. Yamano, T. Suzuki, and Y. Tobita. Experimental studies and empirical models for the transient self-leveling behavior in debris bed. *Journal of nuclear science and technology*, 48(10):1327–1336, 2011. (page: 78, 93)

[28] N. Chikhi, N. G. Nguyen, and J. Fleurot. Determination of the hydrogen source term during the reflooding of an overheated core: Calculation results of the integral reflood test QUENCH-03 with PWR-type bundle. *Nuclear Engineering and Design*, 250:351–363, 2012. (page: 7)

[29] R. Clavier, N. Chikhi, F. Fichot, and M. Quintard. Experimental investigation on single-phase pressure losses in nuclear debris beds: Identification of flow regimes and effective diameter. *Nuclear Engineering and Design*, 292:222–236, 2015. (page: 63)

[30] B. Clément, N. Hanniet-Girault, G. Repetto, D. Jacquemain, A.V Jones, M.P Kissane, and P. von der Hardt. LWR severe accident simulation: Synthesis of the results and interpretation of the first Phebus FP experiment FPT0. *Nuclear Engineering and Design*, 226(1):5–82, 2003. (page: 12)

[31] R. Courant, K. Friedrichs, and H. Lewy. Über die partiellen Differenzengleichungen der mathematischen Physik. *Mathematische Annalen*, 100(1):32–74, 1928. (page: 31)

[32] L. A. Dombrovsky, M. V. Davydov, and P. Kudinov. Thermal radiation modeling in numerical simulation of melt-coolant interaction. *Computational Thermal Sciences*, 1:1–35, 2009. (page: 14)

[33] J. Duran. *Sands, Powders, and Grains*. Springer New York, New York, NY, 2000. (page: 21)

[34] L. Eça and M. Hoekstra. Evaluation of numerical error estimation based on grid refinement studies with the method of the manufactured solutions. *Computers & Fluids*, 38(8):1580–1591, 2009. (page: 44)

[35] L. Eça and M. Hoekstra. A procedure for the estimation of the numerical uncertainty of CFD calculations based on grid refinement studies. *Journal of Computational Physics*, 262:104–130, 2014. (page: 44)

[36] S. Ergun. Fluid flow through packed columns. *Chemical Engineering Progress*, 48(2):89–94, 1952. (page: 63, 64, 88)

[37] T. K. Fannelöp. *Fluid Mechanics for Industrial Safety and Environmental Protection.* Industrial Safety Series. Elsevier Science, Burlington, 2013. (page: 99)

[38] M. Fei, Q. Sun, D. Zhong, and G.D. Zhou. Simulations of granular flow along an inclined plane using the Savage–Hutter model. *Particuology*, 10(2):236–241, 2012. (page: 16)

[39] M. Fischer, O. Herbst, and H. Schmidt. Demonstration of the heat removing capabilities of the EPR core catcher. *Nuclear Engineering and Design*, 235(10-12):1189–1200, 2005. (page: 9)

[40] J. D. Gabor. Simulation experiments for internal heat generation. *Reactor Development Program Progress, Report*, ANL-RDP-32:7–50, 1974. (page: 77, 93)

[41] R. D. Gasser, R. O. Gauntt, and S. C. Bourcier. Late-phase melt progression experiment: MP-2 results and analysis. Technical Report NUREG/CR–6167, United States, 1997. (page: 12)

[42] R. O. Gauntt, R. K. Cole, C. M. Erickson, R. G. Gido, R. D. Gasser, S. B. Rodriguez, and M. F. Young. MELCOR computer code manuals. *Sandia National Laboratories, NUREG/CR*, 6119, 2005. (page: 13)

[43] P. Glaister. Approximate Riemann solutions of the shallow water equations. *Journal of Hydraulic Research*, 26(3):293–306, 1988. (page: 29)

[44] D. M. Hanes and D. L. Inman. Experimental evaluation of a dynamic yield criterion for granular fluid flows. *Journal of Geophysical Research*, 90(B5):3670, 1985. (page: 23)

[45] A Harten. High-resolution schemes for hyperbolic conservation laws. *Journal of Computational Physics*, 49:357–385, 1983. (page: 119)

[46] A. Harten and J. M. Hyman. Self adjusting grid methods for one-dimensional hyperbolic conservation laws. *Journal of Computational Physics*, 50(2):235–269, 1983. (page: 31)

[47] A. Hartmann, M. Buck, and J. Starflinger. Three-dimensional analysis on the coolability of inhomogeneous debris bed with the code MEWA 3D. In *Proceedings of the 2016 International Congress on Advances in Nuclear Power Plants (ICAPP 2016)*, April 17-20 2016. (page: v, vi, 13, 98, 99)

[48] K. Hu and T. G. Theofanous. On the measurement and mechanism of dryout in volumetrically heated coarse particle beds. *International Journal of Multiphase Flow*, 17(4):519–532, 1991. (page: 88)

[49] Z. Huang and W. Ma. Validation and application of the MEWA code to analysis of debris bed coolability. *Nuclear Engineering and Design*, 327:22–37, 2018. (page: 13)

[50] I. Huhtiniemi, D. Magallon, and H. Hohmann. Results of recent KROTOS FCI tests: Alumina versus corium melts. *Nuclear Engineering and Design*, 189(1-3):379–389, 1999. (page: 11)

[51] K. Hutter and T. Koch. Motion of a granular avalanche in an exponentially curved chute: Experiments and theoretical predictions. *Philosophical Transactions of the Royal Society A: Mathematical, Physical and Engineering Sciences*, 334(1633):93–138, 1991. (page: 22, 96)

[52] K. Hutter and K. R. Rajagopal. On flows of granular materials. *Continuum Mechanics and Thermodynamics*, 6(2):81–139, 1994. (page: 21)

[53] IAEA. *Nuclear Power Reactors in the World*, volume v. 2 of *Reference Data Series No. 2*. IAEA, Vienna, 2017th ed. edition, 2017. (page: 5)

[54] H. M. Jaeger, S. R. Nagel, and R. P. Behringer. Granular solids, liquids, and gases. *Reviews of Modern Physics*, 68(4):1259–1273, 1996. (page: 19, 21)

[55] G. S. Jiang, D. Levy, C. T. Lin, S. Osher, and E. Tadmor. High-resolution nonoscillatory central schemes with nonstaggered grids for hyperbolic conservation laws. *SIAM Journal on Numerical Analysis*, 35(6):2147–2168, 1998. (page: 40)

[56] Hong Jiang, editor. *Proceedings of The 20th Pacific Basin Nuclear Conference*. Springer Singapore, Singapore, 2017. (page: 5)

[57] P. C. Johnson and R. Jackson. Frictional–collisional constitutive relations for granular materials, with application to plane shearing. *Journal of Fluid Mechanics*, 176(-1):67, 1987. (page: 23)

[58] A. Karbojian, W. M. Ma, P. Kudinov, and T.-N. Dinh. A scoping study of debris bed formation in the DEFOR test facility. *Nuclear Engineering and Design*, 239(9):1653–1659, 2009. (page: 14, 96)

[59] M. G. Kendall. A new measure of rank correlation. *Biometrika*, 30(1/2):81, 1938. (page: 56)

[60] D. V. Khakhar, A. V. Orpe, P. Andreén, and J. M. Ottino. Surface flow of granular materials: Model and experiments in heap formation. *Journal of Fluid Mechanics*, 441, 2001. (page: 16, 21)

[61] E. Kim, W. H. Jung, J. H. Park, H. S. Park, and K. Moriyama. Experiments on sedimentation of particles in a water pool with gas inflow. *Nuclear Engineering and Technology*, 48(2):457–469, 2016. (page: 15)

[62] M. G. Kleinhans, H. Markies, S. J. De Vet, A. C. in 't Veld, and F. N. Postema. Static and dynamic angles of repose in loose granular materials under reduced gravity. *Journal of Geophysical Research*, 116(E11), 2011. (page: 21)

[63] T. S. Komatsu, S. Inagaki, N. Nakagawa, and S. Nasuno. Creep motion in a granular pile exhibiting steady surface flow. *Physical review letters*, 86(9):1757–1760, 2001. (page: 21)

[64] P. Kudinov, M. Davydov, G. Pohlner, M. Bürger, M. Buck, and R. Meignen. Validation of the fci codes against defor-a data on the mass fraction of agglomerated debris. In *Proceedings of the 5th European Review Meeting on Severe Accident Research (ERMSAR-2012)*, pages 21–23, March 21–23 2012. (page: 14)

[65] P. Kudinov and T.-N. Dinh. A computational study of debris bed formation. *Transaction of American Nuclear Society 2008*, 98:341, 2008. (page: 14)

[66] P. Kudinov, A. Karbojian, W. Ma, and T.-N. Dinh. The DEFOR-S experimental study of debris formation with corium simulant materials. *Nuclear Technology*, 170(1):219–230, 2017. (page: 14, 52, 96)

[67] P. Kudinov, A. Konovalenko, D. Grishchenko, S. Yakush, S. Basso, N. Lubchenko, and A. Karbojian. Investigation of debris bed formation, spreading and coolability. Technical Report NKS–287, KTH Royal Institute of Technology, Sweden, 2013. (page: 14, 52)

[68] P. D. Lax. Weak solutions of nonlinear hyperbolic equations and their numerical computation. *Communications on Pure and Applied Mathematics*, 7(1):159–193, 1954. (page: 33)

[69] S. Leininger. *Experimentelle Untersuchungen der Kühlbarkeit prototypischer Schüttungskonfigurationen unter dem Aspekt der Reaktorsicherheit.* PhD thesis, Universität Stuttgart, 2017. (page: 12, 63)

[70] R. J. LeVeque. *Finite volume methods for hyperbolic problems.* Cambridge texts in applied mathematics. Cambridge University Press, Cambridge and New York, 2002. (page: 29)

[71] R. J. LeVeque. *Finite Volume Methods for Hyperbolic Problems.* Cambridge University Press, Cambridge, 2002. (page: 32)

[72] D. Levy, G. Puppo, and G. Russo. Central WENO schemes for hyperbolic systems of conservation laws. *ESAIM: Mathematical Modelling and Numerical Analysis*, 33(3):547–571, 1999. (page: 33)

[73] L. Li, W. Ma, and S. Thakre. An experimental study on pressure drop and dryout heat flux of two-phase flow in packed beds of multi-sized and irregular particles. *Nuclear Engineering and Design*, 242:369–378, 2012. (page: 63)

[74] R. J. Lipinski. Model for boiling and dryout in particle beds. Technical Report NUREG/CR–2646, Sandia National Labs., 1982. (page: 88)

[75] C. K. K. Lun, S. B. Savage, D. J. Jeffrey, and N. Chepurniy. Kinetic theories for granular flow: Inelastic particles in couette flow and slightly inelastic particles in a general flowfield. *Journal of Fluid Mechanics*, 140(-1):223, 1984. (page: 20)

[76] D. Magallon. Characteristics of corium debris bed generated in large-scale fuel-coolant interaction experiments. *Nuclear Engineering and Design*, 236(19-21):1998–2009, 2006. (page: 52)

[77] D. Magallon. Formation and characterisation of corium debris arising from fuel–coolant interaction. *Nuclear Engineering and Design*, 236:1998–2009, 2006. (page: 8, 11, 52)

[78] D. Magallon and H. Hohmann. High pressure corium melt quenching tests in FARO. *Nuclear Engineering and Design*, 155(1-2):253–270, 1995. (page: 8, 52)

[79] D. Magallon and I. Huhtiniemi. Corium melt quenching tests at low pressure and subcooled water in FARO. *Nuclear Engineering and Design*, 204(1-3):369–376, 2001. (page: 11)

[80] D. Magallon, I. Huhtiniemi, and H. Hohmann. Lessons learnt from FARO/TERMOS corium melt quenching experiments. *Nuclear Engineering and Design*, 189(1-3):223–238, 1999. (page: 11, 96)

[81] J. E. Marsden, L. Sirovich, F. John, E. Godlewski, and P.-A. Raviart. *Numerical Approximation of Hyperbolic Systems of Conservation Laws*, volume 118. Springer New York, New York, NY, 1996. (page: 29)

[82] M. Y. Matsuo, D. Nishiura, and H. Sakaguchi. Geometric effect of angle of repose revisited. *Granular Matter*, 16(4):441–447, 2014. (page: 21)

[83] R. K. McCardell, M. L. Russell, D. W. Akers, and C. S. Olsen. Summary of TMI-2 core sample examinations. *Nuclear Engineering and Design*, 118(3):441–449, 1990. (page: 7)

[84] N. Mitarai and H. Nakanishi. Granular flow: Dry and wet. *The European Physical Journal Special Topics*, 204(1):5–17, 2012. (page: 21)

[85] K. Miyazaki, K. Murai, T. Ohama, N. Yamaoka, and S. Inoue. Dryout heat flux for core debris bed, (I): Effects of system pressure and particle size. *Journal of nuclear science and technology*, 23(8):702–710, 1986. (page: 10)

[86] U. Müller and C. Günther. *Post accident debris cooling: Proceedings of the Fifth Post Accident Heat Removal Information Exchange Meeting, July 28-30, 1982, Nuclear Research Center Karlsruhe, Karlsruhe.* Wissenschaft + Technik. G. Braun, Karlsruhe, 1983. (page: 77, 93)

[87] C. L. Nalezny. Summary of the nuclear regulatory commission's LOFT program research findings. Technical Report NUREG/CR–3005, United States, 1985. (page: 12)

[88] H. Nessyahu and E. Tadmor. Non-oscillatory central differencing for hyperbolic conservation laws. *Journal of Computational Physics*, 87(2):408–463, 1990. (page: 33)

[89] S. Ogawa, A. Umemura, and N. Oshima. On the equations of fully fluidized granular materials. *Zeitschrift für angewandte Mathematik und Physik ZAMP*, 31(4):483–493, 1980. (page: 20)

[90] A. V. Orpe and D. V. Khakhar. Scaling relations for granular flow in quasi-two-dimensional rotating cylinders. *Physical review. E, Statistical, nonlinear, and soft matter physics*, 64(3 Pt 1):031302, 2001. (page: 16, 23)

[91] K. Pearson. Note on regression and inheritance in the case of two parents. *Proceedings of the Royal Society of London (1854-1905)*, 58(-1):240–242, 1895. (page: 55)

[92] G. Pohlner, Z. Vujic, M. Bürger, and G. Lohnert. Simulation of melt jet breakup and debris bed formation in water pools with IKEJET/IKEMIX. *Nuclear Engineering and Design*, 236(19-21):2026–2048, 2006. (page: 13)

[93] S. P. Pudasaini and K. Hutter. *Avalanche dynamics: Dynamics of rapid flows of dense granular avalanches ; with 15 tables.* Springer, Berlin, 2007. (page: 21)

[94] S. P. Pudasaini, K. Hutter, S.-S. Hsiau, S.-C. Tai, Y. Wang, and R. Katzenbach. Rapid flow of dry granular materials down inclined chutes impinging on rigid walls. *Physics of Fluids*, 19(5):053302, 2007. (page: 21)

[95] S. Rahman. *Coolability of corium debris under severe accident conditions in light water reactors.* PhD thesis, Universität Stuttgart. (page: 8, 11, 13, 89)

[96] A. W. Reed. *The effect of channeling on the dryout of heated particulate beds immersed in a liquid pool.* PhD thesis, Massachusetts Institute of Technology, 1982. (page: 88)

[97] A. W. Reed, K. R. Boldt, E. D. Gorham-Bergeron, R. J. Lipinski, and T. R. Schmidt. DCC-1/DCC-2 degraded core coolability analysis. Technical Report NUREG/CR-4390-R3, Sandia National Labs., Albuquerque, NM (USA), 1985. (page: iv, 10, 11)

[98] N. Reinke, T. Drath, T. v. Berlepsch, H. E. Unger, and M. K. Koch. Formation, characterisation and cooling of debris. *Nuclear Engineering and Design*, 236(19-21):1955–1964, 2006. (page: 8)

[99] O. Reynolds. LVII. On the dilatancy of media composed of rigid particles in contact. with experimental illustrations. *The London, Edinburgh, and Dublin Philosophical Magazine and Journal of Science*, 20(127):469–481, 1885. (page: 20)

[100] L. F. Richardson. The approximate arithmetical solution by finite differences of physical problems involving differential equations, with an application to the stresses in a masonry dam. *Philosophical Transactions of the Royal Society A: Mathematical, Physical and Engineering Sciences*, 210(459-470):307–357, 1911. (page: 44)

[101] L. F. Richardson and J. A. Gaunt. The deferred approach to the limit. Part I. Single lattice. Part II. Interpenetrating lattices. *Philosophical Transactions of the Royal Society A: Mathematical, Physical and Engineering Sciences*, 226(636-646):299–361, 1927. (page: 44)

[102] P. J. Roache. Perspective: A method for uniform reporting of grid refinement studies. *Journal of Fluids Engineering*, 116(3):405, 1994. (page: 44, 48)

[103] P. J. Roache. Quantification of uncertainty in computational fluid dynamics. *Annual review of fluid mechanics*, 29(1):123–160, 1997. (page: 44)

[104] P. J. Roache. *Verification and validation in computational science and engineering.* Hermosa publishers, Albuquerque, N.M., op. 1998. (page: 44, 46, 52)

[105] D. A. Robinson and S. P. Friedman. Observations of the effects of particle shape and particle size distribution on avalanching of granular media. *Physica A: Statistical Mechanics and its Applications*, 311(1-2):97–110, 2002. (page: 52)

[106] P. L. Roe. Approximate Riemann solvers, parameter vectors, and difference schemes. *Journal of Computational Physics*, 43(2):357–372, 1981. (page: 27, 29)

[107] C. Roy. Review of discretization error estimators in scientific computing. *48th AIAA Aerospace Sciences Meeting Including the New Horizons Forum and Aerospace Exposition*, 01 2010. (page: 44, 48)

[108] S. B. Savage. Gravity flow of cohesionless granular materials in chutes and channels. *Journal of Fluid Mechanics*, 92(01):53, 1979. (page: 21)

[109] S. B. Savage. Granular flows at high shear rates. In Richard E. Meyer, editor, *Theory of Dispersed Multiphase Flow*, pages 339–358. Elsevier, 1983. (page: 20)

[110] S. B. Savage and K. Hutter. The motion of a finite mass of granular material down a rough incline. *Journal of Fluid Mechanics*, 199(-1):177, 1989. (page: 33)

[111] S. B. Savage and D. J. Jeffrey. The stress tensor in a granular flow at high shear rates. *Journal of Fluid Mechanics*, 110(-1):255, 1981. (page: 20)

[112] S. B. Savage, R. M. Nedderman, U. Tüzün, and G. T. Houlsby. The flow of granular materials-III rapid shear flows. *Chemical Engineering Science*, 38(2):189–195, 1983. (page: 23)

[113] G. Schanz, S. Hagen, P. Hofmann, G. Schumacher, and L. Sepold. Information on the evolution of severe LWR fuel element damage obtained in the CORA program. *Journal of Nuclear Materials*, 188:131–145, 1992. (page: 12)

[114] W. Schmidt. *Influence of multidimensionality and interfacial friction on the coolability of fragmented corium.* PhD thesis, Universität Stuttgart. (page: 8, 10, 13, 89)

[115] T. Schulenberg and U. Mueller. A refined model for the coolability of core debris with flow entry from the bottom. Technical Report KFK–3880/2, Germany, 1984. (page: 88)

[116] M. Schwarz, G. Hache, and P. von der Hardt. Phebus fp: A severe accident research programme for current and advanced light water reactors. *Nuclear Engineering and Design*, 187(1):47–69, 1999. (page: 12)

[117] B. R. Sehgal. Stabilization and termination of severe accidents in LWRs. *Nuclear Engineering and Design*, 236(19-21):1941–1952, 2006. (page: 9)

[118] J.-M Seiler, A. Latrobe, B. R. Sehgal, H. Alsmeyer, O. Kymäläinen, B. Turland, J.-L. Grange, M. Fischer, G. Azarian, M. Bürger, C. J. Cirauqui, and A. Zurita. Analysis of corium recovery concepts by the EUROCORE group. *Nuclear Engineering and Design*, 221(1-3):119–136, 2003. (page: 9)

[119] M. Shamsuzzaman, T. Horie, F. Fuke, M. Kamiyama, T. Morioka, T. Matsumoto, K. Morita, H. Tagami, T. Suzuki, and Y. Tobita. Experimental study on debris bed characteristics for the sedimentation behavior of solid particles used as simulant debris. *Annals of Nuclear Energy*, 111:474–486, 2018. (page: 82)

[120] M. A. R. Sheikh, E. Son, M. Kamiyama, T. Morioka, T. Matsumoto, K. Morita, K. Matsuba, K. Kamiyama, and T. Suzuki. Experimental investigation on characteristics of mixed particle debris in sedimentation and bed formation behavior. In *Proceedings of the 11th International Topical Meeting on Nuclear Thermal-Hydraulics, Operation and Safety (NUTHOS-11)*, October 9-13 2016. (page: 82)

[121] B. L. Smith. On the modelling of bubble plumes in a liquid pool. *Applied Mathematical Modelling*, 22(10):773–797, 1998. (page: 99)

[122] J. H. Song, S. W. Hog, J. H. Kim, Y. J. Chang, Y. S. Shin, B. T. Min, and H. D. Kim. Insights from the recent steam explosion experiments in TROI. *Journal of Nuclear Science and Technology*, 40(10):783–795, 2003. (page: 11)

[123] C. Spearman. 'footrule' for measuring correlation. *British Journal of Psychology, 1904-1920*, 2(1):89–108, 1906. (page: 55)

[124] B. W. Spencer, K. Wang, C. A. Blomquist, L. M. McUmber, and J. P. Schneider. *Fragmentation and quench behavior of corium melt streams in water*. 1994. (page: 11, 96)

[125] D. Squarer, A. T. Pieczynski, and L. E. Hochreiter. Effect of debris bed pressure, particle size, and distribution on degraded nuclear reactor core coolability. *Nuclear Science and Engineering*, 80(1):2–13, 1982. (page: 10)

[126] A. Stuart. Rank correlation methods. by M. G. Kendall, 2nd edition. *British Journal of Statistical Psychology*, 9(1):68, 1956. (page: 56)

[127] Y. C. Tai, S. Noelle, J.M.N.T. Gray, and K. Hutter. Shock-capturing and front-tracking methods for granular avalanches. *Journal of Computational Physics*, 175(1):269–301, 2002. (page: 33, 34)

[128] E. Takasuo. An experimental study of the coolability of debris beds with geometry variations. *Annals of Nuclear Energy*, 92:251–261, 2016. (page: 77)

[129] E. Takasuo, S. Holmström, T. Kinnunen, and P. H. Pankakoski. The COOLOCE experiments investigating the dryout power in debris beds of heap-like and cylindrical geometries. *Nuclear Engineering and Design*, 250:687–700, 2012. (page: 77)

[130] K. Trambauer, C. Bals, J. D. Schubert, and H. Austregesilo. ATHLET-CD Mod 1.1 - Cycle K User's Manual. *Gesellschaft für Anlagen-und Reaktorsicherheit (GRS), GRS-P-2*, 1, 2003. (page: 13)

[131] R. Trenberth and G. F. Stevens. An experimental study of boiling heat transfer and dryout in heated particulate beds. Technical Report AEEW-R–1342, United Kingdom, 1980. (page: 10)

[132] V. X. Tung and V. K. Dhir. A hydrodynamic model for two-phase flow through porous media. *International Journal of Multiphase Flow*, 14(1):47–65, 1988. (page: 88)

[133] J. P. van Dorsselaere, S. Pignet, C. Seropian, T. Montanelli, P. Giordano, F. Jacq, and B. Schwinges, editors. *Development and assessment of ASTEC code for severe accident simulation*, 2005. (page: 13)

[134] B. van Leer. Towards the ultimate conservative difference scheme. V. A second-order sequel to Godunov's method. *Journal of Computational Physics*, 32(1):101–136, 1979. (page: 36)

[135] M. E. Vázquez-Cendón. Improved treatment of source terms in upwind schemes for the shallow water equations in channels with irregular geometry. *Journal of Computational Physics*, 148(2):497–526, 1999. (page: 29)

[136] Y. Wang and K. Hutter. A constitutive model of multiphase mixtures and its application in shearing flows of saturated solid-fluid mixtures. *Granular Matter*, 1(4):163–181, 1999. (page: 22, 96)

[137] Y. Wang and K. Hutter. Shearing flows in a goodman-cowin type granular material — theory and numerical results. *Particulate Science and Technology*, 17(1-2):97–124, 1999. (page: 22, 96)

[138] Y. Wang, K. Hutter, and S. P. Pudasaini. The Savage-Hutter theory: A system of partial differential equations for avalanche flows of snow, debris, and mud. *ZAMM*, 84(8):507–527, 2004. (page: 27, 33)

[139] W. Widmann, M. Bürger, G. Lohnert, H. Alsmeyer, and W. Tromm. Experimental and theoretical investigations on the COMET concept for ex-vessel core melt retention. *Nuclear Engineering and Design*, 236(19-21):2304–2327, 2006. (page: 9)

[140] J. R. Wolf, J. L. Rempe, L. A. Stickler, G. E. Korth, D. R. Diercks, L. A. Neimark, D. W. Akers, B. K. Schuetz, T. L. Shearer, S. A. Chavez, G. L. Thinnes, R. J. Witt, M. L. Corradini, and J. A. Kos. TMI-2 vessel investigation project integration report. Technical report, United States, 1994. NUREG/CR–6197. (page: 8)

[141] S. Yakush and P. Kudinov. Transient phenomena of ex-vessel debris bed formation in a LWR severe accident. *American Nuclear Society Transactions*, pages 546–547, 2009. (page: 14)

[142] S. Yakush, P. Kudinov, and T.-N. Dinh. Multiscale simulations of self-organization phenomena in the formation and coolability of corium debris bed. In *Proceedings The 13th International Topical Meeting on Nuclear Reactor Thermal Hydraulics (NURETH-13), Paper N13P1143*, September 27 - October 2 2009. (page: 14)

[143] B. Zhang, T. Harada, D. Hirahara, T. Matsumoto, K. Morita, K. Fukuda, H. Yamano, T. Suzuki, and Y. Tobita. Self-leveling onset criteria in debris beds. *Journal of Nuclear Science and Technology*, 47(4):384–395, 2010. (page: 77)

[144] B. Zhang, T. Harada, D. Hirahara, T. Matsumoto, K. Morita, K. Fukuda, H. Yamano, T. Suzuki, and Y. Tobita. Experimental investigation on self-leveling behavior in debris beds. *Nuclear Engineering and Design*, 241(1):366–377, 2011. (page: 78)

[145] V. Zhdanov. COTELS project (2): Fuel coolant interaction tests under ex-vessel conditions. In *Proceedings of the OECD Workshop on Ex-Vessel Debris Coolability*, November 15-18 1999. (page: 11)

Appendices

Appendix A
Total Variation Diminishing (TVD) methods

In order to construct oscillation-free schemes, the condition of *monotonicity preserving* is necessary.

Definition (monotonicity preserving)**.** *A numerical method is monotonicity preserving if the solution* q^n *is monotonically increasing (or decreasing) in space, then so is* q^{n+1}*, i.e.*

$$if \qquad \forall j : q_{j+1}^n \geq q_j^n \Rightarrow q_{j+1}^{n+1} \geq q_j^{n+1}, \forall j. \tag{A.1}$$

Harten (1983) [45] proved that:

- **(i)**: a monotone scheme is TVD, and
- **(ii)**: a TVD scheme is monotonicity preserving.

Hence, if higher-order TVD schemes can be constructed, these schemes will be monotonicity preserving.

Let's first start with the definition of the Total variation (TV) of a physical solution $q = q\left(x, t\right)$ which is given by

$$TV = \int \left| \frac{\partial q}{\partial x} \right| dx \tag{A.2}$$

and the total variation for the discrete case is:

$$TV(q^n) = \sum_j \left| q_{j+1}^n - q_j^n \right| \tag{A.3}$$

A numerical scheme is said to be total variation diminishing (TVD), if

$$TV\left(q^{n+1}\right) \leq TV\left(q^n\right) \tag{A.4}$$

The central idea in constructing a TVD method is to attempt to develop a higher-order scheme that will avoid oscillations and exhibit properties similar to those of monotone schemes. For such methods, the solution is first-order near discontinuities and higher order in smooth regions. The transition to the higher order is accomplished by the use of slope limiters on the dependent variables or flux limiters.

Appendix B
Flowchart of the Debris Bed Formation Model

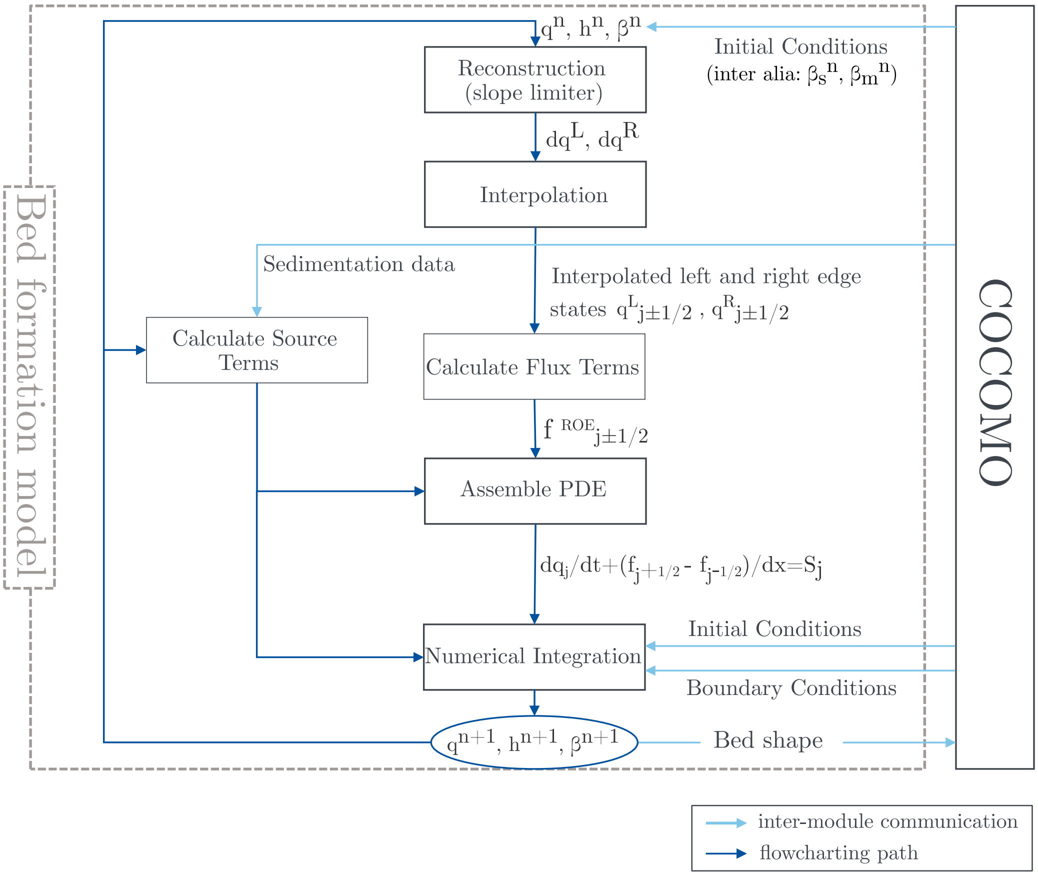

Figure 7.2: Flowchart of the debris bed formation model

Acknowledgements

Foremost, I would like to express my deepest gratitude to my advisor Professor Jörg Starflinger for the continuous support of my Ph.D. study and related research. The door to his office was always open whenever I ran into a trouble spot or had a question about my research or writing. My sincere thanks are extended to Professor Thomas Schulenberg, my co-advisor, for his interest in my work, and comments.

I would also like to thank most sincerely Michael Buck for his continuous assistance and valuable support during my Ph.D. study and research at the IKE. He has inspired me to become an independent researcher and helped me realize the power of critical reasoning. His guidance and efforts enabled me to improve my research methodology and understanding of different numerical challenges. I am also very grateful for the friendly help of Professor Eckart Laurien during the numerical studies and Dr. Rudi Kulenovic for his patience and support during the experimental investigations and the setup of the test facility. Thanks also are due to the GRS for its support and the German Federal Ministry for Economic Affairs and Energy for the funding of my work. I am also very grateful to all the administrative and research staff at the IKE.

I would like to express my special gratitude to my beloved wife, my eternal cheerleader and companion, for the unfailing emotional support, she had provided me during this work.

Finally, last but by no means least, this dissertation is dedicated to my parents, my little brother, and sister for their endless love, support, and encouragement despite the long distance between us.
Thanks God, the merciful, for providing me the strength to step in the beautiful world of science.
Thanks for all your encouragement!

Stuttgart, in February 2019

Wael Hilali.